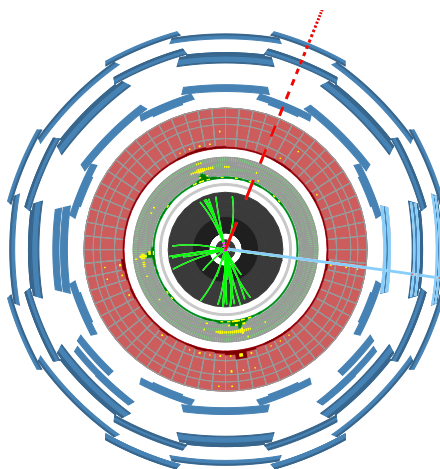


Nuno Filipe da Silva Fernandes de Castro

Study of the Wtb vertex structure at the ATLAS experiment



*Dissertação de Doutoramento em Física,
Especialidade de Física Experimental,
apresentada à Faculdade de Ciências e Tecnologia da
Universidade de Coimbra*

CERN-THESIS-2008-083
17/10/2008



UNIVERSIDADE DE COIMBRA
2008

Dissertação de Doutoramento em Física, Especialidade de Física Experimental
Faculdade de Ciências e Tecnologia da Universidade de Coimbra

Orientador: Professor Doutor João Carlos Lopes de Carvalho
Co-orientador: Professor Doutor António Joaquim Onofre de Abreu Ribeiro Gonçalves

Coimbra, 2008

Resumo

O quark *top* é o mais pesado e o menos estudado dos quarks do Modelo Padrão da Física de Partículas. Apesar de as suas propriedades terem já sido estudadas em colisionadores, a estatística dos dados colectados até ao momento não permitiu que fossem efectuadas medidas precisas, com excepção da medida da sua massa. A determinação de outras propriedades fundamentais, tais como os seus acoplamentos, requer grandes amostras de dados, que serão obtidas no *Large Hadron Collider* (LHC) do CERN.

No Modelo Padrão, o vértice Wtb é puramente esquerdo, sendo a sua amplitude determinada pelo elemento V_{tb} da matriz de Cabibbo-Kobayashi-Maskawa, que se relaciona com a corrente carregada associada à interacção fraca entre um quark *top* e um quark *b*. De uma forma mais geral, podem ser introduzidos acoplamentos adicionais, tais como acoplamentos vectoriais direitos e acoplamentos tensoriais esquerdos e direitos. O estudo das distribuições angulares dos produtos do decaimento do quark *top* permitirá a medida precisa da estrutura do vértice Wtb , proporcionando igualmente um importante teste de possíveis extensões do Modelo Padrão.

Na presente tese é discutida a sensibilidade de ATLAS para o estudo dos acoplamentos anómalos associados ao vértice Wtb . Para tal, considera-se a produção de pares $t\bar{t}$ em LHC e estudam-se diferentes observáveis, tais como assimetrias angulares, bem como fracções e razões de helicidade do bóson W . Os resultados espectáveis para luminosidades de 10 fb^{-1} e 1 fb^{-1} são obtidos através da combinação dos observáveis mais sensíveis.

Abstract

The top quark is the heaviest and least studied quark of the Standard Model. Although its properties have already been investigated at colliders, the statistics of the collected data have not yet allowed for precise measurements, with exception of its mass. The determination of other fundamental properties such as its couplings requires larger top quark samples, which will be available at the Large Hadron Collider (LHC) at CERN.

Within the Standard Model, the Wtb vertex is purely left-handed, and its amplitude is given by the Cabibbo-Kobayashi-Maskawa matrix element V_{tb} , related to weak interaction between a top and a b -quark. In a more general way, additional anomalous couplings such as right-handed vectorial couplings and left and right-handed tensorial couplings can also be considered. The study of the angular distribution of the top quark decay products at the LHC will allow precision measurements of the structure of the Wtb vertex, providing also an important probe for possible physics beyond the SM.

In the present thesis, the ATLAS sensitivity to anomalous Wtb couplings is studied. For this, the $t\bar{t}$ pair production at the LHC is considered and different observables, such as angular asymmetries and W helicity fractions and ratios, are discussed. The expected results for luminosities of 10 fb^{-1} and 1 fb^{-1} are obtained through the combination of the most sensitive observables.

Acknowledgments

First and foremost, I want to thank Professors António Onofre and João Carvalho, who supervised this thesis, for their continuous support, guidance and friendship.

I also thank Laboratório de Instrumentação e Física Experimental de Partículas for providing me with all the institutional support needed for my work, with an acknowledgement, in particular, to Professor Amélia Maio, Team Leader of the Portuguese ATLAS group and to the Heads of the projects “Physics at LHC” and “ATLAS GRID”.

Part of the computational work of this thesis has been performed in the HPC Milipeia center at the Laboratório de Computação Avançada of the University of Coimbra. A special word is due to Miguel Oliveira, for his patience and help.

I also acknowledge the support given by the Fundação para a Ciência e a Tecnologia, through the grant SFRH/BD/13936/2003.

I owe a debt of gratitude to my colleagues from Coimbra and Lisboa, especially to the members of the Portuguese ATLAS group, the former members of the Portuguese DELPHI group (with whom I started to work in Particle Physics) and my office colleagues (in particular Matilde Castanheira for her kindness and friendship). They were always available and ready for an exchange of ideas, contributing to an amazing work environment. A special thank you to Sofia Andringa for the careful reading of the thesis and for the very useful comments and suggestions.

I thank the ATLAS Collaboration, in particular the Top Working Group and the Top Properties Subgroup members, for the discussions on the analyses and Collaboration tools.

Professor Juan António Aguilar Saavedra gave a very important contribution to the theoretical part of this work and I thank him for the collaboration. To him and also to the Professors Orlando Oliveira, Pedro Ferreira and Rui Santos I thank the many fruitful discussions. From my personal point of view, the collaboration between theoreticians and experimentalists has always been rewarding.

I thank all the members of the Departamento de Física Teórica y del Cosmos of the University of Granada, where I spent a month working, in May 2007. A special word is due to Professor Francisco del Aguila Giménez, for the support and advice.

I would also like to thank Filipe Veloso, my working colleague, for his help, time and suggestions, as well as for his friendship. We have walked a long path together. To my other friends, especially Filipe, Leonor, Nils, Renato and Rui, thank you for being there for me.

Finally, I have to thank my family for their love and emotional support, especially to my children, Pedro and Laura, whom I apologise for not being able to play with them as many times as I wished. Although they do not know it yet, they were of great importance to this work. Again, a very special word to Mariana, for the love, sharing and friendship. Without her continuous support it would have been almost impossible to conciliate my family and my work.

*à Mariana,
ao Pedro,
à Laura*

“Primum vivere depois escribir.”

Luiz Pacheco – *Diário Remendado*

Contents

| | | |
|----------|--|-----------|
| 1 | Introduction | 1 |
| 2 | The top quark and the Wtb vertex | 3 |
| 2.1 | The Standard Model | 3 |
| 2.2 | The top quark | 7 |
| 2.2.1 | Top quark production at the LHC | 8 |
| 2.3 | The Wtb vertex | 8 |
| 2.3.1 | W -boson helicity fractions and ratios | 11 |
| 2.3.2 | Angular asymmetries | 18 |
| 3 | The ATLAS experiment at the LHC | 21 |
| 3.1 | The LHC collider | 21 |
| 3.2 | The ATLAS detector | 23 |
| 3.2.1 | ATLAS coordinate system | 24 |
| 3.2.2 | Magnet system | 27 |
| 3.2.3 | Inner detector | 27 |
| 3.2.4 | Calorimeter system | 29 |
| 3.2.5 | Muon system | 32 |
| 3.2.6 | Forward detectors | 33 |
| 3.2.7 | Trigger and data acquisition systems | 33 |
| 3.2.8 | LHC computing Grid | 36 |
| 3.2.9 | Detector Control System | 36 |
| 4 | Monte Carlo generation, simulation and reconstruction | 37 |
| 4.1 | Signal and background processes | 37 |
| 4.1.1 | Parton Distribution Functions | 38 |
| 4.1.2 | Hadronization | 41 |
| 4.2 | Fast simulation | 41 |
| 4.2.1 | Monte Carlo generation | 42 |
| 4.2.2 | Event simulation and reconstruction | 43 |
| 4.3 | Full simulation | 45 |
| 4.3.1 | Monte Carlo generation | 47 |
| 4.3.2 | Detector simulation, digitization and reconstruction | 51 |
| | Event reconstruction | 51 |
| | Expected trigger performance | 53 |

| | | |
|----------|---|------------|
| 5 | Event analysis | 57 |
| 5.1 | Analysis for $L=10 \text{ fb}^{-1}$ | 57 |
| 5.1.1 | Preselection | 58 |
| 5.1.2 | Final selection | 61 |
| 5.1.3 | W polarization and angular asymmetries | 67 |
| 5.1.4 | Systematic uncertainties | 69 |
| 5.2 | Analyses for $L=1 \text{ fb}^{-1}$ | 72 |
| 5.2.1 | Analysis without b -tagging | 72 |
| 5.2.2 | Analysis with b -tagging | 83 |
| 5.2.3 | W polarization and angular asymmetries | 89 |
| 5.2.4 | Systematic uncertainties | 91 |
| 6 | Expected constraints on the Wtb anomalous couplings | 95 |
| 6.1 | Expected limits at ATLAS | 95 |
| 6.2 | Possible improvements on the limits | 104 |
| 7 | Conclusions | 107 |
| A | Effect of m_b in the helicity fractions | 111 |
| B | Fits used in the systematic error evaluation | 113 |
| | Bibliography | 127 |

List of Figures

| | | |
|------|---|----|
| 2.1 | <i>Summary and combination of the Tevatron top mass measurements</i> | 7 |
| 2.2 | <i>Leading order Feynman diagrams corresponding to the $t\bar{t}$ production at the LHC</i> | 9 |
| 2.3 | <i>Examples of leading order Feynman diagrams corresponding to the single top production at the LHC</i> | 9 |
| 2.4 | <i>Representation of the top quark decay into a b-quark and a W-boson with positive (right-handed), negative (left-handed) or zero helicity</i> | 11 |
| 2.5 | <i>Differential distribution of $\cos\theta_\ell^*$ within the SM</i> | 13 |
| 2.6 | <i>Differential distribution of $\cos\theta_\ell^*$ for different values of the Wtb anomalous couplings</i> | 13 |
| 2.7 | <i>W-boson helicity fractions measurements by the CDF and D0 collaborations</i> | 15 |
| 2.8 | <i>Dependence of the helicity fractions on the anomalous couplings (CP-conserving case)</i> | 16 |
| 2.9 | <i>Dependence of the helicity ratios on the anomalous couplings (CP-conserving case)</i> | 17 |
| 2.10 | <i>Considered angular asymmetries involving the angle θ_ℓ^*</i> | 19 |
| 2.11 | <i>Dependence of the angular asymmetries on the anomalous couplings (CP-conserving case)</i> | 20 |
| 3.1 | <i>LHC experiments</i> | 22 |
| 3.2 | <i>CERN accelerator complex</i> | 22 |
| 3.3 | <i>Atlas detector</i> | 25 |
| 3.4 | <i>ATLAS coordinate system</i> | 26 |
| 3.5 | <i>Pseudorapidity as a function of the polar angle</i> | 26 |
| 3.6 | <i>Geometry of the magnet systems</i> | 28 |
| 3.7 | <i>ATLAS Inner Detector</i> | 30 |
| 3.8 | <i>ATLAS calorimeter system</i> | 30 |
| 3.9 | <i>ATLAS muon system</i> | 34 |
| 3.10 | <i>ATLAS trigger and data acquisition systems</i> | 35 |
| 4.1 | <i>Fast and full simulation of the ATLAS detector</i> | 38 |
| 4.2 | <i>Standard Model cross-sections at the Tevatron and the LHC</i> | 39 |
| 4.3 | <i>Different final states for $t\bar{t} \rightarrow W^+ b W^- \bar{b}$ events, originated from the different W decays</i> | 40 |
| 4.4 | <i>CTEQ 6L Parton Distribution Functions for $Q^2 = (250 \text{ GeV})^2$</i> | 40 |
| 4.5 | <i>Hadronization of quarks and gluons</i> | 41 |

| | | |
|------|--|----|
| 4.6 | <i>Distributions, at the generator level (TopReX 4.10 with CTEQ 5L PDF set), of the transverse momentum, mass, η and ϕ of the hard process particles.</i> | 44 |
| 4.7 | <i>c and light jets contamination factors defined in ATLFASTB for different values of b-tagging efficiencies</i> | 45 |
| 4.8 | <i>Calibration factors applied to jets by the ATLFASTB package</i> | 46 |
| 4.9 | <i>Computing time required by the full simulation of different Monte Carlo Samples</i> | 46 |
| 4.10 | <i>Schematic representation of the full simulation production chain</i> | 47 |
| 4.11 | <i>Distributions, at the generator level (MC@NLO 3.1 with CTEQ 6M PDF set), of the transverse momentum, mass, η and ϕ of the hard process particles.</i> | 49 |
| 4.12 | <i>Distribution of the b-tagging weight variable for b, c and light jets</i> | 52 |
| 4.13 | <i>Reconstruction efficiencies for electrons, muons and quarks/gluons as function of the generated η and p_T, for the MC@NLO $t\bar{t}$ sample (full simulation)</i> | 54 |
| 4.14 | <i>Electrons and muons reconstruction efficiencies for each trigger level, as a function of p_T, η and ϕ.</i> | 55 |
| 5.1 | <i>Leptons, non b-tagged and b-tagged jet multiplicity for the signal sample (fast simulation, $L = 10 \text{ fb}^{-1}$)</i> | 58 |
| 5.2 | <i>Kinematical distributions after the preselection level (fast simulation analysis for $L = 10 \text{ fb}^{-1}$)</i> | 60 |
| 5.3 | <i>Discriminant variables construction using the signal (background) p.d.f.</i> | 62 |
| 5.4 | <i>Discriminant variable for signal and background (fast simulation, $L = 10 \text{ fb}^{-1}$). The cumulative S/\sqrt{B} and S/B distributions are also shown</i> | 62 |
| 5.5 | <i>Effect of the \mathcal{L}_R cut on the reconstructed W and t invariant masses (fast simulation, $L = 10 \text{ fb}^{-1}$)</i> | 62 |
| 5.6 | <i>ΔR separation between each of the reconstructed objects and the corresponding generated particle (fast simulation analysis for $L = 10 \text{ fb}^{-1}$)</i> | 64 |
| 5.7 | <i>Relative differences between the momenta of the reconstructed and generated objects (fast simulation analysis for $L = 10 \text{ fb}^{-1}$)</i> | 65 |
| 5.8 | <i>Relative differences between the momenta of the reconstructed and generated objects (fast simulation analysis for $L = 10 \text{ fb}^{-1}$)</i> | 66 |
| 5.9 | <i>$\cos\theta_\ell^*$ distribution in the laboratory frame (fast simulation analysis for $L = 10 \text{ fb}^{-1}$)</i> | 68 |
| 5.10 | <i>Reconstructed $\cos\theta_\ell^*$ distribution and corresponding correction function (fast simulation analysis for $L = 10 \text{ fb}^{-1}$)</i> | 68 |
| 5.11 | <i>Event display of a simulated semileptonic $t\bar{t}$ event with an electron in the final state</i> | 73 |
| 5.12 | <i>Event display of a simulated semimuonic $t\bar{t}$ event</i> | 74 |
| 5.13 | <i>Distributions, before the $\sqrt{\chi^2} < 4$ cut, of the $\sqrt{\chi^2}$ variable ($L = 1 \text{ fb}^{-1}$ analysis without b-tagging)</i> | 75 |
| 5.14 | <i>Preselection level distributions of relevant variables ($L = 1 \text{ fb}^{-1}$ analysis without b-tagging)</i> | 77 |

| | | |
|------|--|-----|
| 5.15 | <i>Preselection level distributions of the reconstructed W and t masses ($L = 1 \text{ fb}^{-1}$ analysis without b-tagging)</i> | 78 |
| 5.16 | <i>Discriminant variables for signal and background ($L = 1 \text{ fb}^{-1}$ analysis without b-tagging). The cumulative S/\sqrt{B} and S/B distributions are also shown</i> | 78 |
| 5.17 | <i>ΔR separation between each of the reconstructed objects and the corresponding generated particle (full simulation analysis without b-tagging for $L = 1 \text{ fb}^{-1}$)</i> | 80 |
| 5.18 | <i>Relative differences between the momenta of the reconstructed and generated objects (full simulation analysis without b-tagging for $L = 1 \text{ fb}^{-1}$)</i> | 81 |
| 5.19 | <i>Relative differences between the momenta of the reconstructed and generated objects ($L = 1 \text{ fb}^{-1}$ analysis without b-tagging)</i> | 82 |
| 5.20 | <i>Distributions, before the $\sqrt{\chi^2} < 4$ cut and before any trigger requirements, of the $\sqrt{\chi^2}$ variable ($L = 1 \text{ fb}^{-1}$ analysis with b-tagging)</i> | 84 |
| 5.21 | <i>Distributions, after the preselection level and normalized to $L = 1 \text{ fb}^{-1}$, of the signal and background b-tagging weights</i> | 84 |
| 5.22 | <i>Discriminant variables for signal and background ($L = 1 \text{ fb}^{-1}$ analysis with b-tagging). The cumulative S/\sqrt{B} and S/B distributions are also shown</i> | 85 |
| 5.23 | <i>ΔR separation between each of the reconstructed objects and the corresponding generated particle (full simulation analysis with b-tagging for $L = 1 \text{ fb}^{-1}$)</i> | 86 |
| 5.24 | <i>Relative differences between the momenta of the reconstructed and generated objects (full simulation analysis with b-tagging for $L = 1 \text{ fb}^{-1}$)</i> | 87 |
| 5.25 | <i>Relative differences between the momenta of the reconstructed and generated objects ($L = 1 \text{ fb}^{-1}$ analysis with b-tagging)</i> | 88 |
| 5.26 | <i>Reconstructed $\cos\theta_\ell^*$ distributions, after the final selection and normalized to $L = 1 \text{ fb}^{-1}$ (full simulation analyses with and without b-tagging)</i> | 90 |
| 5.27 | <i>Correction functions obtained for the $L = 1 \text{ fb}^{-1}$ analyses with and without b-tagging</i> | 90 |
| 5.28 | <i>Corrected $\cos\theta_\ell^*$ distributions for the $L = 1 \text{ fb}^{-1}$ analyses with and without b-tagging</i> | 90 |
| 6.1 | <i>Expected 68.3% CL confidence regions on the anomalous couplings for $L = 10 \text{ fb}^{-1}$</i> | 100 |
| 6.2 | <i>Expected 68.3% CL confidence regions on the anomalous couplings for $L = 10 \text{ fb}^{-1}$</i> | 101 |
| 6.3 | <i>Expected 68.3% CL confidence regions on the anomalous couplings for $L = 10 \text{ fb}^{-1}$ and $L = 1 \text{ fb}^{-1}$ (analyses with and without b-tagging)</i> | 102 |
| 6.4 | <i>Comparison between the limits derived from the CDF results on the W helicity fractions ($L = 1.9 \text{ fb}^{-1}$) with the ATLAS expectations for $L = 1 \text{ fb}^{-1}$</i> | 103 |
| 6.5 | <i>Expected 68.3% CL confidence regions on the anomalous couplings, obtained from the A_\pm, $\rho_{R,L}$, single top cross-section and $r_{b\ell}$ observables</i> | 105 |

| | | |
|------|---|-----|
| A.1 | <i>Dependence of the helicity fractions F_i on V_R and g_L, for the cases when the b-quark is considered and when it is neglected</i> | 112 |
| B.1 | <i>Fits used in the b-jet energy scale systematic error evaluation (fast simulation analysis, $L = 10 \text{ fb}^{-1}$)</i> | 114 |
| B.2 | <i>Fits used in the light jet energy scale systematic error evaluation (fast simulation analysis, $L = 10 \text{ fb}^{-1}$)</i> | 115 |
| B.3 | <i>Fits used in the background normalization systematic error evaluation (fast simulation analysis, $L = 10 \text{ fb}^{-1}$)</i> | 116 |
| B.4 | <i>Fits used in the top mass systematic error evaluation (fast simulation analysis, $L = 10 \text{ fb}^{-1}$)</i> | 117 |
| B.5 | <i>Fits used in the ISR/FSR systematic error evaluation (fast simulation analysis, $L = 10 \text{ fb}^{-1}$)</i> | 118 |
| B.6 | <i>Fits used in the b-tagging efficiency systematic error evaluation (fast simulation analysis, $L = 10 \text{ fb}^{-1}$)</i> | 119 |
| B.7 | <i>Fits used in the jet energy scale systematic error evaluation (full simulation analysis without b-tagging, $L = 1 \text{ fb}^{-1}$)</i> | 120 |
| B.8 | <i>Fits used in the luminosity systematic error evaluation (full simulation analysis without b-tagging, $L = 1 \text{ fb}^{-1}$)</i> | 121 |
| B.9 | <i>Fits used in the top mass systematic error evaluation (full simulation analysis without b-tagging, $L = 1 \text{ fb}^{-1}$)</i> | 122 |
| B.10 | <i>Fits used in the jet energy scale systematic error evaluation (full simulation analysis with b-tagging, $L = 1 \text{ fb}^{-1}$)</i> | 123 |
| B.11 | <i>Fits used in the luminosity systematic error evaluation (full simulation analysis with b-tagging, $L = 1 \text{ fb}^{-1}$)</i> | 124 |
| B.12 | <i>Fits used in the top mass systematic error evaluation (full simulation analysis with b-tagging, $L = 1 \text{ fb}^{-1}$)</i> | 125 |

List of Tables

| | | |
|-----|--|----|
| 2.1 | <i>Quantum numbers of the Standard Model particles</i> | 5 |
| 2.2 | <i>Experimental observables used to define the SM gauge couplings . . .</i> | 6 |
| 2.3 | <i>Quarks and charged leptons masses</i> | 6 |
| 2.4 | <i>Indirect limits on the Wtb anomalous couplings, obtained from the $BR(b \rightarrow s\gamma)$ measurement</i> | 10 |
| 3.1 | <i>Summary of relevant LHC parameters</i> | 23 |
| 3.2 | <i>General ATLAS performance goals</i> | 25 |
| 3.3 | <i>Relevant parameters of the ATLAS magnet system</i> | 28 |
| 3.4 | <i>Pseudorapidity coverage, granularity and segmentation in layers for each calorimeter</i> | 31 |
| 3.5 | <i>Relevant parameters of the ATLAS muon spectrometer</i> | 34 |
| 4.1 | <i>Samples generated and simulated with the fast simulation</i> | 42 |
| 4.2 | <i>MC generator, cross-section and luminosity for each sample (full simulation)</i> | 50 |
| 4.3 | <i>MC generator and number of available events for systematic uncertainties study</i> | 51 |
| 4.4 | <i>Mean reconstruction efficiencies for each type of generated particles (full simulation)</i> | 53 |
| 4.5 | <i>Signal efficiencies for each trigger level</i> | 56 |
| 4.6 | <i>Background rejections for the single isolated lepton trigger</i> | 56 |
| 5.1 | <i>Number of selected signal and background events after the preselection (fast simulation analysis for $L = 10 \text{ fb}^{-1}$)</i> | 61 |
| 5.2 | <i>Number of selected signal and background events after the final selection (fast simulation analysis for $L = 10 \text{ fb}^{-1}$)</i> | 63 |
| 5.3 | <i>Efficiencies for each reconstructed objects (fast simulation analysis for $L = 10 \text{ fb}^{-1}$)</i> | 67 |
| 5.4 | <i>Theoretical and reconstructed values of helicity fractions, helicity ratios and angular asymmetries for $L = 10 \text{ fb}^{-1}$.</i> | 69 |
| 5.5 | <i>Sources of systematic error in the determination of helicity fractions, helicity ratios and angular asymmetries (fast simulation analysis for $L = 10 \text{ fb}^{-1}$)</i> | 71 |
| 5.6 | <i>Results obtained from the simulation for the observables studied, including statistical and systematic uncertainties (fast simulation analysis for $L = 10 \text{ fb}^{-1}$)</i> | 72 |

| | | |
|------|---|----|
| 5.7 | <i>Expected number of signal and background events after the preselection ($L = 1 \text{ fb}^{-1}$ analysis without b-tagging)</i> | 76 |
| 5.8 | <i>Number of selected signal and background composition for each selection level ($L = 1 \text{ fb}^{-1}$ analysis without b-tagging)</i> | 79 |
| 5.9 | <i>Efficiencies for each reconstructed object in the $L = 1 \text{ fb}^{-1}$ analysis without b-tagging</i> | 83 |
| 5.10 | <i>Number of selected signal (S) and background (B) composition for each selection level ($L = 1 \text{ fb}^{-1}$ analysis with b-tagging)</i> | 85 |
| 5.11 | <i>Efficiencies for each reconstructed object in the $L = 1 \text{ fb}^{-1}$ analysis with b-tagging</i> | 89 |
| 5.12 | <i>Expected values and corresponding statistical errors for the helicity fractions, helicity ratios and angular asymmetries ($L = 1 \text{ fb}^{-1}$ analyses with and without b-tagging)</i> | 91 |
| 5.13 | <i>Sources of systematic error for the $L = 1 \text{ fb}^{-1}$ full simulation analysis without b-tagging</i> | 93 |
| 5.14 | <i>Sources of systematic error for the $L = 1 \text{ fb}^{-1}$ full simulation analysis with b-tagging</i> | 93 |
| 5.15 | <i>Results obtained from the simulation for the observables studied, including statistical and systematic uncertainties (full simulation analysis without b-tagging for $L = 10 \text{ fb}^{-1}$)</i> | 94 |
| 5.16 | <i>Results obtained from the simulation for the observables studied, including statistical and systematic uncertainties (full simulation analysis with b-tagging for $L = 10 \text{ fb}^{-1}$)</i> | 94 |
| 6.1 | <i>Expected 1σ limits on anomalous couplings obtained from the different observables ($L = 10 \text{ fb}^{-1}$)</i> | 96 |
| 6.2 | <i>Correlation matrix for A_{\pm}, $\rho_{R,L}$ ($L = 10 \text{ fb}^{-1}$ analysis)</i> | 97 |
| 6.3 | <i>Correlation matrix for A_{\pm}, $\rho_{R,L}$ ($L = 1 \text{ fb}^{-1}$ analyses)</i> | 97 |
| 6.4 | <i>Expected 1σ limits on the Wtb anomalous couplings for luminosities of 1 fb^{-1} and 10 fb^{-1} obtained from the $\rho_{L,R}$ and A_{\pm} observables (only one anomalous coupling was allowed to be nonzero at a time)</i> | 98 |
| 6.5 | <i>Expected 1σ limits on the Wtb anomalous couplings for $L = 10 \text{ fb}^{-1}$ (two anomalous couplings were allowed to be nonzero at a time)</i> | 98 |

Chapter 1

INTRODUCTION

THE LARGE HADRON COLLIDER at CERN is expected to start operating by the end of Summer 2008. Due to an unprecedented centre of mass energy and luminosity, it will be a top quark factory. This will allow to perform precision tests of the properties of this quark, which is almost as heavy as a gold atom. It should be noticed that the top quark mass was measured with a precision of $\sim 1\%$ at the Tevatron [1], which is much better than the measurements of the remaining quark masses.

The large mass of the top quark makes it a natural candidate for the study of the electroweak symmetry breaking mechanism, as well as to test physics beyond the Standard Model (SM). Although the Tevatron results for top quark physics are, so far, in agreement with the predictions of the SM, its centre of mass energy and collected luminosity have not yet allowed for precision measurements, with the exception of its mass. In particular, questions on top quark production and decay mechanisms remain, to large extent, unanswered. These questions will be addressed by the LHC experiments (in particular ATLAS and CMS).

The large top quark mass has still another consequence: being heavier than the W -boson, it can decay to bW (both on-shell). Within the SM, the $t \rightarrow bW$ decay is the almost exclusive top decay mode. Moreover, as the expectation for the t -quark lifetime is of the order of 10^{-25} s [2, 3], one order of magnitude smaller than the typical hadronization time scale ($\sim 10^{-24}$ s), the top quark decays before hadronization takes place and, consequently, its spin information is transferred to the decay products. For this reason, the angular distributions of the particles originated in a top quark decay can provide information about the Wtb vertex and the top production mechanism.

In the present thesis, the ATLAS prospects for the study of the Wtb vertex structure are discussed. This work is organized as follows. After a brief review of the SM and the top quark in chapter 2, the LHC and the ATLAS experiment will be

presented in chapter 3. The Monte Carlo generation and simulation of signal and background events is discussed in chapter 4, while the event analysis is described in chapter 5. Finally, the expected constraints on the anomalous Wtb couplings are presented in chapter 6 and some conclusions are drawn in chapter 7.

Chapter 2

THE TOP QUARK AND THE Wtb VERTEX

THE STANDARD MODEL of particle physics is a gauge theory which incorporates the electroweak theory (EW) [4, 5, 6] and quantum chromodynamics (QCD) [7, 8]. In the present chapter, a brief introduction to the SM is made (section 2.1), with emphasis in the top quark (section 2.2) and in the Wtb vertex structure (section 2.3). In particular, possible anomalous (*i.e.* beyond the SM) couplings associated to this vertex are discussed and different observables allowing to test them are proposed.

2.1 The Standard Model

Although the SM symmetry group is not a theoretical prediction, $SU(2)_L \otimes U(1)_Y \otimes SU(3)_C$ is consistent with the known phenomenology. It is the direct product of three gauge groups and the couplings for each group (g , g' and g_s) have to be determined. The $SU(2)_L \otimes U(1)_Y$ and $SU(3)_C$ groups are associated with the EW and QCD theories, respectively.

The SM lagrangian, \mathcal{L}_{SM} , embodies the present knowledge of the electroweak and strong interactions. It can be divided into four sectors:

$$\mathcal{L}_{SM} = \mathcal{L}_{\text{gauge}} + \mathcal{L}_{\text{matter}} + \mathcal{L}_{\text{Higgs}} + \mathcal{L}_{\text{Yukawa}} . \quad (2.1)$$

The $\mathcal{L}_{\text{gauge}}$ term describes the pure gauge interactions. The kinetic energy and the self interactions of the strong and electroweak fields are included in this sector.

The gauge interactions of the fermion (matter) fields, ψ_i , are included in $\mathcal{L}_{\text{matter}}$. These matter fields, associated to quarks and leptons of spin 1/2, are multiplets

classified according to their helicity state: left handed (LH) doublets of $SU(2)_L$ and right handed (RH) singlets of $U(1)_Y$:

$$\psi_i = \begin{pmatrix} u_i \\ d_i \end{pmatrix}_L, u_{iR}, d_{iR} \quad (\text{for quarks}) \quad (2.2)$$

and

$$\psi_i = \begin{pmatrix} \nu_i \\ \ell_i \end{pmatrix}_L, \ell_{iR} \quad (\text{for leptons}), \quad (2.3)$$

where u_i (d_i) stands for an up-type (down-type) quark, ℓ_i represents a charged lepton and ν_i a neutrino. The index i runs over the number of fermion generations and the R (L) index stands for the right (left) handedness of the fermions.

The number of SM-like quark and lepton generations has to be equal, *i.e.* although the number of fermion generations is a free parameter of the theory, the same number of SM-like lepton and quark families is required in order to cancel gauge anomalies in higher order calculations. This cancellation is necessary for the renormalizability of the theory [9, 10].

The introduction of mass terms in the lagrangian would explicitly break the local gauge symmetry. A possibility for the gauge bosons to acquire mass is through a mechanism of spontaneous symmetry breaking.¹ In the SM, this is achieved by introducing the Higgs field [11, 12]. This field has a finite vacuum expectation value and its inclusion in the theory leads to the prediction of a massive scalar boson, the Higgs boson, which has not yet been discovered. The characterization of the Higgs field requires two parameters (μ and λ), which can be related with the vacuum expectation value (v) and the Higgs boson mass (m_H).² The Higgs sector of the theory, containing scalar kinetic terms and the Higgs potential, is included in the SM lagrangian by the term $\mathcal{L}_{\text{Higgs}}$.

In the SM, the fermions acquire mass via Yukawa couplings to the Higgs field, which are included in $\mathcal{L}_{\text{Yukawa}}$. The SM assumes that there are no right handed neutrinos and therefore they are expected to be massless. Nevertheless, a few years ago the Super-Kamiokande [14], K2K [15], SNO [16] and KamLAND [17] collaborations reported an evidence for neutrino oscillations, which indicates that neutrinos are massive. The extensions of the SM to accommodate massive neutrinos are beyond the scope of this thesis.³

After the spontaneous symmetry breaking, the bosonic sector of the SM has one scalar field, corresponding to the neutral Higgs boson (H) two charged bosons (W^+ and W^-), two neutral bosons (Z and γ) and eight colored gluons (g). The gluons have an additional quantum number, the color (C), and are responsible for the strong

¹ The difference is important because the theory with spontaneous symmetry breaking is renormalizable.

² See, for instance, Ref. [13].

³ A recent review on neutrino physics can be found in Ref. [18]. Possible extensions of the SM to accommodate massive neutrinos and its implications are discussed, for instance, in Refs. [19, 20, 21, 22, 23, 24, 25].

interaction between quarks. Each quark exists in three color versions (red, green or blue).

The charged currents (CC) induce a mixing between the different generations of quarks. By convention, this mixing is described as a rotation of the down-type quarks, parameterised in terms of the Cabibbo-Kobayashi-Maskawa (CKM) matrix [26], V . For n generations of quarks, V is a $n \times n$ unitary matrix, whose elements have to be determined. Flavour changing neutral currents (FCNC) are absent at tree level but, through CKM mixing, can naturally appear at one-loop level [27].

The weak hypercharge, Y , is defined as $Y = 2(Q - T_3)$, where Q is the fermion electric charge (in units of the positron charge, e) and T_3 is the third component of the weak isospin operator (\hat{T}). The quantum numbers of the SM fermions and bosons are summarized in table 2.1.

| | | T | T_3 | Y | Q | C |
|--------------|-------------|-----|-------|------|------|-------|
| leptons | ν_{iL} | 1/2 | +1/2 | -1 | 0 | — |
| | ℓ_{iL} | 1/2 | -1/2 | -1 | -1 | — |
| | ℓ_{iR} | 0 | 0 | -2 | -1 | — |
| quarks | u_{iL} | 1/2 | +1/2 | +1/3 | +2/3 | R,G,B |
| | d_{iL} | 1/2 | -1/2 | +1/3 | -1/3 | R,G,B |
| | u_{iR} | 0 | 0 | +4/3 | +2/3 | R,G,B |
| | d_{iR} | 0 | 0 | -2/3 | -1/3 | R,G,B |
| gauge bosons | B^0 | 0 | 0 | 0 | 0 | — |
| | W^+ | 1 | +1 | 0 | +1 | — |
| | W^0 | 1 | 0 | 0 | 0 | — |
| | W^- | 1 | -1 | 0 | -1 | — |
| | gluons | 0 | 0 | 0 | 0 | (RGB) |
| Higgs | H | 1/2 | -1/2 | 1 | 0 | — |

Table 2.1: *The quantum numbers of the Standard Model particles are shown. To each fermion corresponds an anti-particle with opposite charge, but the same mass. The index i runs over the number of fermion generations and the R (L) index stands for the fermion helicity. The electric charges, Q , are normalized to the positron charge. R , G and B stand for the possible color charges (red, green and blue). The photon (γ) and the Z bosons are linear combinations of the B^0 and W^0 bosonic fields.*

The gauge and Higgs sectors of the SM depend on five parameters: the three gauge couplings (g , g' and g_s) and the two Higgs field parameters (v and μ). These parameters can be related by the following experimentally measurable quantities ⁴:

$$\alpha_{em} = \frac{(g \sin \theta_w)^2}{4\pi}, \quad \tan \theta_w = \frac{g}{g'}, \quad m_Z^2 = \frac{g^2 v^2}{2 \cos^2 \theta_w}, \quad m_H = \sqrt{2} \mu.$$

The g_s coupling is related with the strong coupling constant (α_s) ⁵. The measured

⁴ The choice of this set of observables is not unique. For example, the W -boson mass ($m_W = gv/2$) or the Fermi constant, $G_F = 1/(2v^2)$, could also be chosen.

⁵ Details can be found, for instance, in Ref. [28].

values of these quantities and the 95% CL limits on the Higgs mass are shown in table 2.2.

| quantity | value | uncertainty (ppb) |
|----------------------|--|-------------------|
| $\alpha_{em}(Q^2=0)$ | $7.297\,352\,5376(50) \times 10^{-3} (\epsilon_0 \hbar c)$ | 0.68 |
| $\sin\theta_w(m_Z)$ | 0.23152(14) | 6.5×10^5 |
| $\alpha_s(m_Z)$ | 0.1176(20) | 1.7×10^7 |
| m_Z | 91.1876(21) GeV | 2.3×10^4 |
| m_H | $114 \text{ GeV} < m_H < 144 \text{ GeV}$ | — |

Table 2.2: *Experimental observables [29] which can be used to define the SM gauge couplings. The 95% CL bounds on the Higgs mass are also shown: the lower bound was obtained from the direct searches at LEP [30] and the upper bound was set by the electroweak precision data [31]. The uncertainty associated to each measured value is expressed in parts per 10^9 (ppb).*

In a three generations scenario ⁶, there are six quarks, three charged leptons and three neutrinos. The masses of the quarks and charged leptons are free parameters of the SM to be determined experimentally (c.f. table 2.3).

| generation | quark | mass (GeV) | charged lepton | mass (GeV) |
|------------|-------|--|----------------|--------------------------------|
| first | u | 1.5×10^{-3} to 3.0×10^{-3} | e | $0.51099892(4) \times 10^{-3}$ |
| | d | 3×10^{-3} to 7×10^{-3} | | |
| second | c | 1.25 ± 0.09 | μ | $0.105658369(9)$ |
| | s | $(95 \pm 25) \times 10^{-3}$ | | |
| third | t | 172.6 ± 1.4 | τ | 1.7769 ± 0.0002 |
| | b | 4.70 ± 0.07 | | |

Table 2.3: *Measured values of the known quark and charged lepton masses (three generations of fermions) [29]. The quoted top mass is the combination of the CDF and D0 measurements [1].*

The CKM matrix elements are also free parameters of the SM ⁷. Assuming only three generations and the unitarity of the CKM matrix, 90% confidence level limits on the magnitude of the V_{ij} elements can be obtained from a global fit [29]:

$$\begin{pmatrix} V_{ud} & V_{us} & V_{ub} \\ V_{cd} & V_{cs} & V_{cb} \\ V_{td} & V_{ts} & V_{tb} \end{pmatrix} = \begin{pmatrix} 0.97383^{+0.00024}_{-0.00023} & 0.2272 \pm 0.0010 & (3.96 \pm 0.09) \times 10^{-3} \\ 0.2271 \pm 0.0010 & 0.97296 \pm 0.00024 & (42.21^{+0.10}_{-0.80}) \times 10^{-3} \\ (8.14^{+0.32}_{-0.64}) \times 10^{-3} & (41.63^{+0.12}_{-0.78}) \times 10^{-3} & 0.999100^{+0.000034}_{-0.000004} \end{pmatrix}$$

⁶ The result on the number of light neutrino species [31] supports the formulation of the SM with three families. Moreover, all the known fermions belong to these three generations.

⁷ The 3×3 CKM matrix elements can be parameterised in terms of three angles and one phase [32].

2.2 The top quark

The top quark was discovered by the Fermilab experiments CDF and D0 in 1995 [33, 34]. This discovery completed the three-generation structure of the fundamental particles of the SM. The top mass values measured by the Tevatron experiments [1] are summarized in figure 2.1.

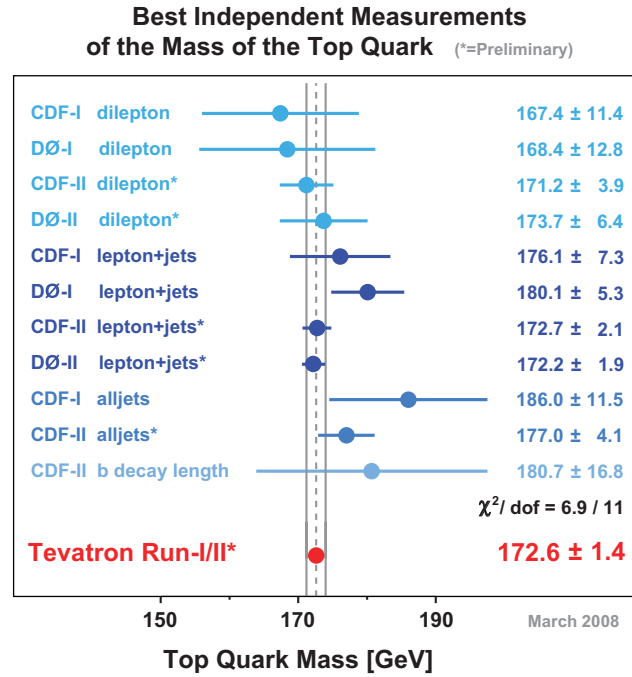


Figure 2.1: Summary and combination of the Tevatron top mass measurements (extracted from Ref. [1]).

The top quark differs from the other SM quarks not only by its large mass, which is close to the electroweak symmetry breaking scale and is approximately 35 times the mass of the b -quark, but also by the fact that it decays almost exclusively through the $t \rightarrow Wb$ mode, and before hadronization can take place. This makes the top quark a very interesting object and an ideal tool for testing the SM predictions and possible new physics beyond the SM.

Several properties of the top quark have already been explored by the Tevatron experiments, such as its mass, its charge, its lifetime, the rare decays through flavour changing neutral currents and the production cross-sections. The structure of the Wtb vertex and the top main decay mode within the SM ($t \rightarrow bW$) were also investigated together with the measurement of the W -boson helicity fractions. Given the current Tevatron luminosity, most of these studies are limited by the small amount of statistics acquired.

2.2.1 Top quark production at the LHC

In hadron colliders, the top quark is predominantly produced in pairs, through quark/anti-quark annihilation or gluon fusion (figure 2.2). At the LHC (unlike the Tevatron) the total production cross-section will be dominated by the gluon fusion process, which amounts to $\sim 90\%$ of the total $t\bar{t}$ production cross-section. According to the SM, top quarks can also be produced in a significant way through electroweak single top production in three different channels: t-channel (figure 2.3a), Wt associated production (figure 2.3b) and s-channel (figure 2.3c).

The next-to-leading-order (NLO) cross-section for $t\bar{t}$ production at the LHC ($\sqrt{s} = 14$ TeV) is 833^{+52}_{-39} pb [35, 2], where the error reflects the uncertainties in the renormalization scale. This cross-section has been calculated at the NLO level in α_s , including next-to-leading logarithms (NLL) soft gluon resummation. More recent calculations [36, 37, 38] found compatible results within the errors.

The total NLO cross-section for the single top production at the LHC is 322 pb: 245 ± 12 for the t-channel [39]; 66 ± 2 pb for the Wt associated production [40]; and 11 ± 1 for the s-channel [39].

2.3 The Wtb vertex

Within the SM the Wtb vertex is purely left-handed, and its size is given by the Cabibbo-Kobayashi-Maskawa matrix element V_{tb} , which can be measured in single top production [41, 42, 43, 44]. In new physics models, departures from the SM expectation $V_{tb} \simeq 1$ are possible [45, 46], as well as new radiative contributions to the Wtb vertex [47, 48]. These corrections can be parameterised with the effective operator formalism. The most general Wtb vertex for on mass shell W , t and b , containing terms up to dimension five can be written as:

$$\begin{aligned} \mathcal{L} = & -\frac{g}{\sqrt{2}} \bar{b} \gamma^\mu (V_L P_L + V_R P_R) t W_\mu^- \\ & -\frac{g}{\sqrt{2}} \bar{b} \frac{i\sigma^{\mu\nu} q_\nu}{m_W} (g_L P_L + g_R P_R) t W_\mu^- + \text{h.c.}, \end{aligned} \quad (2.4)$$

where $q = p_t - p_b$, $P_{L,R} = (1 \mp \gamma_5)$ are the helicity projectors⁸ and $V_{L,R}$ ($g_{L,R}$) are vector-like (tensor-like) couplings. A general Wtb vertex also contains terms proportional to $(p_t + p_b)^\mu$, q^μ and $\sigma^{\mu\nu}(p_t + p_b)_\nu$. Nevertheless, since the b and t -quarks were assumed to be on-shell and the W -bosons decay to light particles whose masses can be neglected, these extra operators can be rewritten in terms of the ones in equation (2.4) using Gordon identities [49]. Additionally, if CP is conserved in the decay, the couplings can be taken to be real.

⁸ The Dirac matrices (γ) satisfy $\{\gamma^\mu, \gamma^\nu\} = \gamma^\mu \gamma^\nu + \gamma^\nu \gamma^\mu = 2g^{\mu\nu}$, where $g^{\mu\nu}$ is the metric tensor (see, for instance, Ref. [49]). Furthermore, $\gamma_5 = \gamma^5 = i\gamma^1\gamma^2\gamma^3\gamma^4$ and $\sigma^{\mu\nu} = \frac{i}{2}[\gamma^\mu, \gamma^\nu] = \frac{i}{2}(\gamma^\mu\gamma^\nu - \gamma^\nu\gamma^\mu)$.

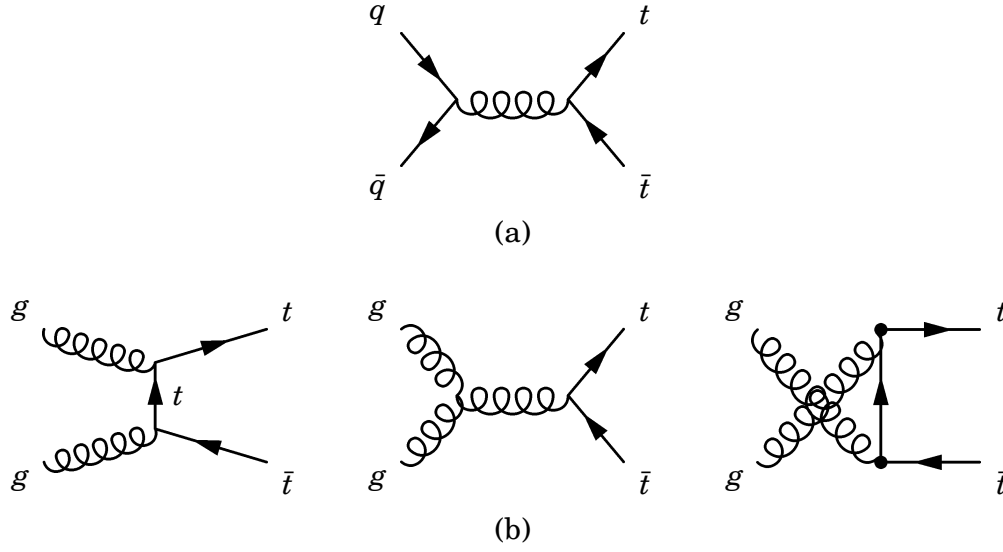


Figure 2.2: *Leading order Feynman diagrams corresponding to the $t\bar{t}$ production at the LHC: (a) $q\bar{q}$ annihilation and (b) gluon fusion.*

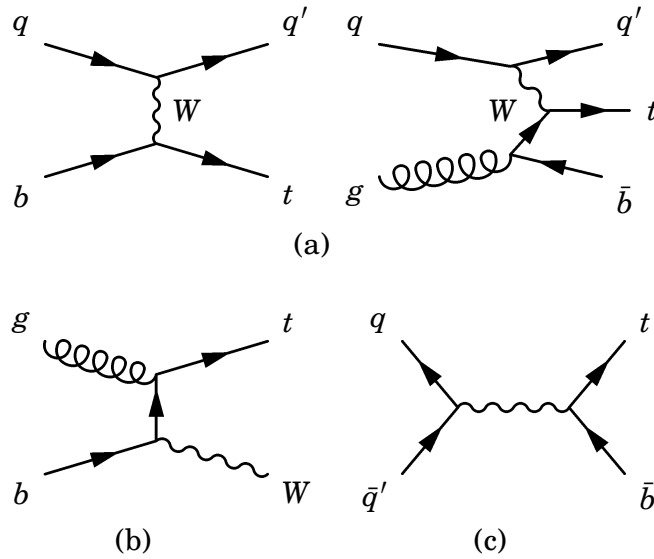


Figure 2.3: *Examples of leading order Feynman diagrams corresponding to the single top production at the LHC: (a) t -channel; (b) Wt associated production and (c) s -channel.*

Within the SM, $V_L \equiv V_{tb} \simeq 1$ and V_R , g_L , g_R vanish at the tree level, while nonzero values are generated at one loop level [50]. Additional contributions to V_R , g_L , g_R are possible in SM extensions, without spoiling the agreement with low-energy measurements [19].

Rare decays of the B -mesons, as well as the $B\bar{B}$ mixing, can provide constraints on the anomalous Wtb couplings, because they receive large contributions from loops involving the top quark and the W -boson. Taking into account the current world average on the $B \rightarrow s\gamma$ branching ratio (BR) [51]:

$$BR(b \rightarrow s\gamma) = [3.55 \pm 0.24^{+0.09}_{-0.10}(\text{experiment}) \pm 0.03(\text{theory})] \times 10^{-4}, \quad (2.5)$$

indirect limits on the anomalous couplings can be evaluated [19, 52]. These bounds, shown in table 2.4, have been obtained under the assumption that the non-linear terms in the theoretical calculation of $BR(b \rightarrow s\gamma)$ are negligible when compared with the linear ones. If this assumption is relaxed, additional solutions are found. Furthermore, this limits were obtained assuming that only one anomalous coupling is different from zero at a time. If different couplings are simultaneously turned on in a correlated manner, their magnitudes are, in principle, not bounded by $b \rightarrow s\gamma$ low energy measurements alone [19].

| | $V_L - V_{tb}$ | V_R | g_L | g_R |
|-------------|----------------|---------|---------|-------|
| upper bound | 0.03 | 0.0025 | 0.0004 | 0.57 |
| lower bound | -0.13 | -0.0007 | -0.0015 | -0.15 |

Table 2.4: *Indirect limits on the Wtb anomalous couplings, obtained from the $BR(b \rightarrow s\gamma)$ measurement. Table extracted from Ref. [52].*

The top quark production and decay processes at LHC will allow to probe the Wtb vertex [42, 44, 53, 54, 55]. $t\bar{t}$ pairs production takes place through QCD interactions without involving a Wtb coupling. Additionally, it is likely that the top quark decays almost exclusively in the $t \rightarrow W^+ b$ channel. Therefore, its cross-section for production and decay $gg, q\bar{q} \rightarrow t\bar{t} \rightarrow W^+ b W^- \bar{b}$ is insensitive to the size and structure of the Wtb vertex. However, the angular distributions of top (anti-top) decay products give information about its structure, and can be used to probe non-standard couplings. The angular distributions relating top and anti-top decay products probe not only the Wtb interactions but also the spin correlations among the two quarks produced, and thus may be influenced by new production mechanisms as well. On the other hand, single top quark production is sensitive to both the size and the structure of the Wtb vertex, involved in the production and the decay of the top quark

2.3.1 W-boson helicity fractions and ratios

The polarisation of the W -bosons emitted in the top quark decay is sensitive to non-standard couplings [56]. The W -bosons can be produced with positive (right-handed), negative (left-handed) or zero helicity, with corresponding partial widths (Γ_R , Γ_L and Γ_0) defined in relation to the total width: $\Gamma \equiv \Gamma(t \rightarrow W^+ b) = \Gamma_R + \Gamma_L + \Gamma_0$. The Γ_R component vanishes in the $m_b = 0$ limit because the b quarks produced in top decays have left-handed chirality, and for vanishing m_b the helicity and the chirality states coincide (figure 2.4).

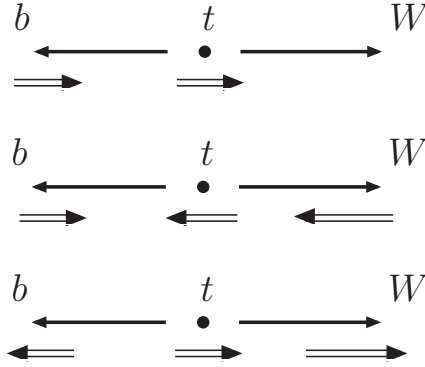


Figure 2.4: Schematic representation of the top quark decay into a b quark and a W -boson with positive (right-handed), negative (left-handed) or zero helicity. The double arrows represent the spin of the particles, while the single arrows stand for their momenta. For convenience, this process is represented in the top quark rest frame. When the W -boson is produced with right-handed helicity, the b quark must have positive helicity (to lowest order), which has vanishing probability for $m_b \rightarrow 0$. Figure extracted from Ref. [3].

The partial widths corresponding to the three W -boson helicities depend on the Wtb anomalous couplings. This dependence was calculated in Ref. [57]:

$$\begin{aligned} \Gamma_0 &= \frac{g^2 |\vec{q}|}{32\pi} \left\{ \frac{m_t^2}{m_W^2} [|V_L|^2 + |V_R|^2] (1 - x_W^2 - 2x_b^2 - x_W^2 x_b^2 + x_b^4) - 4x_b \operatorname{Re} V_L V_R^* \right. \\ &\quad + [|g_L|^2 + |g_R|^2] (1 - x_W^2 + x_b^2) - 4x_b \operatorname{Re} g_L g_R^* \\ &\quad - 2 \frac{m_t}{m_W} \operatorname{Re} [V_L g_R^* + V_R g_L^*] (1 - x_W^2 - x_b^2) \\ &\quad \left. + 2 \frac{m_t}{m_W} x_b \operatorname{Re} [V_L g_L^* + V_R g_R^*] (1 + x_W^2 - x_b^2) \right\}, \\ \Gamma_{R,L} &= \frac{g^2 |\vec{q}|}{32\pi} \left\{ [|V_L|^2 + |V_R|^2] (1 - x_W^2 + x_b^2) - 4x_b \operatorname{Re} V_L V_R^* \right. \\ &\quad \left. + \frac{m_t^2}{m_W^2} [|g_L|^2 + |g_R|^2] (1 - x_W^2 - 2x_b^2 - x_W^2 x_b^2 + x_b^4) - 4x_b \operatorname{Re} g_L g_R^* \right\} \end{aligned}$$

$$\begin{aligned}
& -2 \frac{m_t}{m_W} \text{Re} [V_L g_R^* + V_R g_L^*] (1 - x_W^2 - x_b^2) \\
& + 2 \frac{m_t}{m_W} x_b \text{Re} [V_L g_L^* + V_R g_R^*] (1 + x_W^2 - x_b^2) \Big\} \\
& \pm \frac{g^2}{64\pi} \frac{m_t^3}{m_W^2} \{ -x_W^2 [|V_L|^2 - |V_R|^2] + [|g_L|^2 - |g_R|^2] (1 - x_b^2) \\
& + 2x_W \text{Re} [V_L g_R^* - V_R g_L^*] + 2x_W x_b \text{Re} [V_L g_L^* - V_R g_R^*] \} \\
& \times (1 - 2x_W^2 - 2x_b^2 + x_W^4 - 2x_W^2 x_b^2 + x_b^4), \tag{2.6}
\end{aligned}$$

with $x_W = m_W/m_t$, $x_b = m_b/m_t$ and

$$|\vec{q}| = \frac{1}{2m_t} (m_t^4 + m_W^4 + m_b^4 - 2m_t^2 m_W^2 - 2m_t^2 m_b^2 - 2m_W^2 m_b^2)^{1/2} \tag{2.7}$$

being the modulus of the W -boson momentum in the top quark rest frame.

The total top quark width is given by

$$\begin{aligned}
\Gamma = & \frac{g^2 |\vec{q}|}{32\pi} \frac{m_t^2}{m_W^2} \{ [|V_L|^2 + |V_R|^2] (1 + x_W^2 - 2x_b^2 - 2x_W^4 + x_W^2 x_b^2 + x_b^4) \\
& - 12x_W^2 x_b \text{Re} V_L V_R^* + 2 [|g_L|^2 + |g_R|^2] \left(1 - \frac{x_W^2}{2} - 2x_b^2 - \frac{x_W^4}{2} - \frac{x_W^2 x_b^2}{2} + x_b^4 \right) \\
& - 12x_W^2 x_b \text{Re} g_L g_R^* - 6x_W \text{Re} [V_L g_R^* + V_R g_L^*] (1 - x_W^2 - x_b^2) \\
& + 6x_W x_b \text{Re} [V_L g_L^* + V_R g_R^*] (1 + x_W^2 - x_b^2) \}. \tag{2.8}
\end{aligned}$$

The different polarisation states of the W -boson determine the angular distribution of its decay products, namely the angle between the charged lepton momentum in the W rest frame and the W momentum in the t -quark rest frame (θ_ℓ^*). The normalised differential decay rate for unpolarised top quarks can be written as

$$\frac{1}{\Gamma} \frac{d\Gamma}{d\cos\theta_\ell^*} = \frac{3}{8} (1 + \cos\theta_\ell^*)^2 F_R + \frac{3}{8} (1 - \cos\theta_\ell^*)^2 F_L + \frac{3}{4} \sin^2\theta_\ell^* F_0, \tag{2.9}$$

with $F_i \equiv \Gamma_i/\Gamma$ being the W -boson helicity fractions. The three terms correspond to the three helicity states, and the interference terms vanish [58]. Within the SM, at the leading order (LO), the values of these helicity fractions are $F_0 = 0.703$, $F_L = 0.297$, $F_R = 3.6 \times 10^{-4}$, for $m_t = 175$ GeV, $m_W = 80.39$ GeV, $m_b = 4.8$ GeV (the values at NLO are $F_0 = 0.694$, $F_L = 0.304$ and $F_R = 1.5 \times 10^{-3}$ [50]). The resulting distribution is shown in figure 2.5, which was obtained from the analytical expressions in equations (2.6)–(2.9) and also from a Monte Carlo simulation. The latter is performed using the Protos generator [41], which uses the full resonant matrix element for $gg, q\bar{q} \rightarrow t\bar{t} \rightarrow W^+ b W^- \bar{b} \rightarrow f_1 \bar{f}'_1 b \bar{f}'_2 \bar{b}$, and hence takes into account the top and W widths, as well as their polarisations. It can be seen that the finite width corrections have a negligible influence in the distribution, and hence equations (2.6)–(2.9) can be used to make precise predictions for the distributions. The effect of the Wtb anomalous couplings (V_L, V_R, g_L, g_R) on the $\cos\theta_\ell^*$ distribution is shown in figure 2.6.

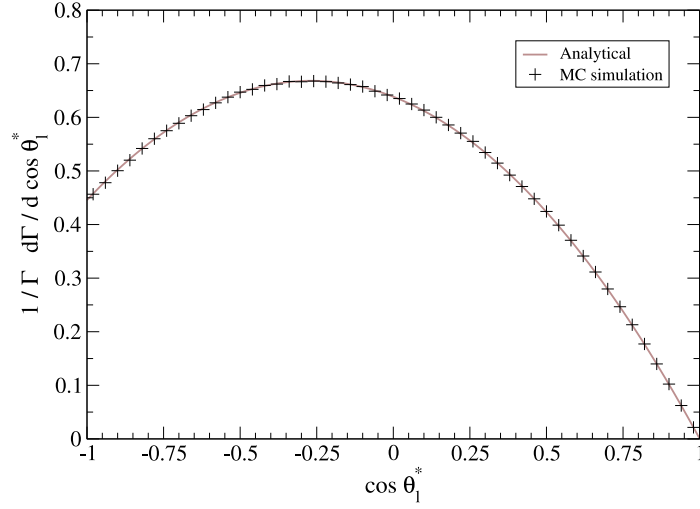


Figure 2.5: SM differential distribution of $\cos\theta_l^*$ (equation 2.9), calculated analytically and with a Monte Carlo generator.

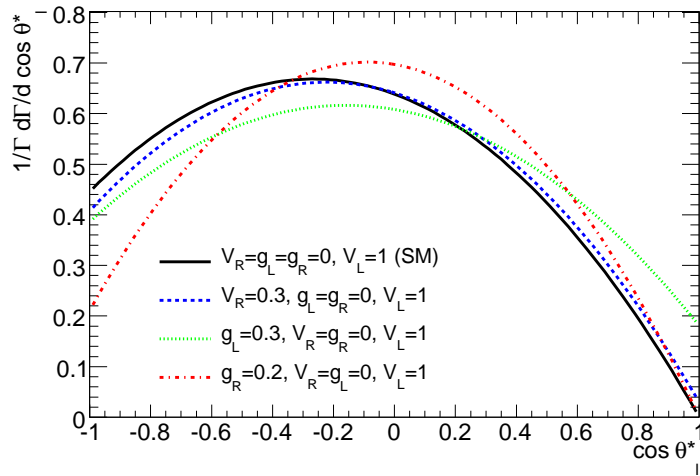


Figure 2.6: Differential distribution of $\cos\theta_l^*$ (equation 2.9), for different values of the Wtb anomalous couplings (V_L, V_R, g_L, g_R).

The present experimental measurements of the W -boson helicity fractions were obtained at the Tevatron by the CDF [59] and D0 [60] collaborations. These limits are shown in figure 2.7.

In the presence of anomalous couplings, the helicity fractions F_i are modified with respect to their SM values. This dependence is shown in figure 2.8, considering that only one coupling is different from zero at a time and assuming the CP-conserving case of real V_R , g_R and g_L . It can be seen that F_L and F_0 are more sensitive to g_R than to g_L and V_R . This is due to the interference term $V_L g_R^*$, which is not suppressed by the bottom quark mass, as it happens for the g_L and V_R couplings. This linear term dominates over the quadratic one and makes the helicity fractions (and related quantities) very sensitive to g_R . It should also be noticed that the phases of the anomalous couplings influence the helicity fractions through the interference terms, which depend on the real part of V_R , g_L and g_R . V_L was assumed to be real, and normalised to unity.

The sensitivity achieved for non-standard couplings may be improved if, instead of the helicity fractions, their ratios are considered:

$$\rho_{R,L} \equiv \frac{\Gamma_{R,L}}{\Gamma_0} = \frac{F_{R,L}}{F_0}, \quad (2.10)$$

which are independent quantities and take the values of $\rho_R = 5.1 \times 10^{-4}$ and $\rho_L = 0.423$ in the SM (LO).⁹ The dependence of these helicity ratios on the anomalous couplings is shown in figure 2.9.

The importance of keeping the bottom quark mass in the calculations has to be stressed. Within the SM the m_b correction to the helicity fractions is small, of the order of $x_b^2 = 7.5 \times 10^{-4}$, as can be seen in the equations 2.6. It should be noticed, however, that the interference terms involving g_L or V_R couplings with V_L are proportional to $x_b = 0.027$, and are of the same order of magnitude as the quadratic terms. The effect of including m_b in the computations is illustrated with more detail in appendix A.

⁹ The SM NLO values are $\rho_R = 1.4 \times 10^{-3}$ and $\rho_L = 0.438$.

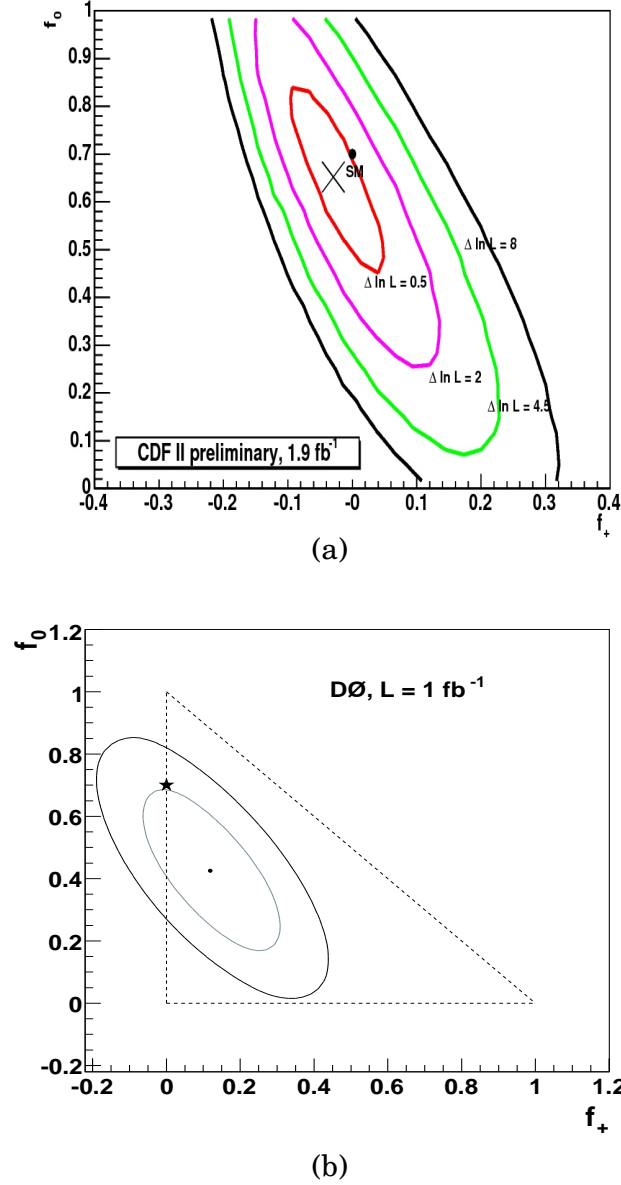


Figure 2.7: W -boson helicity fractions measurements by the Tevatron experiments. (a) CDF result with $L = 1.9 \text{ fb}^{-1}$: the figure, extracted from Ref. [59], shows contours of constant likelihood from the fit to the data. The X shows the minimum of the likelihood and the dot represent the SM expectation. (b) D0 result with $L = 1.9 \text{ fb}^{-1}$: the figure, extracted from Ref. [60], shows the obtained result (dot) and the SM expectation (star). The external ellipse represents the 95% CL contour and the dashed triangle shows the physical region for the helicity fractions. The notation used by these collaborations is different from the one adopted in the present thesis: f_0 and f_+ stand for F_0 and F_R , respectively.

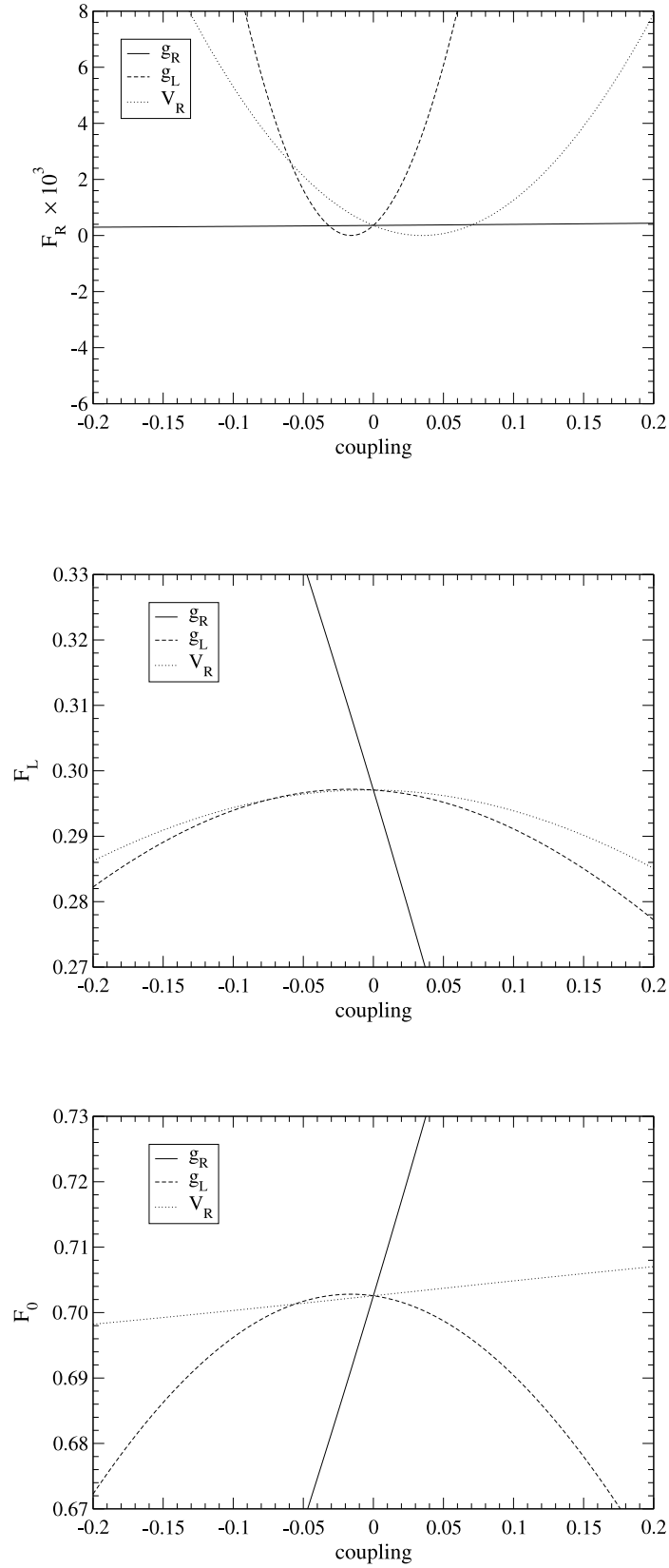


Figure 2.8: *Dependence of the helicity fractions $F_i = \Gamma_i/\Gamma$ on the anomalous couplings (equation 2.4), in the CP-conserving case.*

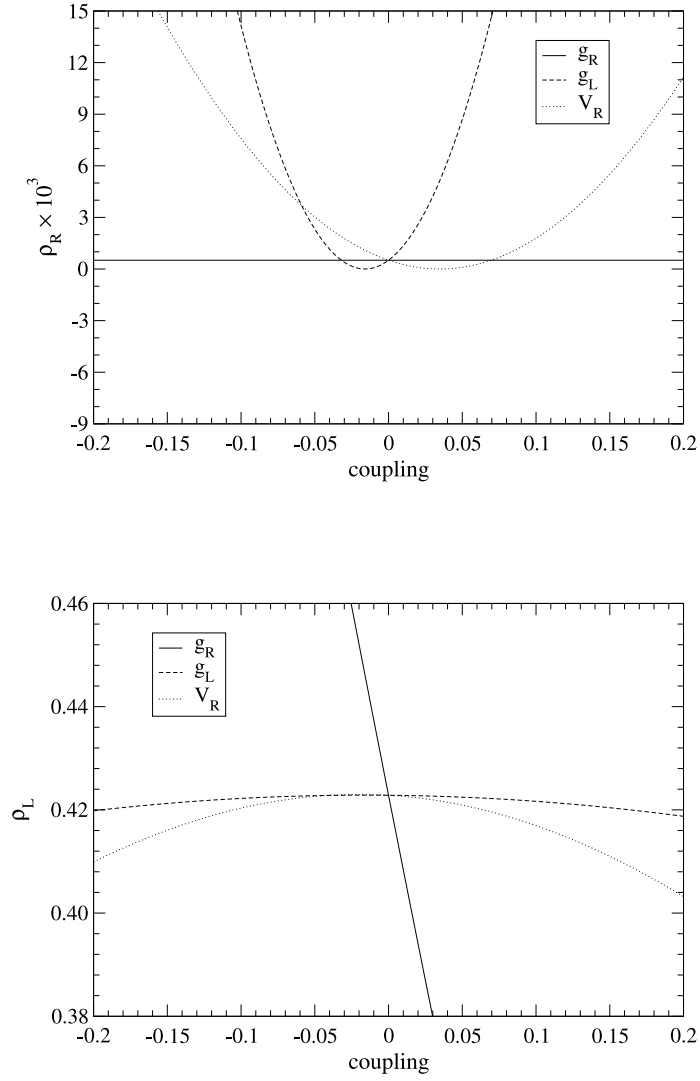


Figure 2.9: *Dependence of the helicity ratios $\rho_{R,L} = \Gamma_{R,L}/\Gamma_0$ on the anomalous couplings (equation 2.4), in the CP-conserving case.*

2.3.2 Angular asymmetries

A simple method to extract information about the Wtb vertex is through angular asymmetries involving the angle θ_ℓ^* between the charged lepton momentum (in the W -boson rest frame) and the W boson momentum (in the top quark rest frame). Alternatively, one may consider the angle $\theta_{\ell b}$ between the charged lepton and b -quark momenta in the W -boson rest frame. Both approaches are equivalent¹⁰ since these two angles are related by $\theta_\ell^* + \theta_{\ell b} = \pi$. For any fixed value of z in the interval $[-1, 1]$, one can define an asymmetry

$$A_z = \frac{N(\cos\theta_\ell^* > z) - N(\cos\theta_\ell^* < z)}{N(\cos\theta_\ell^* > z) + N(\cos\theta_\ell^* < z)}. \quad (2.11)$$

The most obvious choice is $z = 0$, giving the forward-backward (FB) asymmetry A_{FB} [61, 53].¹¹ It is analogous to the FB asymmetries at LEP, which together with the ratios R_b and R_c [31], allowed to determine the couplings of the c and b quarks to the Z boson [29, 62, 63]. The FB asymmetry is related to the W -boson helicity fractions by

$$A_{\text{FB}} = \frac{3}{4}[F_R - F_L]. \quad (2.12)$$

The measurement of this asymmetry alone is not enough to fully reconstruct the $\cos\theta_\ell^*$ distribution. Other asymmetries, for different values of z , have therefore to be considered. The determination of F_i is easier if asymmetries involving only F_R and F_0 , or F_L and F_0 are chosen. This is achieved by choosing $z = \mp(2^{2/3} - 1)$:

$$\begin{aligned} z = -(2^{2/3} - 1) &\rightarrow A_z = A_+ = 3\beta[F_0 + (1 + \beta)F_R], \\ z = (2^{2/3} - 1) &\rightarrow A_z = A_- = -3\beta[F_0 + (1 + \beta)F_L], \end{aligned} \quad (2.13)$$

where $\beta = 2^{1/3} - 1$. From both asymmetries and using $F_R + F_L + F_0 = 1$, the W -boson helicity ratios can be obtained:

$$\begin{aligned} F_R &= \frac{1}{1 - \beta} + \frac{A_- - \beta A_+}{3\beta(1 - \beta^2)}, \\ F_L &= \frac{1}{1 - \beta} - \frac{A_+ - \beta A_-}{3\beta(1 - \beta^2)}, \\ F_0 &= -\frac{1 + \beta}{1 - \beta} + \frac{A_+ - A_-}{3\beta(1 - \beta)}. \end{aligned} \quad (2.14)$$

The evaluation of these angular asymmetries A_{FB} , A_+ , A_- is represented in figure 2.10, while their dependence with the anomalous couplings is shown in figure 2.11. The SM values for them are $A_{\text{FB}} = -0.2225$, $A_+ = 0.5482$ and $A_- = -0.8397$ (LO).¹²

¹⁰ The experimental determination of $\theta_{\ell b}$, however, is simpler, because both momenta are measured in the same reference frame without any ambiguity in the boosts.

¹¹ There is a difference in sign with respect to the definitions in Refs. [61, 53], where $\theta_{\ell b}$ is used.

¹² The SM NLO values are $A_{\text{FB}} = -0.2270$, $A_+ = 0.5429$ and $A_- = -0.8402$.

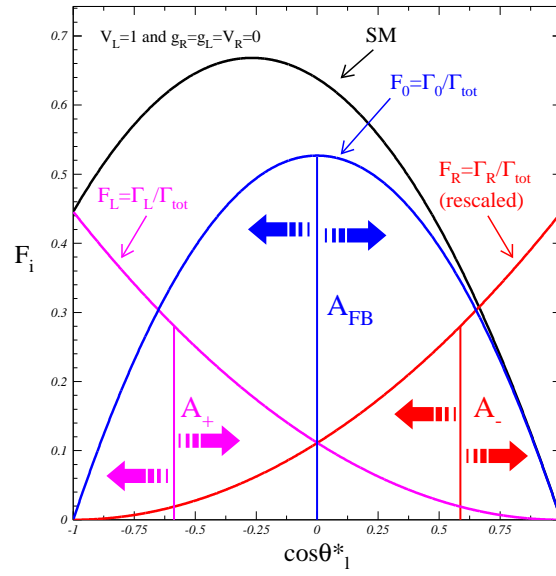


Figure 2.10: Considered angular asymmetries involving the angle θ_ℓ^* between the charged lepton momentum (in the W -boson rest frame) and the W -boson momentum (in the top quark rest frame).

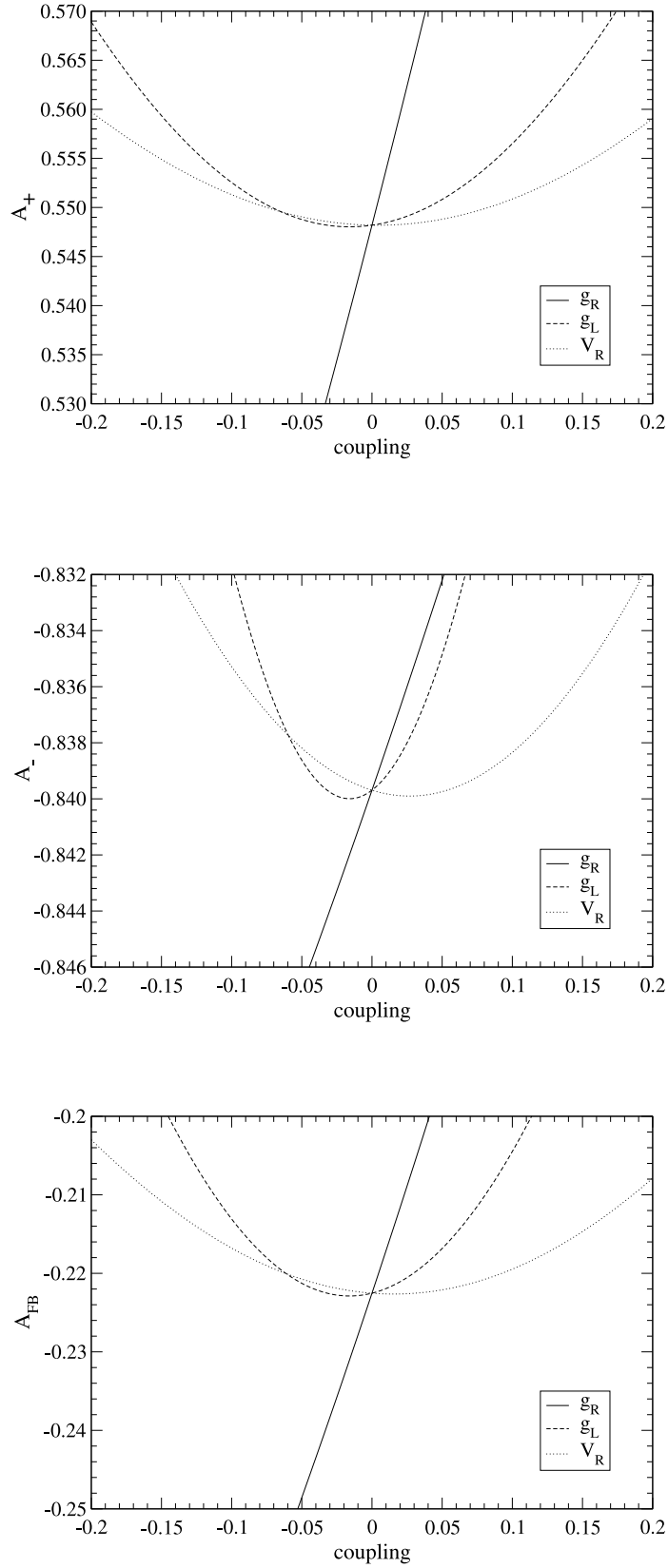


Figure 2.11: *Dependence of the angular asymmetries A_+ , A_- and A_{FB} on the couplings g_L , g_L and V_R , for the CP-conserving case.*

Chapter 3

THE ATLAS EXPERIMENT AT THE LHC

THE LARGE HADRON COLLIDER (LHC) will achieve a centre of mass energy and luminosity which will allow to perform precision tests of the SM and to search for new physics in unprecedented conditions. In section 3.1, the LHC injection and acceleration chain is presented. A brief description of the different ATLAS subdetectors, as well as of the trigger, data acquisition and detector control systems, is done in section 3.2.

3.1 The LHC collider

The LHC [64, 65, 66] is a proton-proton collider currently under installation at CERN (European Organization for Nuclear Research, located near Geneva, Switzerland) and it is expected to start operating by the end of Summer 2008. With a centre of mass energy (\sqrt{s}) of 14 TeV, it represents the next major step in high energy accelerators. The LHC was installed in a 27 km tunnel at a depth ranging from 50 to 175 m underground. It was designed to accelerate two beams of protons ¹, which will collide at four interaction points. The ALICE, ATLAS, CMS and LHC-B detectors are placed in these interaction points (figure 3.1).

The production of high energy protons requires a complex injection and acceleration chain (figure 3.2). Protons will be produced in bunches ² and injected in the linear accelerator LINAC (where they are accelerated up to 50 MeV) and, afterwards, in the Proton Synchrotron Booster (PSB) until they reach 1 GeV. These protons are then accelerated up to 26 GeV in the the Proton Synchrotron (PS) and injected in the Super Proton Synchrotron (SPS), were they reach 450 GeV. Finally, two counter-rotating beams are injected in the LHC, where they are accelerated to 7 TeV.

¹ The LHC will also accelerate ions, but this is beyond the scope of the present thesis.

² The protons will be obtained from hydrogen atoms.

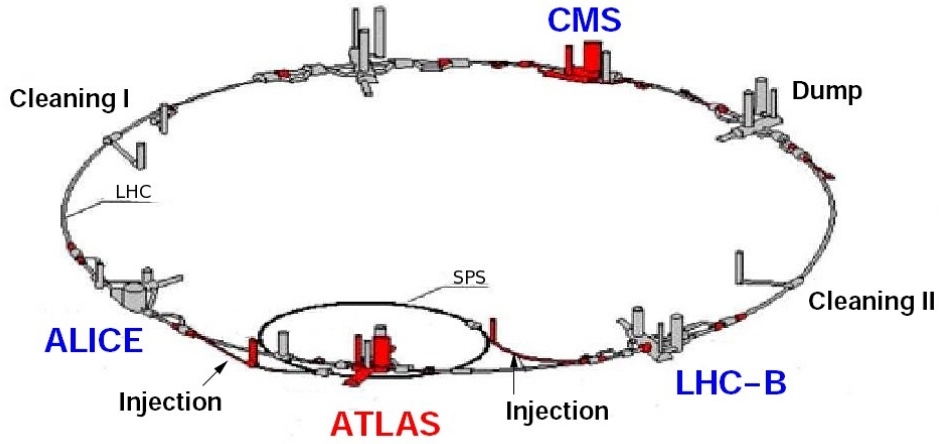


Figure 3.1: Overall view of the LHC and location of the ATLAS, CMS, ALICE and LHC-B experiments.

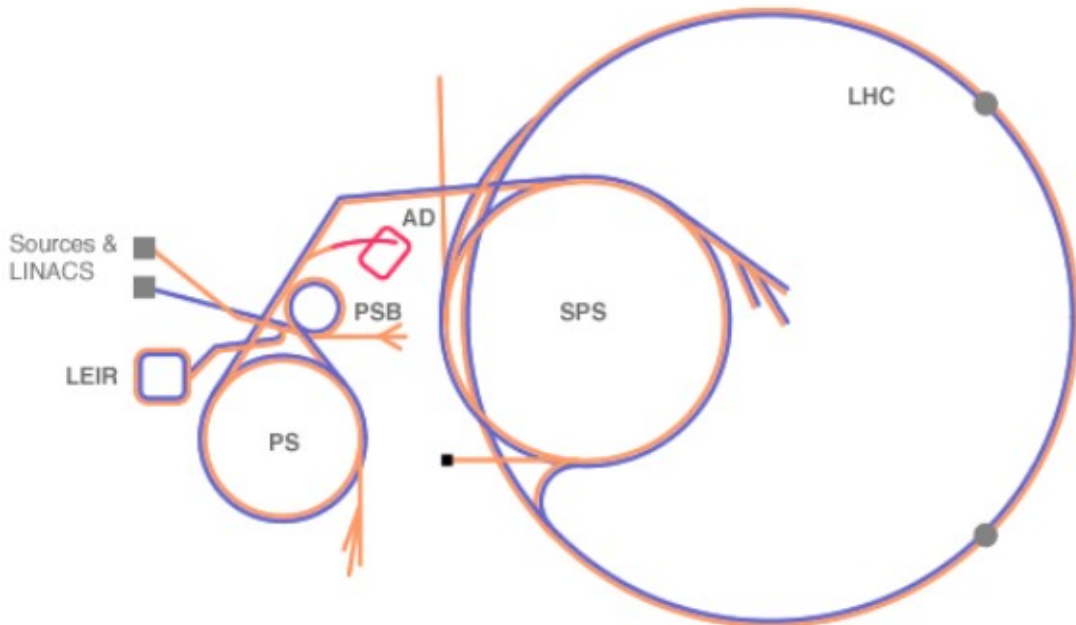


Figure 3.2: Schematic view of the LHC injection and acceleration chain at the CERN accelerators complex.

| | |
|------------------------------------|---|
| proton beam energy | 7 TeV |
| number of particles per bunch | 1.15×10^{11} |
| number of bunches | 2808 |
| circulating beam current | 0.582 A |
| stored energy per beam | 362 MJ |
| mean bunch length | 7.55 cm |
| mean beam diameter (ATLAS and CMS) | 16.7 μm |
| peak luminosity (ATLAS and CMS) | $1.0 \times 10^{34} \text{ cm}^{-2} \text{ s}^{-1}$ |

Table 3.1: *Summary of relevant parameters for the LHC collisions (adapted from [64]).*

The proton bunches will circulate in a vacuum tube and will be manipulated using electromagnetic devices: 1232 dipole magnets will keep the particles in their nearly circular orbits while 392 quadrupole magnets will focus the beams. The dipoles were placed in the curved sections of the LHC and the quadrupoles in the straight ones. These magnets are made of superconducting niobium-titanium (Ni-Ti) cables and will operate at 1.9 K (using superfluid helium for cooling), producing a magnetic field of 8 T. The beams will be accelerated and kept at a constant energy with superconducting radiofrequency (RF) cavities. The LHC will use eight RF cavities per beam. These cavities will be operated at 4.5 K.

In the LHC, under nominal operating conditions, each proton beam will have 2808 bunches, with each bunch containing 1.15×10^{11} protons. The design luminosity is $l = 10^{34} \text{ cm}^{-2} \text{ s}^{-1}$, which corresponds to an integrated luminosity of about $L = 100 \text{ fb}^{-1}$ per year of operation and per experiment (ATLAS and CMS). During the first low luminosity phase, $l = 10^{33} \text{ cm}^{-2} \text{ s}^{-1}$ (corresponding to $L \sim 10 \text{ fb}^{-1}$ per year and per experiment) is expected.

The bunch crossing time will be 25 ns and around 20 collisions are expected per bunch crossing (creating pile-up events). With an inelastic proton-proton cross-section of 60 mb and a much lower rate of interesting events, it is unlikely that more than one interesting event is produced by bunch-crossing. Nevertheless, the extra activity in each interesting event will affect the event reconstruction, especially in the forward region of the detector.

Some of the relevant LHC parameters are summarized in table 3.1.

3.2 The ATLAS detector

The ATLAS experiment ³ uses a general-purpose detector, constructed in several cylindrical layers around the beam pipe and two end-caps, in order to cover

³ ATLAS is an acronym for **A** Toroidal **L**H**C** **A**pparatu**S**. The ATLAS experiment was proposed for operation in 1994 and was approved for construction in 1995 [67].

the maximum possible solid angle around the interaction point (*c.f.* figure 3.3). A detailed review of the ATLAS detector can be found in Ref. [68].

The following requirements were taken into account in the ATLAS detector design.

- Due to the experimental conditions at the LHC, fast, radiation-hard electronics and sensor elements are required. In addition, high detector granularity is needed to handle the expected high particle fluxes and to reduce the influence of pile-up.
- Large angular acceptance.
- Good charged-particle momentum resolution and reconstruction efficiency by the inner tracker detector. For the offline tagging of b -jets and τ -leptons, vertex detectors close to the interaction region have to be able to observe secondary vertices.
- Electromagnetic (EM) calorimetry for electron and photon identification and measurements, complemented by full-coverage hadronic calorimetry for accurate jet and missing transverse energy (\cancel{E}_T) measurements.
- Muon identification and good momentum resolution over a large range of momentum transverse to the beam axis (p_T).
- Forward detectors, aimed to determine the luminosity delivered to ATLAS.
- Highly efficient triggering on low- p_T objects, with good background rejection.

The general performance goals for the ATLAS detector are summarized in table 3.2.

3.2.1 ATLAS coordinate system

The ATLAS coordinate system is represented in figure 3.4. The nominal interaction point is defined as the origin of the coordinate system, while the beam direction defines the z -axis and the $x-y$ plane is transverse to the beam direction. The positive x -axis is defined as pointing from the interaction point to the centre of the LHC ring and the positive y -axis is defined as pointing upwards. The side-A of the detector is defined as that with positive z and side-C is that with negative z . The azimuthal angle ϕ is measured around the beam axis (with $\phi = 0$ corresponding to the x -axis), and the polar angle θ is the angle measured from the beam axis (z -axis). The pseudorapidity is defined as $\eta = -\ln[\tan(\theta/2)]$ and it is represented in figure 3.5. The distance ΔR in the pseudorapidity-azimuthal angle space is defined as $\Delta R = \sqrt{\Delta\eta^2 + \Delta\phi^2}$.

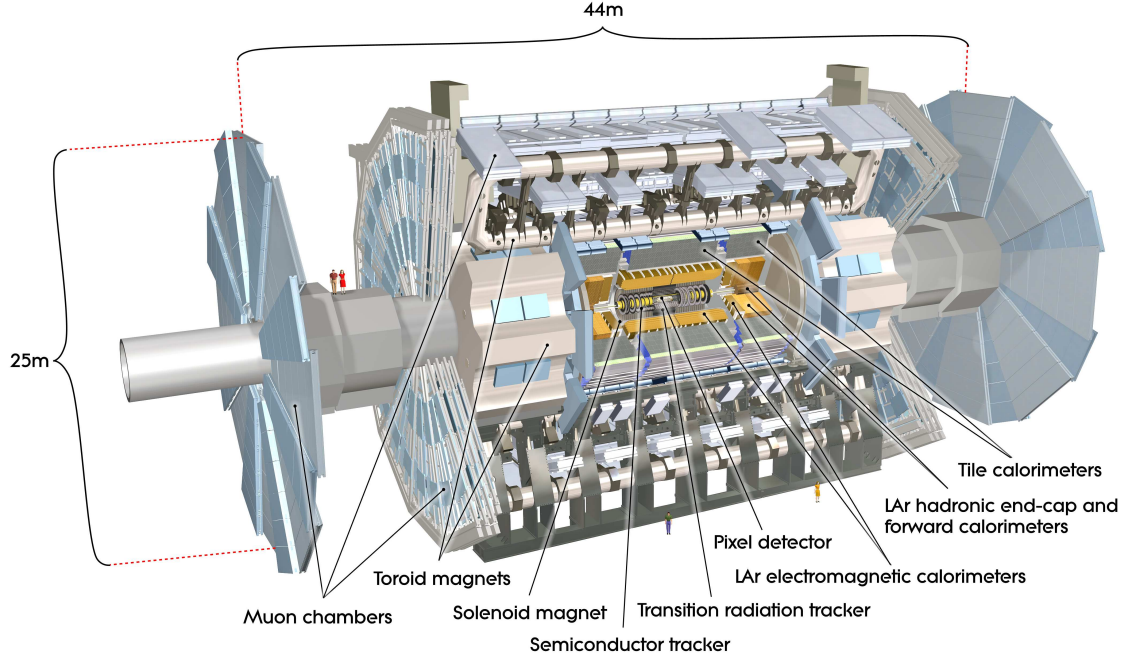


Figure 3.3: Schematic representation of the ATLAS detector (cut-away view). The different subdetectors and magnets are shown (extracted from Ref. [68]).

| detector component | required resolution | η coverage | |
|-----------------------------|---|----------------------|----------------------|
| | | measurement | trigger |
| Tracking | $\sigma_{p_T}/p_T = 0.05\% \times p_T \oplus 1\%$ | $ \eta < 2.5$ | — |
| EM calorimetry | $\sigma_E/E = 10\%/\sqrt{E} \oplus 0.7\%$ | $ \eta < 3.2$ | $ \eta < 2.5$ |
| Hadronic calorimetry (jets) | | | |
| barrel and end-cap | $\sigma_E/E = 50\%/\sqrt{E} \oplus 3\%$ | $ \eta < 3.2$ | $ \eta < 3.2$ |
| forward | $\sigma_E/E = 100\%/\sqrt{E} \oplus 10\%$ | $3.1 < \eta < 4.9$ | $3.1 < \eta < 4.9$ |
| Muon spectrometer | $\sigma_{p_T}/p_T = 10\%$ at $p_T = 1$ TeV | $ \eta < 2.7$ | $ \eta < 2.4$ |

Table 3.2: General performance goals of the ATLAS detector (extracted from Ref. [68]). For high- p_T muons, the muon spectrometer performance is independent of the inner-detector system. The unit for E and p_T is GeV.

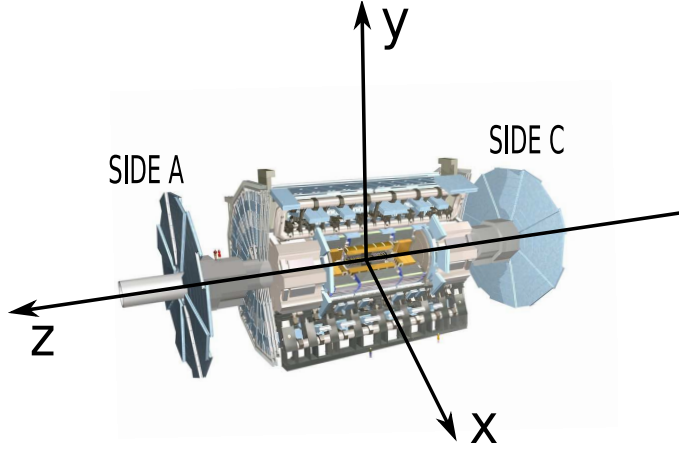


Figure 3.4: *ATLAS coordinate system: the positive x-axis is defined as pointing from the interaction point to the centre of the LHC ring and the positive y-axis is defined as pointing upwards. The side-A of the detector is defined as that with positive z and side-C is that with negative z. The azimuthal angle ϕ is measured around the beam axis (with $\phi = 0$ corresponding to the x-axis), and the polar angle θ is the angle from the beam axis.*

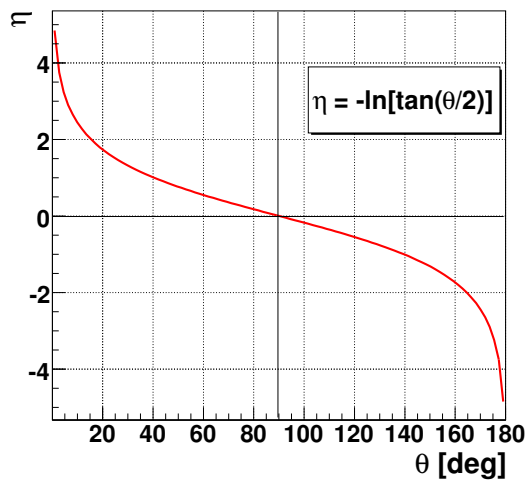


Figure 3.5: *Pseudorapidity (η) as a function of the polar angle (θ).*

3.2.2 Magnet system

ATLAS features a unique hybrid system of four large superconducting magnets. Their geometry, shown in figure 3.6, has conditioned, to large extent, the design of the entire detector. The purpose of this magnet system is the bending of the charged particles produced in the events, allowing to measure their momenta and charge sign.

The ATLAS magnet system [69], whose main parameters are listed in table 3.3, consists of:

- A solenoid, which is aligned with the beam axis and provides a 2 T axially symmetric magnetic field for the inner detector. To achieve the desired calorimeter performance, the layout was carefully optimised to keep the material thickness in front of the calorimeter as low as possible, resulting in a solenoid system thickness of ~ 0.6 radiation lengths at normal incidence [70].
- A barrel and two end-cap toroids, which produce a toroidal magnetic field of 0.5 T and 1 T, respectively, for the muon detectors. The barrel toroid, which consists of eight coils, covers the region $|\eta| < 1.0$ while the end-cap toroids cover $1.4 < |\eta| < 2.7$. The magnetic field in the intermediate region is a combination of the barrel and end-cap toroid contributions.

3.2.3 Inner detector

In order to reconstruct the momenta of the high number of tracks produced by the charged particles emerging from each collision, a detector with a very good granularity and momentum resolution is required. Pixel and silicon microstrip trackers, used in combination with the straw tubes of the transition radiation tracker, can fulfill these requirements.

The ATLAS tracking system, named Inner Detector (ID), is illustrated in figure 3.7. From the inside to the outside of ATLAS, the pixel detector, the semiconductor tracker (SCT) and the transition radiation tracker (TRT) were installed. The ID is immersed in the 2 T magnetic field, generated by the central solenoid.

The high precision tracking detectors (pixels and SCT) cover the region $|\eta| < 2.5$. In the barrel region, they are arranged in concentric cylinders around the beam axis while at the end-cap regions they are located on disks perpendicular to the beam axis. The highest granularity is achieved in the region closer to the interaction point through the use of silicon pixel detectors. The pixel layers are segmented in $R - \phi$ and z with typically three pixel layers crossed by each track. All the pixel sensors are identical and have a minimum size of $R - \phi \times z = 50 \times 400 \mu\text{m}^2$. The intrinsic accuracies of the pixel detectors are $\sigma_{R-\phi} = 10 \mu\text{m}$ and $\sigma_z = 115 \mu\text{m}$ in the barrel, and $\sigma_{R-\phi} = 10 \mu\text{m}$ and $\sigma_R = 115 \mu\text{m}$, in the end-caps. It has approximately 80.4 million read-out channels. The SCT is made of semiconductor strips. In the

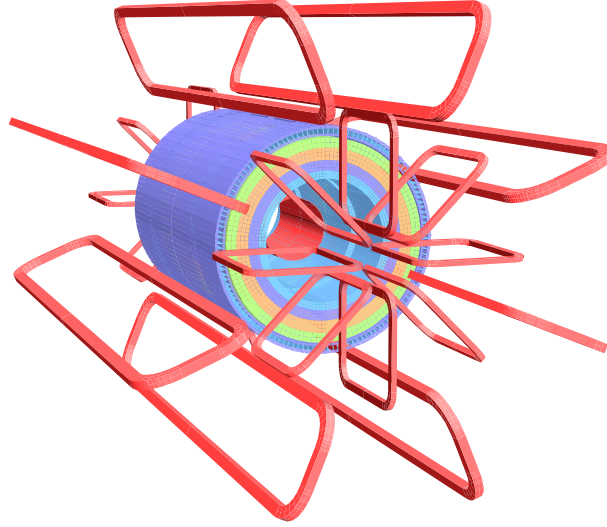


Figure 3.6: *Geometry of the magnets systems. The eight barrel toroid coils, with the end-cap coils interleaved are visible. The solenoid winding lies inside the calorimeter volume. The tile calorimeter is modelled by four layers with different magnetic properties, plus an outside return yoke. (extracted from Ref. [68]).*

| | unit | solenoid | barred toroid | end-cap toroids |
|----------------------|------|-------------|---------------|-----------------|
| Size: | | | | |
| inner diameter | m | 2.46 | 9.4 | 1.65 |
| outer diameter | m | 2.63 | 20.1 | 10.7 |
| axial length | m | 5.29 (cold) | 25.3 | 5.0 |
| number of coils | | 1 | 8 | 2×8 |
| Coils: | | | | |
| turns per coil | | 1154 | 120 | 116 |
| nominal current | kA | 7.73 | 20.5 | 20.5 |
| magnet stored energy | GJ | 0.04 | 1.08 | 2×0.25 |
| peak field | T | 2.6 | 3.9 | 4.1 |
| field range | T | 0.9–2.0 | 0.2–2.5 | 0.2–3.5 |

Table 3.3: *Relevant parameters of the ATLAS magnet systems (extracted from Ref. [68]).*

barrel region, this detector uses small-angle (40 mrad) stereo strips to measure both coordinates, with one set of strips in each layer parallel to the beam direction, measuring $R - \phi$. The intrinsic accuracies of each SCT barrel module are $17 \mu\text{m}$ and $580 \mu\text{m}$, for $R - \phi$ and z , respectively. For the end-cap disks, the accuracies are $17 \mu\text{m}$ and $580 \mu\text{m}$, for $R - \phi$ and R , respectively. The total number of SCT read-out channels is approximately 6.3 million.

The last layer of the ID is the TRT subdetector, which detects the transition radiation produced when a relativistic particle passes through the boundary between materials with different electrical properties. At each interface between materials, the probability of transition radiation increases with the relativistic γ of the radiating particle. For a given energy, this allows a discrimination between lighter and heavier particles (a pion and an electron, for instance). It consists of a large number of straws (with a 4 mm diameter), providing in average 36 measurements per track with an accuracy of $130 \mu\text{m}$ per straw. The total number of TRT read-out channels is approximately 3.5×10^5 .

As showed in table 3.2, the required resolution for tracking is:

$$\frac{\sigma p_T}{p_T} = 0.05\% \times p_T \oplus 1\% .$$

3.2.4 Calorimeter system

The ATLAS calorimeter system is composed by the electromagnetic and hadronic calorimeters, as shown in figure 3.8. The pseudorapidity coverage, granularity and segmentation in layers for each calorimeter are summarized in table 3.4.

The calorimeters must provide good containment for electromagnetic and hadronic showers, and also limit the particles reaching the muon system (only muons and the undetected neutrinos should be able to pass through the calorimeters with very small punch-through). The ATLAS calorimeter system consists of several sampling detectors with full ϕ -symmetry and coverage around the beam axis. The calorimeters closer to the beam-line are housed in three cryostats, one barrel and two end-caps. The barrel cryostat contains the EM barrel calorimeter, whereas each of the two end-cap cryostats contains an EM calorimeter.

The EM calorimeter [71, 68] is a sampling calorimeter made of layers of lead (used as the passive material), built in an accordion-shape. Between the layers, liquid argon (LAr) is used as the active material. The accordion geometry provides complete ϕ symmetry without azimuthal cracks. The lead thickness in the absorber plates has been optimised to achieve the best possible performance in energy resolution. This calorimeter has an integrated presampler layer, located behind a cryostat wall in the region $|\eta| < 1.8$. The presampler consists of an active LAr layer with a thickness of 1.1 cm (0.5 cm) in the barrel (end-cap) region and it is used to correct for the energy lost by electrons and photons upstream of the calorimeter. The EM calorimeter is divided into three regions: the barrel ($|\eta| < 1.475$) and two end-caps

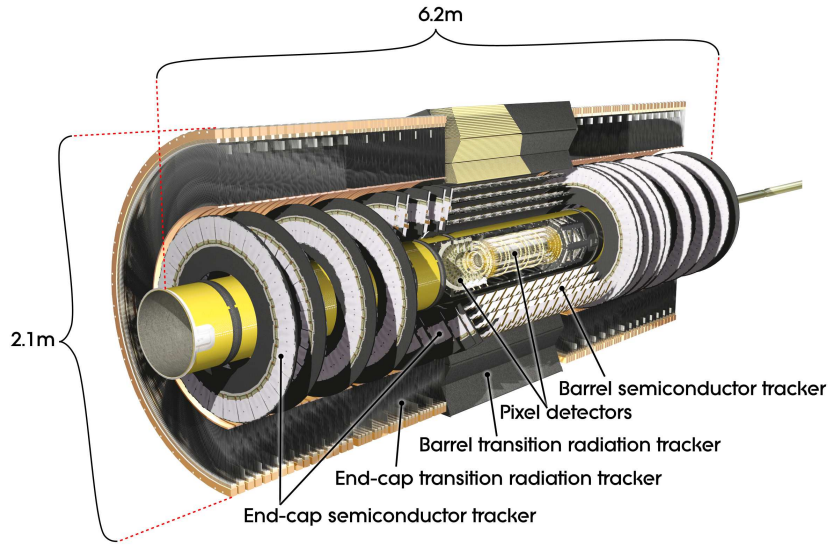


Figure 3.7: *Cut-away view of the ATLAS Inner Detector (extracted from Ref. [68]).*

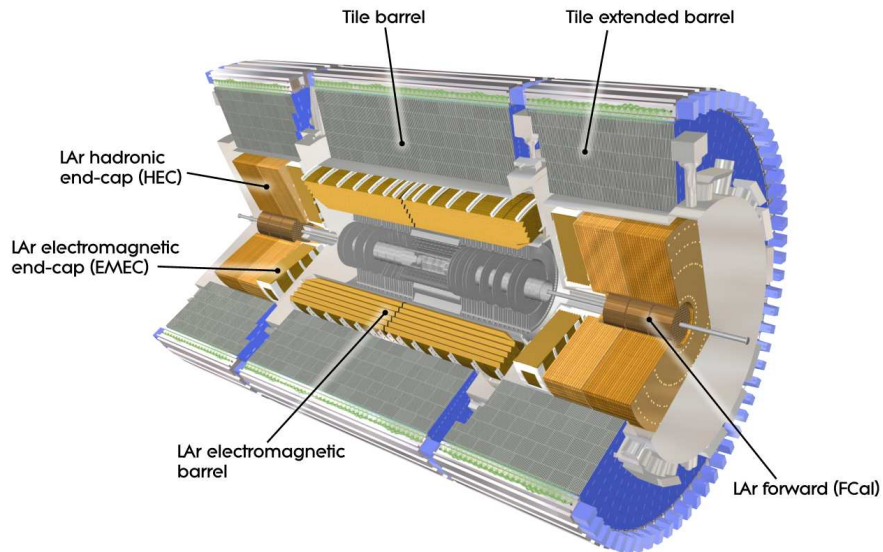


Figure 3.8: *Cut-away view of the ATLAS calorimeter system (extracted from Ref. [68]).*

| Barrel | | | End-cap | |
|---|----------------------|-------------------------|----------------------|--------------------------|
| EM calorimeter | | | | |
| number of layers and $ \eta $ coverage: | | | | |
| presampler | 1 | $ \eta < 1.52$ | 1 | $1.5 < \eta < 1.8$ |
| calorimeter | 3 | $ \eta < 1.35$ | 2 | $1.375 < \eta < 1.5$ |
| | 2 | $1.35 < \eta < 1.475$ | 3 | $1.5 < \eta < 2.5$ |
| | | | 2 | $2.5 < \eta < 3.2$ |
| granularity ($\Delta\eta \times \Delta\phi$ versus $ \eta $): | | | | |
| presampler | 0.025×0.1 | $ \eta < 1.52$ | 0.025×0.1 | $1.5 < \eta < 1.8$ |
| calorimeter 1st layer | $0.025/8 \times 0.1$ | $ \eta < 1.4$ | 0.050×0.1 | $1.375 < \eta < 1.425$ |
| | 0.025×0.025 | $1.4 < \eta < 1.475$ | 0.025×0.1 | $1.425 < \eta < 1.5$ |
| | | | $0.025/8 \times 0.1$ | $1.5 < \eta < 1.8$ |
| | | | $0.025/6 \times 0.1$ | $1.8 < \eta < 2.0$ |
| | | | $0.025/4 \times 0.1$ | $2.0 < \eta < 2.4$ |
| | | | 0.025×0.1 | $2.4 < \eta < 2.5$ |
| | | | 0.1×0.1 | $2.5 < \eta < 3.2$ |
| calorimeter 2nd layer | 0.025×0.025 | $ \eta < 1.4$ | 0.050×0.025 | $1.375 < \eta < 1.425$ |
| | 0.075×0.025 | $1.4 < \eta < 1.475$ | 0.025×0.025 | $1.425 < \eta < 2.5$ |
| | | | 0.1×0.1 | $2.5 < \eta < 3.2$ |
| calorimeter 3rd layer | 0.050×0.025 | $ \eta < 1.35$ | 0.050×0.025 | $1.5 < \eta < 2.5$ |
| Number of read-out channels | | | | |
| presampler | 7808 | | 1536 (both sides) | |
| calorimeter | 101760 | | 62208 (both sides) | |
| scintillator tile calorimeter (TileCal) | | | | |
| $ \eta $ coverage | $ \eta < 1.0$ | | $0.8 < \eta < 1.7$ | |
| number of layers | 3 | | 3 | |
| granularity ($\Delta\eta \times \Delta\phi$) | 0.1×0.1 | | 0.1×0.1 | |
| | 0.2×0.1 | | 2.2×0.1 | |
| read-out channels | 5760 | | 4092 (both sides) | |
| LAr hadronic endcap (HEC) | | | | |
| $ \eta $ coverage | | | $1.5 < \eta < 3.2$ | |
| number of layers | | | 4 | |
| granularity ($\Delta\eta \times \Delta\phi$) | | | 0.1×0.1 | $1.5 < \eta < 2.5$ |
| | | | 0.2×0.2 | $2.5 < \eta < 3.2$ |
| read-out channels | | | 5632 (both sides) | |
| LAr forward calorimeter (FCal) | | | | |
| $ \eta $ coverage | | | $3.1 < \eta < 4.9$ | |
| number of layers | | | 3 | |
| granularity ($\Delta x \times \Delta y$, in cm^2) | | | FCal 1 | 3.0×2.6 |
| | | | FCal 2 | 2.3×4.2 |
| | | | FCal 3 | 5.4×4.7 |
| read-out channels | | | 3524 (both sides) | |

Table 3.4: Summary of the pseudorapidity coverage, granularity and segmentation in layers for each calorimeter (adapted from [68]).

($1.375 < |\eta| < 3.2$). The amount of material in front of the EM calorimeter is an important factor, which affects its performance. In particular, a significant amount of material is present at $|\eta| \sim 1.5$, corresponding to the cables and service structures passing to the ID.

The hadronic calorimeter is composed by three subdetectors: the tile calorimeter (TileCal), the LAr hadronic end-cap calorimeter (HEC) and the LAr forward calorimeter (FCal). The TileCal [72, 73] is a sampling calorimeter using steel as the absorber and scintillator as the active medium. It is located in the region, $|\eta| < 1.7$, behind the LAr EM calorimeter, and it is subdivided into a barrel central region ($|\eta| < 1.0$) and two extended barrels ($0.8 < |\eta| < 1.7$). The radial depth of the TileCal is ~ 7.4 interaction lengths at normal incidence. The electronic and read-out of TileCal are integrated in its mechanical structure. The light produced in the scintillating tiles is collected at the edges of each tile using two wavelength shifting fibers. The HEC is a copper-LAr sampling calorimeter which covers the range $1.5 < |\eta| < 3.2$. It shares each of the two LAr end-cap cryostats with EMEC and FCals. The FCals provide coverage over $3.1 < |\eta| < 4.9$ and are divided in three modules: the first one has copper as passive material and the other two have tungsten (the active material is LAr in the three modules).

The required resolutions for the ATLAS calorimeters are:

$$\begin{aligned}\frac{\sigma_E}{E} &= \frac{10\%}{\sqrt{E}} \oplus 0.7\% & (\text{EM}), \\ \frac{\sigma_E}{E} &= \frac{50\%}{\sqrt{E}} \oplus 3\% & (\text{hadronic, barrel and end-caps}), \\ \frac{\sigma_E}{E} &= \frac{100\%}{\sqrt{E}} \oplus 10\% & (\text{hadronic, forward}).\end{aligned}$$

3.2.5 Muon system

The muon spectrometers are the ATLAS most external detectors. The muon system can be divided into the barrel, where the muon chambers are arranged cylindrically, and the end-cap regions, where they are placed vertically (*c.f.* figure 3.9).

The muon system has a full coverage in the region $|\eta| < 2.7$, with the exception of a region around $\eta = 0$, where a 300 mm gap is present, allowing for the passage of the services for the ID detector, solenoid and calorimeters. This gap leads to a significant degradation of the muon reconstruction efficiency in that region.

In most of the η range, the measurement of the track coordinates is provided by the Monitored Drift Tubes (MDT), which are aluminium-walled gaseous drift chambers in which the muons ionize the gas under a high electric field. At large pseudorapidities ($2.0 < |\eta| < 2.7$), Cathode Strip Chambers (CSC) with higher granularity are used. The CSC are multiwire proportional chambers with cathodes segmented into strips. The muon trigger system covers the pseudorapidity range $|\eta| < 2.4$, using Resistive Plate Chambers (RPC) in the barrel ($|\eta| < 1.05$) and Thin Gap Chambers (TGC) in the end-caps ($1.05 < |\eta| < 2.7$). Relevant parameters of the muon system

are summarized in table 3.5.

The required resolution for the muon system is:

$$\frac{\sigma_{p_T}}{p_T} = 10\% \text{ (at } p_T = 1 \text{ TeV).}$$

3.2.6 Forward detectors

Two smaller detectors cover the ATLAS forward region, with the main purpose of measuring the luminosity delivered to ATLAS. At ± 17 m from the interaction point lies LUCID⁴. It detects inelastic pp scattering in the forward direction, being the main on-line relative-luminosity monitor for ATLAS. The second set of detectors is ALFA⁵, which is located at ± 240 m of the interaction point and is made of scintillating fibre trackers located inside roman pots, designed to approach as close as 1 mm to the beam. The ALFA detectors will allow the measurement of the elastic Coulomb scattering cross-section.

During the initial period of the LHC operation, the absolute calibration procedure for LUCID will rely on the knowledge of the LHC parameters. This will allow the luminosity evaluation with an initial precision of $\sim 20 - 30\%$. In a posterior phase, a more accurate calibration will be obtained with the ALFA detectors, which should allow the measurement of the luminosity with an uncertainty below 5%.

3.2.7 Trigger and data acquisition systems

With an LHC bunch crossing every 25 ns (*i.e.* at a 40 MHz rate) and ~ 20 collisions per bunch crossing at nominal luminosity, events will be produced at ATLAS with a rate of ~ 1 GHz (much larger than the 200 Hz storage capability of the ATLAS experiment [74, 68]). Therefore, the trigger system has to be able to reduce the incoming interaction rate by a factor of $\sim 10^7$ in such a way that the interesting hard-scattered events are selected with high efficiency.

The trigger and data acquisition (DAQ) systems are divided in three levels of event selection, based on the signatures of high- p_T particles and missing transverse energy. These three levels are schematically represented in figure 3.10.

The first level of trigger (LVL1) takes a decision based on the reduced-granularity information from a subset of fast detectors (RPC and TGC muon spectrometers for muons and the calorimeters for EM clusters, jets, τ -leptons decaying into hadrons, E_T and large total energy). The LVL1 trigger takes a decision within $2.5 \mu\text{s}$ and, meanwhile, the full event data is kept in the pipeline memory. The data corresponding to the events selected by the LVL1 are transferred to the read-out buffers (ROB)

⁴ LUCID is an acronym for **L**uminosity measurement using **C**herenkov **I**ntegrating **D**etector.

⁵ ALFA is an acronym for **A**bsolute **L**uminosity **F**or **A**TLAS.

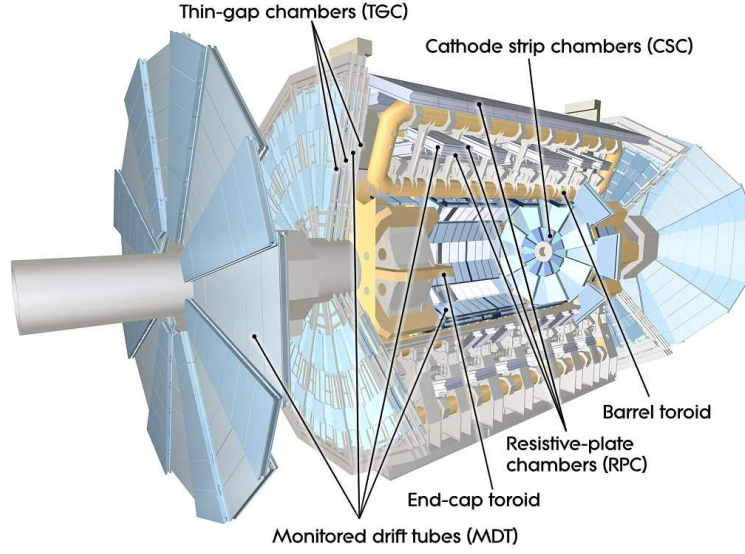


Figure 3.9: Cut-away view of the ATLAS muon system (extracted from Ref. [68]).

| monitored drift tubes (MDT) | |
|---------------------------------------|---|
| coverage | $ \eta < 2.7$ (innermost layer: $ \eta < 2.0$) |
| number of chambers | 1150 |
| number of channels | 354000 |
| function | precision tracking |
| cathode strip chambers (CSC) | |
| coverage | $2.0 < \eta < 2.7$ |
| number of chambers | 32 |
| number of channels | 31000 |
| function | precision tracking |
| resistive plate chambers (RPC) | |
| coverage | $ \eta < 1.05$ |
| number of chambers | 606 |
| number of channels | 373000 |
| function | triggering, second coordinate |
| thin gap chambers (TGC) | |
| coverage | $1.05 < \eta < 2.7$ (for triggering: $ \eta < 2.4$) |
| number of chambers | 3588 |
| number of channels | 318000 |
| function | triggering, second coordinate |

Table 3.5: Relevant parameters of the ATLAS muon spectrometer for the final configuration of the detector in 2009 (adapted from Ref. [68]).

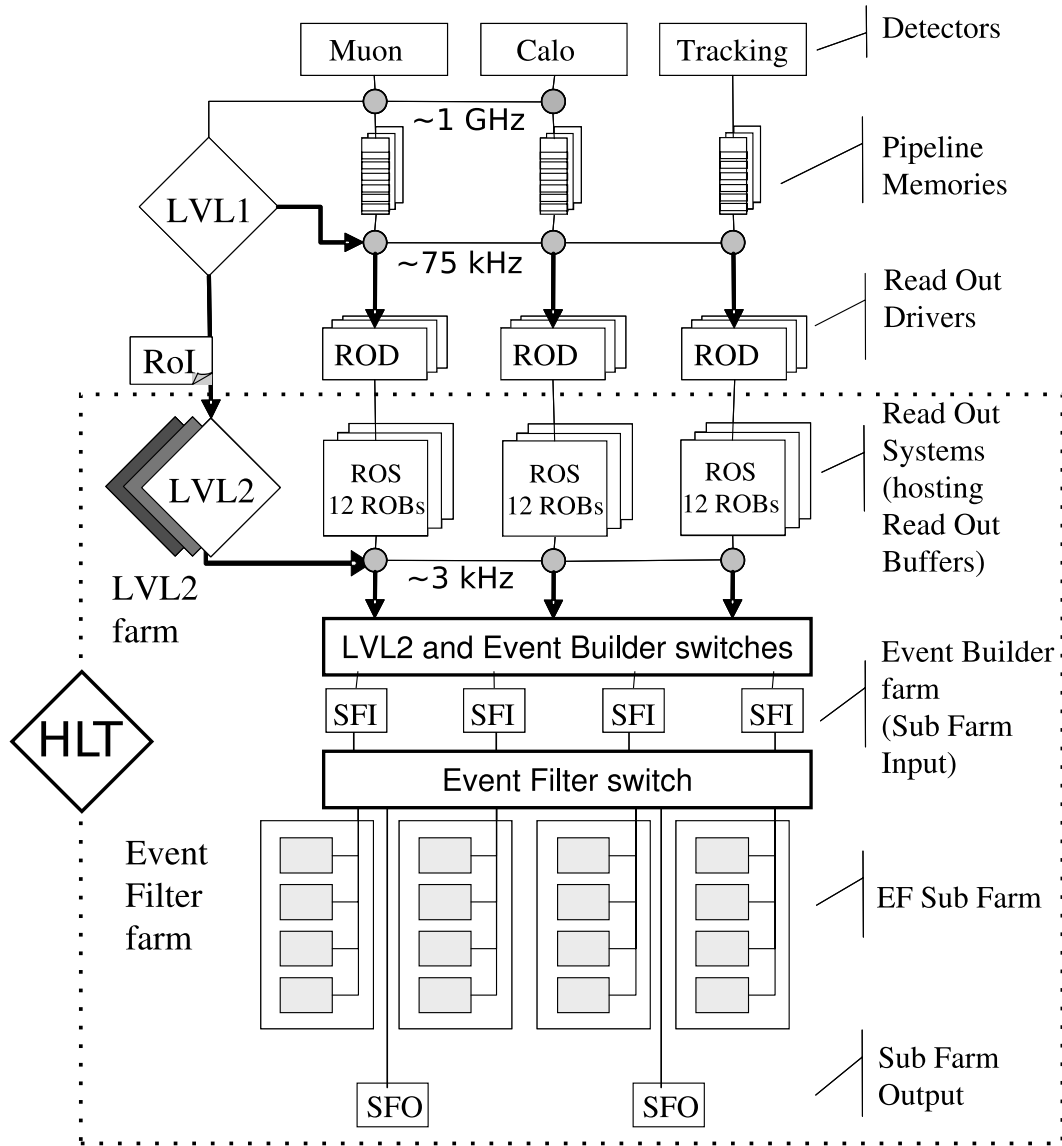


Figure 3.10: *ATLAS trigger and data acquisition systems (adapted from Ref. [74])*

by the read-out drivers (ROD). The trigger rate after LVL1 is ~ 75 kHz (upgradable to 100 kHz).

The High Level trigger (HLT) is divided into two levels: the second level trigger (LVL2) and the event filter (EF). While the LVL1 was implemented with custom-made electronics, the HLT is almost entirely based on commercial computers and networking hardware.

The LVL2 is seeded by regions-of-interest (RoI), which are the regions of the detector where LVL1 has identified possibly interesting objects. The LVL2 uses RoI information on coordinates, energy and topologies, to limit the amount of data to be read-out from the detector. In this way, although the HLT algorithms require the full granularity and precision of the calorimeters and muon chambers, only $\sim 2\%$ of

the full event data is needed for a decision. LVL2 has a latency of the order of 1 s, achieving an event rate around 3 kHz.

The EF uses off-line procedures to fully reconstruct events, performing a last selection of the events to be recorded for subsequent off-line analysis. This trigger level reduces the event rate to approximately 200 Hz, with an average event processing time of ~ 4 s.

Trigger conditions are referred to by a combination of letters and numbers. The object being triggered is represented by one or two letters (EM for electromagnetic clusters, e for electrons and MU or mu for muons), with capital and lower-case letters being used for LVL1 and HLT, respectively. Following these letters, the numbers represent the p_T of the object for which the trigger is 95% efficient. If an isolation requirement exists the letter i or I is added. As an example, EM25I represents the LVL1 trigger condition requiring an isolated EM cluster and this trigger condition has an efficiency of 95% for EM clusters above 25 GeV.

3.2.8 LHC computing Grid

Even at the LHC start-up, the ATLAS experiment will collect and store over 1 PB of data per year [75]. The storage and offline reconstruction of this amount of data require the use of a large storage and computing resources. In order to optimize and share such resources, a worldwide Grid computing system was developed for the LHC experiments [75, 76, 77].

The Grid sites are organized in Tiers: the Tier-0 is located at CERN (where the data are produced) and it is connected via high-speed networks to eleven Tier-1 sites (located in different countries), which will store the output of event reconstruction. The Tier-1 centres will make data available to Tier-2 centres, each consisting of collaborating computing facilities, which can store sufficient data and provide adequate computing power for specific analysis tasks. The individual scientists will access these facilities through Tier-3 computing resources, which consist of local computing clusters (or even individual computers).

3.2.9 Detector Control System

The Detector Control System (DCS) was designed to allow a coherent and safe operation of the detector hardware. It controls, monitors and archives the operational parameters, signals and any abnormal behaviour of the ATLAS detector. Typical examples of the monitored information are high and low voltage for detector and electronics, gas and cooling, magnetic field, temperatures and humidity. It also handles the communication between the sub-detectors and other systems, which are controlled independently (e.g. the LHC accelerator, the CERN technical services, the ATLAS magnets, and the detector safety system).

Chapter 4

MONTE CARLO GENERATION, SIMULATION AND RECONSTRUCTION

THE KNOWLEDGE of the physical properties of both the particular process under study (the signal) and the remaining SM processes (the background) requires the use of large samples of simulated events, which are described in section 4.1. For this, generators based on Monte Carlo (MC) techniques were used. Furthermore, the detector effects have to be considered using the simulation of the ATLAS detector. Such simulation can be performed using a fast simulation, which parametrizes the expected performance of the detector, or using the full GEANT4 [78] simulation, which simulates the detailed interaction of each particle in the detector (figure 4.1). The fast simulation (section 4.2) allows the simulation of very large samples of signal and background events. The full simulation (section 4.3), although much more demanding from the computational point of view, takes into account the detector details, allowing a more realistic study of the performances of particle reconstruction and trigger.

4.1 Signal and background processes

The LHC centre of mass energy ($\sqrt{s} = 14$ TeV) leads to a significant enhancement of the different production cross-sections with respect to those observed at the Tevatron ($\sqrt{s} \sim 2$ TeV), as represented in figure 4.2. The increase in the $t\bar{t}$ production is particularly important, and for this reason the LHC is expected to be a top quark production factory.

The $t\bar{t} \rightarrow W^+bW^-\bar{b}$ events, in which one of the W bosons decays hadronically and the other one decays in the leptonic channel $W \rightarrow \ell\nu_\ell$ (with $\ell = e^\pm, \mu^\pm$), are considered as signal events for the present analysis. The remaining decay channels

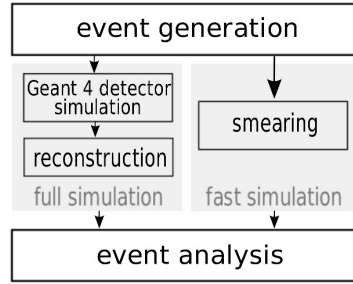


Figure 4.1: *Fast and full simulation of the ATLAS detector.*

of the $t\bar{t}$ pairs constitute a background to this signal (*c.f.* with figure 4.3). From now on, the W boson decaying hadronically and its parent top quark will be named as “hadronic” and the W decaying leptonically (and its parent top quark) will be called “leptonic”. Similarly, the b -quark associated with the leptonic W to reconstruct the leptonic top is called “leptonic b ” (and the one associated with the hadronic W to reconstruct the hadronic top is called “hadronic b ”). The $t\bar{t}$ topology where one of the W decays hadronically and the other one decays leptonically is called “semileptonic”, while the $t\bar{t}$ topologies in which both W -bosons decay into quarks or leptons are called “hadronic” and “dileptonic”, respectively. Other SM processes which can somehow mimic the semileptonic $t\bar{t}$ topology (*e.g.* single top, W +jets, Z +jets, WW , ZZ , WZ and QCD) are also considered as backgrounds.

4.1.1 Parton Distribution Functions

The protons in pp collisions, can be treated as a set of partons [80] (the quarks and the gluons), with its composition being described by structure functions. In the context of this parton model, the calculation of production cross-sections at hadron colliders depends on the knowledge of the Parton Distribution Functions (PDF), which describe the distribution of the momentum fraction (x) of the partons in a proton (as a function of the squared momentum transfer, Q^2 , carried by the exchanged particle in the scattering). The PDF cannot be calculated perturbatively and, therefore, are evaluated through the measurement of deep-inelastic scattering and jet production at colliders [81], and extrapolated with the DGLAP¹ evolution equations [82, 83, 84]. In particular, the ZEUS and H1 experiments at HERA have performed fits to the HERA data to extract parton densities at low x , where the gluon population clearly dominates [85, 86]. In figure 4.4 the PDFs evaluated by the CTEQ Collaboration [87] are shown. These PDF sets include data from experiments at HERA and Tevatron colliders.

¹DGLAP stands for Dokshitzer-Gribov-Lipatov-Altarelli-Parisi.

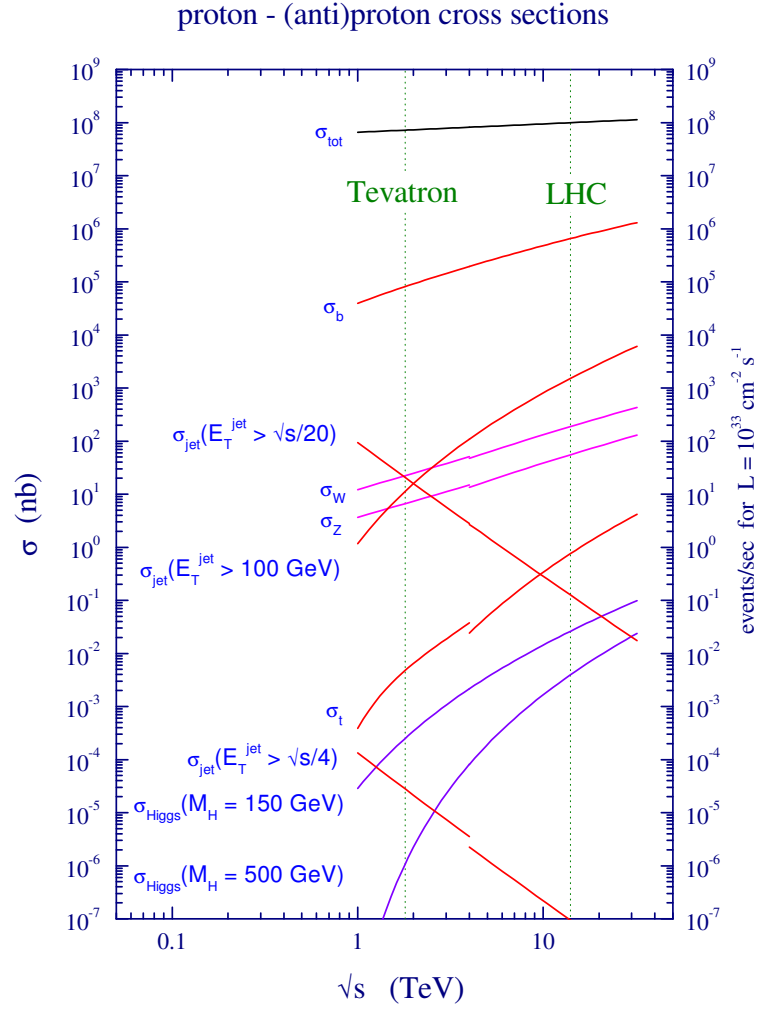


Figure 4.2: *Standard Model cross-sections at the Tevatron and the LHC [79]. The non-continuity of the cross-section values in the plot is due to the transition from a $p\bar{p}$ to a pp collider.*

| | | | | | |
|------------|---------------|-----------|------------|---------------|------------|
| $c\bar{s}$ | electron+jets | muon+jets | tau+jets | all-hadronic | |
| $\bar{u}d$ | | | | | |
| τ^- | e τ | $\mu\tau$ | $\tau\tau$ | tau+jets | |
| μ^- | e μ | $\mu\mu$ | $\mu\tau$ | muon+jets | |
| e^- | e e | e μ | e τ | electron+jets | |
| W decay | e^+ | μ^+ | τ^+ | $u\bar{d}$ | $c\bar{s}$ |

Figure 4.3: Final states for $t\bar{t} \rightarrow W^+ b W^- \bar{b}$ events, originated from the different W decays. In the present analysis the electron+jets and muon+jets channels are considered signal, while all the remaining final states constitute a background to this signal.

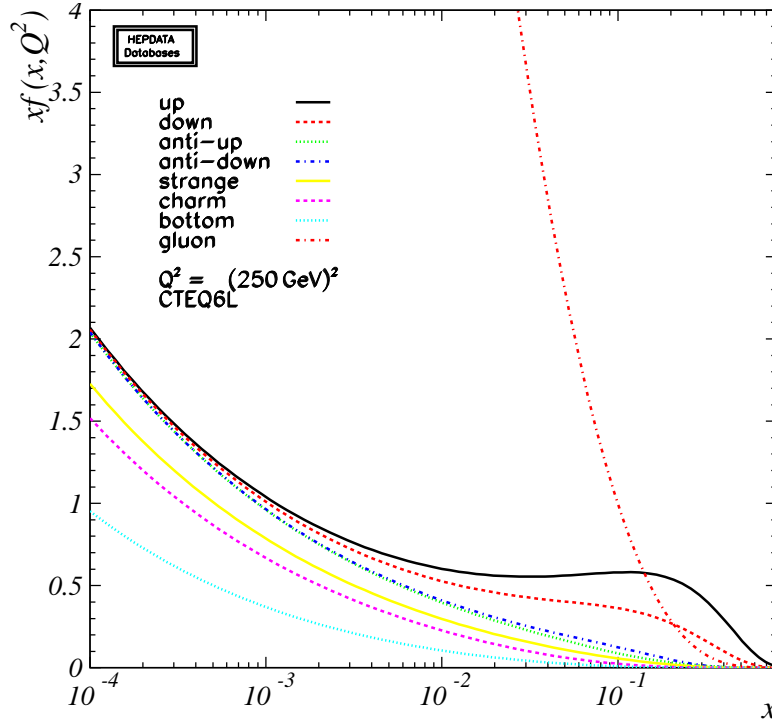


Figure 4.4: Parton Distribution Functions for $Q^2 = (250 \text{ GeV})^2$, evaluated by the CTEQ Collaboration (CTEQ 6L).

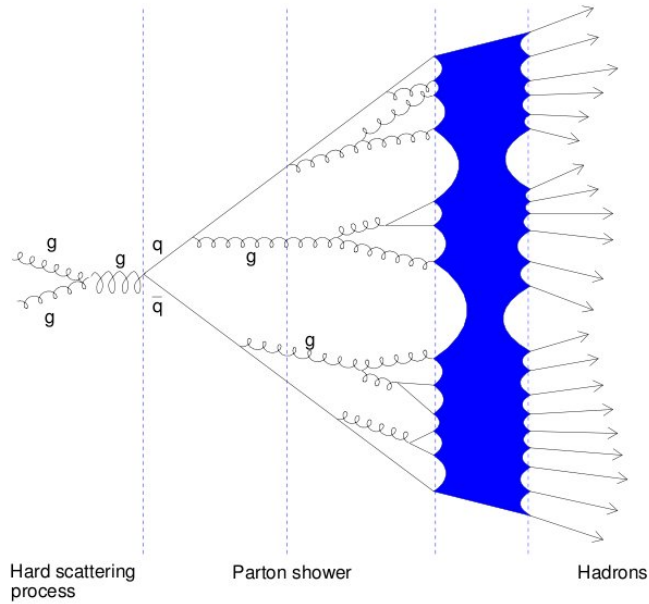


Figure 4.5: *Schematic representation of the quarks and gluon hadronization into colour-neutral hadrons. Figure extracted from Ref. [88].*

4.1.2 Hadronization

Due to confinement, quarks and gluons cannot manifest themselves as free particles but, instead, form colour-neutral hadrons. This implies that quarks and gluons produced in the hard process of the interaction are detected as jets of hadrons. Such process is called hadronization and it is represented schematically in figure 4.5.

An explicit calculation of the hadronization mechanism has not yet been performed, since it is a non-perturbative process [89]. Therefore, the simulation of the hadronization is performed with Monte Carlo methods, based on phenomenological models [90]. The Pythia [91] and HERWIG [92] Monte Carlo generators have different hadronization models implemented [93, 94, 95].

4.2 Fast simulation

A fast simulation of the ATLAS detector is an important tool to obtain the large samples of signal and background events needed for the analysis and for the study of systematic uncertainties. The fast simulation is based on the smearing of the tetra-momenta of the generated particles and on corrections for the particles identification efficiency. Therefore, it is relatively light from the computational point of view. As an example, the generation and fast simulation of 10^6 $t\bar{t}$ events (including all the possible decay channels) using the TopReX 4.10 generator [96] and

| process | generator | σ (pb) | | N_{events} ($\times 10^6$) | L (fb $^{-1}$) |
|-----------------------------|-----------|--------------------|-------|--|-----------------------|
| $t\bar{t}$ | TopReX | 833 | (NLO) | 39 | 46.8 |
| $t\bar{t}$ | AlpGen | 833 | (NLO) | 18 | 21.6 |
| single top (t -channel) | TopReX | 268 | (LO) | 3 | 11.2 |
| single top (Wt -channel) | TopReX | 51.3 | (LO) | 0.5 | 9.75 |
| single top (s -channel) | TopReX | 6.86 | (LO) | 0.5 | 72.9 |
| $b\bar{b}$ | PYTHIA | 1.57×10^8 | (LO) | 375 | 2.39×10^{-3} |
| W +jets | PYTHIA | 1.48×10^5 | (LO) | 35 | 0.24 |
| Z/γ^* +jets | PYTHIA | 6.09×10^4 | (LO) | 60 | 0.99 |
| WW , ZZ and WZ | PYTHIA | 7.46×10^2 | (LO) | 15 | 20.1 |

Table 4.1: *The MC generator, cross-section, number of generated events and corresponding luminosity for the generated samples. The NLO (including NLL soft gluon resummation) value for the $t\bar{t}$ cross-section [35] was used, while the LO cross-sections were considered for the remaining processes. The fast simulation of the ATLAS detector (ATLFAST) was used for these samples.*

the ATLFAST 2.53 package [97] took 17.5 hours in a 2.8 GHz Pentium IV computer with 512 MB of RAM. The resulting ntuples require 605 MB of disk space. In the present thesis, the fast simulation was used to estimate the ATLAS sensitivity to Wtb anomalous couplings with a luminosity of 10 fb^{-1} (which is expected to correspond to one year of LHC data in the low luminosity phase).

4.2.1 Monte Carlo generation

Top quark pairs, as well as the single top quark events, were generated with TopReX 4.10 [96] with default settings. In order to study the effect of the generator in the signal samples, an additional $t\bar{t}$ sample was generated using AlpGen 1.33 [98]. Further backgrounds without top quarks in the final state, *i.e.* $b\bar{b}$, W +jets, Z/γ^* +jets, WW , ZZ and WZ production processes, were generated using PYTHIA 6.206 [91]. In all cases the CTEQ 5L [99] parton distribution functions were used. For the systematic uncertainties studies, additional $t\bar{t}$ samples were generated with the CTEQ 6L [87] and MRST 2001 [100] PDF sets. Events were hadronized using PYTHIA, taking also into account initial state radiation (ISR), final state radiation (FSR) and pile-up. In order to evaluate the effect of ISR and FSR, $t\bar{t}$ samples without ISR and FSR were also generated.

In order to study the systematic uncertainties, $t\bar{t}$ samples were generated with TopReX 4.10 for different top masses ($m_t = 170, 175, 180 \text{ GeV}$). Furthermore, the parameter ϵ_b in the Peterson parameterisation for b -quark fragmentation was varied from the reference value (-0.006) to -0.0035 [91, 101]. Additional $t\bar{t}$ samples with pile-up [91] (with an average of 2.3 interactions per event) were also generated.

The generated Monte Carlo samples are listed in table 4.1. In figure 4.6 some relevant kinematical distributions at the generator level are shown for the $t\bar{t}$ signal (TopReX reference sample with CTEQ 5L, ISR and FSR, $m_t = 175$ GeV and without pile-up). For all the generated samples, the lower allowed p_T (defined in the rest frame of the hard interaction) for the $2 \rightarrow 2$ hard process was set to 5 GeV (flag CKIN(3) in PYTHIA).

It should be stressed that the objective of the present work is to test the sensitivity for the exclusion of new physics, under the hypothesis that the SM holds, and therefore the simulation was done assuming the absence of anomalous couplings. Once data becomes available, if an evidence for Wtb anomalous couplings is found, the generation of additional signal samples beyond the SM will be required.

4.2.2 Event simulation and reconstruction

The generated background and signal events were passed through the ATLAS fast simulation packages ATLFAST 2.53 and ATLFASTB [97].

In a first step, ATLFAST simulates for each event the energy deposition in the calorimeter cells by all the stable particles². The calorimeter cells were then clustered within a cone of $\Delta R = 0.4$. Cells with transverse energy (E_T) above 1.5 GeV were used as cluster seeds and the cone algorithm was applied in decreasing order of E_T . Only clusters with $E_T > 5$ GeV are considered.

The polar angle of the generated photons was smeared, assuming a Gaussian parameterisation with the following resolution:

$$\left\{ \begin{array}{ll} \frac{0.065}{\sqrt{E_\gamma}}, & |\eta| < 0.8 \\ \frac{0.050}{\sqrt{E_\gamma}}, & 0.8 < |\eta| < 1.4 \\ \frac{0.40}{\sqrt{E_\gamma}}, & 1.4 < |\eta| < 2.5 \end{array} \right. \quad (4.1)$$

Furthermore, the momentum and energy of the generated electrons and muons was smeared according to Gaussian parameterisations, depending on p_T and $|\eta|$. Consequently, after ATLFAST, the photon (electron) energy resolution is $\sigma E/E < 2.9\%$ (3.3%), for $E > 20$ GeV. The transverse momentum resolution of muons with $p_T < 100$ GeV is $\sigma p_T/p_T \lesssim 2\%$. Photons, electrons and muons were selected only if they have $|\eta| < 2.5$ and $p_T > 5$ GeV ($p_T > 6$ GeV for muons). They were classified as isolated if the transverse energy of the cluster associated to the particle, inside a cone of $\Delta R = 0.2$, did not exceed the particle energy by 10 GeV, and if ΔR to any other energy cluster was above 0.4.

The clusters of energy depositions not associated to isolated photons, electrons or muons are used for the jet reconstruction. Their momenta was smeared according to a Gaussian distribution, depending on $|\eta|$. Jets were selected if they have $E_T >$

² The $\Delta\eta \times \Delta\phi$ dimensions of the cells are 0.1×0.1 (0.2×0.2) for $|\eta| < 3$ ($3 < |\eta| < 5$).

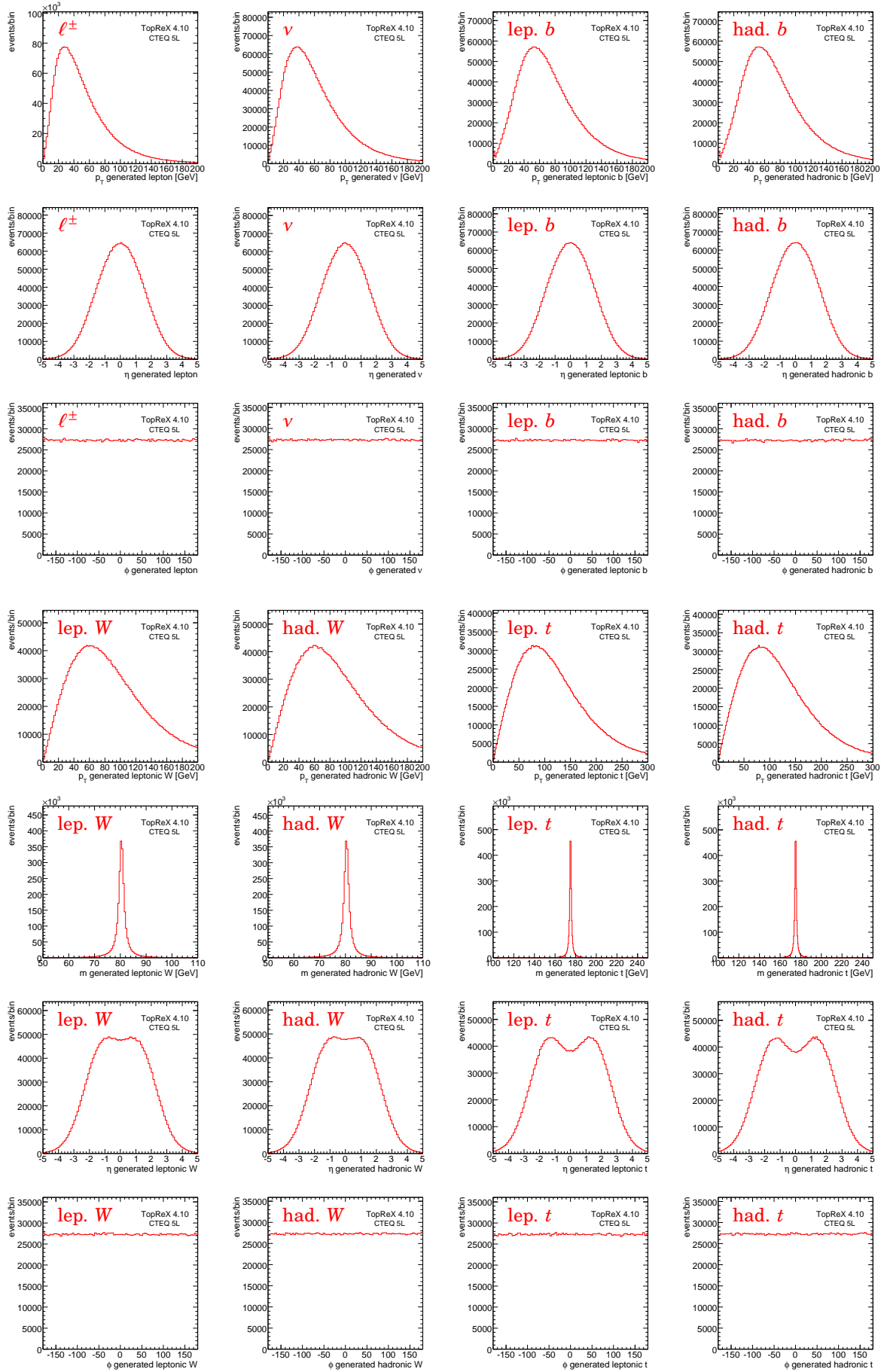


Figure 4.6: *Distributions, at the generator level (TopReX 4.10 with CTEQ 5L PDF set), of the transverse momentum, mass, η and ϕ of the hard process particles.*

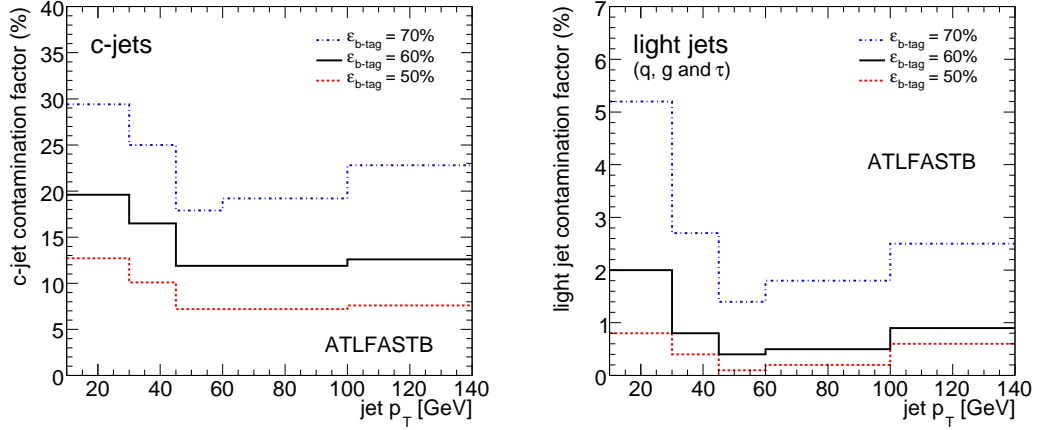


Figure 4.7: Values defined in ATLFASTB for c and light jets contamination factors, as a function of the jet transverse momentum, for different values of b -tagging efficiencies.

10 GeV. For $E > 20$ GeV, the jet energy resolution is better than 12% for $|\eta| < 3$ and better than 24% for $|\eta| > 3$.

The missing transverse momentum was estimated by summing the transverse momentum of the isolated photons, electrons, muons and jets. The non-isolated muons and the clusters of energy deposition not associated to isolated photons, electrons, muons or jets, were also taken into account.

In the ATLAS detector, it will be possible to identify b jets with $|\eta| < 2.5$ by using b -tagging tools [68]. This algorithm was simulated using the ATLFASTB package, which, by default, sets the b -tagging efficiency to 60%. In order to check the dependence of the analysis with the b -tagging efficiencies, different values, 50% and 70% (corresponding to the expected variation within the interesting signal transverse momentum range), were also considered for the systematic studies. The corresponding contamination factors for c and light jets (light quarks, gluons and tau leptons) depend on the jet transverse momentum and are represented in figure 4.7.

Due to the hadronization and FSR, the jets are reconstructed with lower energy than the original quarks or gluons. The jet energy is calibrated by the ATLFASTB package, by applying a calibration factor, $K^{\text{jet}} = p_T^{\text{parton}}/p_T^{\text{jet}}$, which is the ratio between the true parton energy and the reconstructed jet energy, obtained from reference Monte Carlo samples [97]. The calibration factor depends on p_T and it is different for b -tagged and for non b -tagged jets (*c.f.* figure 4.8).

4.3 Full simulation

The full simulation allows to study in detail the detector performance, namely the reconstruction efficiencies for the different detected particles and the trigger im-

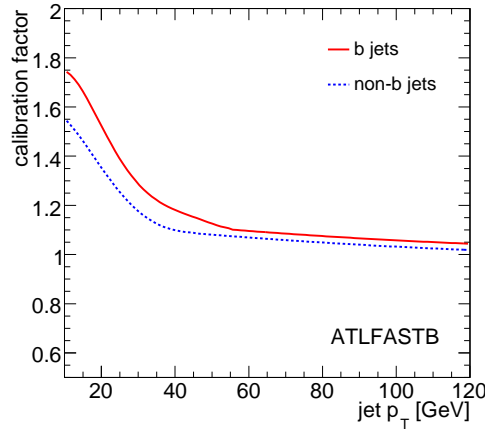


Figure 4.8: Calibration factors applied to jets by the ATLFASTB package, defined as the ratio between the true parton energy and the reconstructed jet energy, obtained from reference Monte Carlo samples. These factors depend on the jet p_T and are different for b -tagged and non b -tagged jets.

impact on the analyses. The drawback of the full simulation is the required computing time, which significantly reduces the number of simulated events possible to obtain in a reasonable amount of time. The computing time required for the simulation of relevant SM processes is shown in figure 4.9.

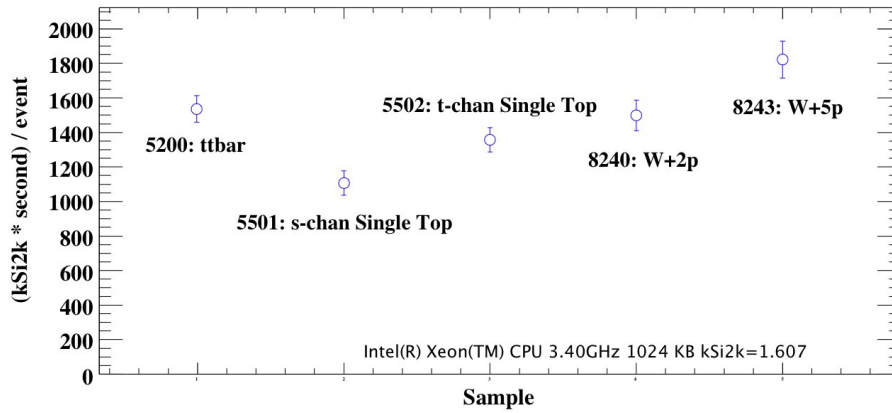


Figure 4.9: Time taken to simulate one event for different Monte Carlo samples (in units of $kSi2k$ seconds [102]). Figure extracted from Ref. [103].

The complete simulation of the ATLAS detector has to take into account a large number of physics processes occurring within the different parts of the detector [104, 105]. The GEANT4 simulation was validated through the comparison with test-beam data [106] and a good agreement (at the level of 1%) has been found [105]. With the first LHC data, a significant effort will be required to understand the details of the current ATLAS experiment configuration. This information will be included in the simulation.

After generating the Monte Carlo events³, the ATLAS simulation estimates the

³ The information at the generator level is recorded in the HepMC [107] format.

response of the detectors (GEANT4 hits) in order to produce the simulated digital output (GEANT4 digits). At this stage, Raw Data Objects (RDO) are obtained and are fed to the pattern recognition and tracking reconstruction algorithms, being processed in the same way as real data. The first output of event reconstruction is saved in the Event Summary Data (ESD), which due to the large event size (~ 2 MB per $t\bar{t}$ event), will only be available at Tier-1 Grid sites [76, 77, 75]. In order to reduce the event size, the ESD are then slimmed down into Analysis Object Data (AOD), which are expected to be small enough to be made available in the Tier-2 sites (~ 500 kB per $t\bar{t}$ event). The contents of AOD were designed to provide the necessary information for the main physics analysis. Detailed studies of the detector may need to access the ESD data. The chain from the generation to the reconstructed events is represented in figure 4.10.

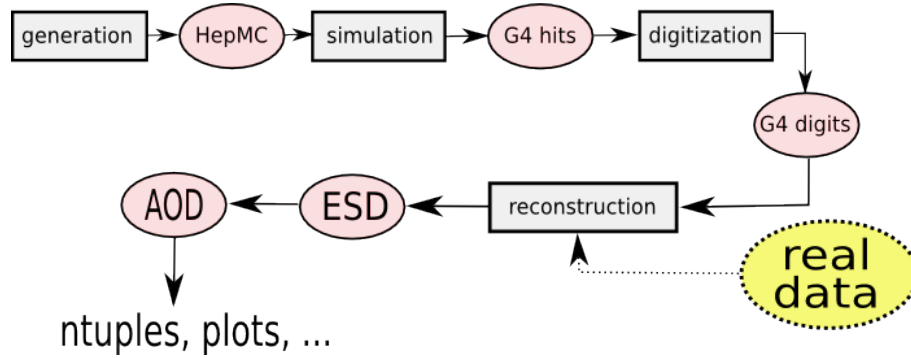


Figure 4.10: Schematic representation of the full simulation production chain.

The full simulation samples used in the present study are part of the ATLAS Computing System Commissioning (CSC) exercise [108] and were produced by the ATLAS collaboration using the Worldwide LHC Computing Grid (LCG). The gLite tools [109] were used to access and store locally these samples.

4.3.1 Monte Carlo generation

The generation of $t\bar{t}$ events was done using the generator MC@NLO 3.1 [110]. Within this generator the hard process of $t\bar{t}$ is calculated at NLO and therefore diagrams leading to an additional jet or gluon in the final state ($2 \rightarrow 3$ processes) are also included at the matrix element level [111]. The fragmentation and hadronization was done using HERWIG [92], in conjunction with the underlying event generator Jimmy [112, 113]. No kinematical cuts were applied at the generation. A fixed top mass of 175 GeV was assumed for the reference sample, while additional samples with $m_t = 160, 170, 190$ GeV were generated for systematic studies. In figure 4.11 some relevant kinematical distributions at the generator level are shown for the reference $t\bar{t}$ signal sample (*i.e.*, for the semileptonic $t\bar{t}$ events generated with MC@NLO 3.1, fixing the top mass to 175 GeV). Unlike TopReX (figure 4.6), the MC@NLO generator assumes a fixed top mass (with zero width) and do not consider spin correlations between the produced t and \bar{t} -quarks. For high values of the top quarks

p_T , the ratio between the NLO and LO cross-sections become larger [114]. In this region, MC@NLO is expected to describe better the generated top quarks than the LO generators.

Single top events were generated with AcerMC [115], with the hadronization being done by PYTHIA. For all the three channels (t-channel, s-channel and Wt channel), the W -bosons were forced to decay to leptons (e , μ or τ). In the case of Wt channel, one of the W -bosons present in the event (either the associated W or the W from the top decay) was forced to decay into leptons, while the other one was required to decay into quarks.

Background events coming from the $W + n$ jets ($n = 2, \dots, 5$) processes were generated with ALPGEN 2.06 [98] interfaced with HERWIG. A parton-jet matching algorithm was used to avoid the double counting of events caused by the overlap between the multi-parton matrix element and the parton shower [116]. In order to optimize the generation ⁴, only leptonic decays of the W were accepted and the events were forced to have at least three generated jets with $p_T > 30$ GeV. A fraction of this background contains heavy quarks. Such processes ($Wb\bar{b} + n$ jets and $Wc\bar{c} + n$ jets, with $n = 1, \dots, 3$) were generated separately. In these cases, the only requirement at the generation level was the leptonic decay of the W .

The Z +jets events were generated with PYTHIA [91]. In these events the Z -boson was forced to have an invariant mass above 20 GeV and had to decay into charged leptons (e , μ or τ). Furthermore, the electrons and muons were required to have a $p_T > 10$ GeV, while the taus were required to have $p_T > 5$ GeV and had to decay into electrons or muons.

Diboson (WW , ZZ and WZ) events were generated with HERWIG. For these events a filter requiring a generated electron or a muon with $p_T > 10$ GeV was applied.

The CTEQ 6M PDF set [87] was used for the MC@NLO events, while the generation of the remaining events was done with CTEQ 6L. For all generated events, the TAUOLA and PHOTOS [117] packages were used to process the τ -decay and radiative corrections, respectively. ISR, FSR and multiple interactions were taken into account. For systematic uncertainties studies $t\bar{t}$ events were also generated with AcerMC and hadronized with PYTHIA. The initial and final state radiation effects in $t\bar{t}$ events were studied with AcerMC interfaced with PYTHIA samples, by changing the generator parameters which controls the p_T cut-off and parton shower parameterisation associated to ISR and FSR. ⁵ No pile-up events were added with the exception of a small $t\bar{t}$ MC@NLO sample, where an average of 4.6 collisions per bunch

⁴ In order to limit the size of the full simulation samples, only the background events with final state events similar to the ones expected for the semileptonic $t\bar{t}$ signal were generated and fully simulated.

⁵ In order to obtain a sample leading to a maximum (minimum) value of m_t , the PYTHIA parameters which control the ISR cut-off scale and ISR/FSR parton shower parameterisation were changed to PARJ(81)=0.07, PARP(61)=0.384 and PARP(62)=1.0 (PARJ(81)=0.28, PARP(61)=0.096 and PARP(62)=3.0). The parameter PARJ(81) (PARP(61)) affects the FSR (ISR) parton shower by setting the QCD scale (Λ_{QCD}) used in the running α_s evaluation, while the PARP(62) parameter controls the ISR cut-off scale [91, 118].

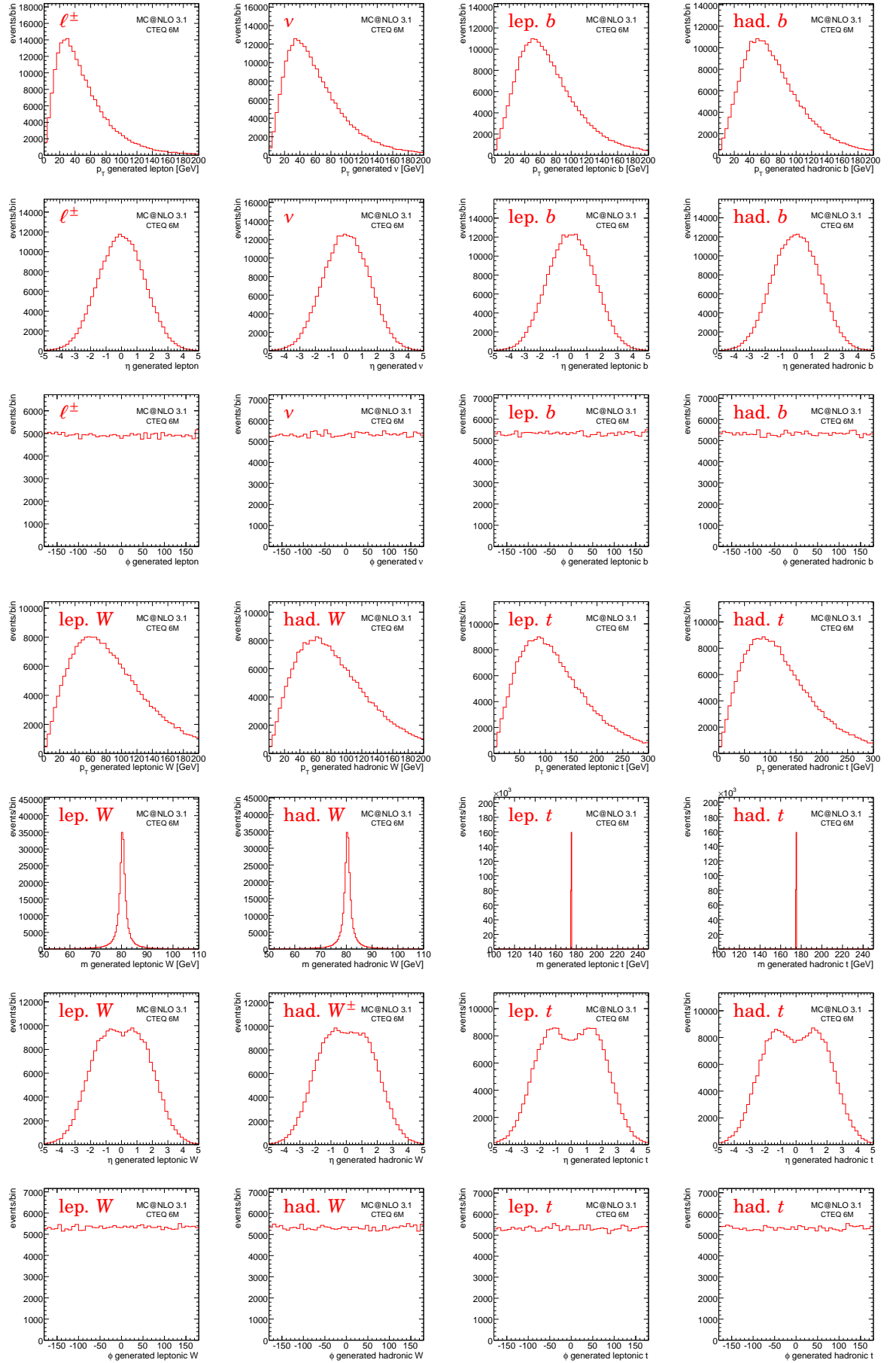


Figure 4.11: *Distributions, at the generator level (MC@NLO 3.1 with CTEQ 6M PDF set), of the transverse momentum, mass, η and ϕ of the hard process particles.*

| process | generator | σ (pb) | N_{events} | L (fb $^{-1}$) |
|---------------------------------------|-----------|---------------|---------------------|-------------------|
| $t\bar{t} \rightarrow \ell(\ell) + X$ | MC@NLO | 450 | 548550 | 0.89 |
| $t\bar{t} \rightarrow \text{hadrons}$ | MC@NLO | 383 | 97200 | 0.19 |
| single top (Wt channel) | AcerMC | 29.1 | 48350 | 1.66 |
| single top (s-channel) | AcerMC | 3.5 | 48300 | 14.0 |
| single top (t-channel) | AcerMC | 79.9 | 46950 | 0.52 |
| $W \rightarrow e\nu + 2$ jets | ALPGEN | 246 | 21950 | 0.09 |
| $W \rightarrow e\nu + 3$ jets | ALPGEN | 143 | 11250 | 0.08 |
| $W \rightarrow e\nu + 4$ jets | ALPGEN | 62 | 6000 | 0.10 |
| $W \rightarrow e\nu + 5$ jets | ALPGEN | 26 | 4950 | 0.19 |
| $W \rightarrow \mu\nu + 2$ jets | ALPGEN | 19 | 7000 | 0.37 |
| $W \rightarrow \mu\nu + 3$ jets | ALPGEN | 74 | 12500 | 0.17 |
| $W \rightarrow \mu\nu + 4$ jets | ALPGEN | 41 | 3200 | 0.08 |
| $W \rightarrow \mu\nu + 5$ jets | ALPGEN | 23 | 2750 | 0.12 |
| $W \rightarrow \tau\nu + 2$ jets | ALPGEN | 101 | 19700 | 0.20 |
| $W \rightarrow \tau\nu + 3$ jets | ALPGEN | 100 | 13000 | 0.13 |
| $W \rightarrow \tau\nu + 4$ jets | ALPGEN | 53 | 5750 | 0.11 |
| $W \rightarrow \tau\nu + 5$ jets | ALPGEN | 24 | 550 | 0.02 |
| $Wb\bar{b} + 0$ jets | ALPGEN | 16.1 | 6250 | 0.38 |
| $Wb\bar{b} + 1$ jet | ALPGEN | 17.9 | 7200 | 0.40 |
| $Wb\bar{b} + 2$ jets | ALPGEN | 10.1 | 4000 | 0.40 |
| $Wb\bar{b} + 3$ jets | ALPGEN | 7.1 | 3000 | 0.42 |
| $Wc\bar{c} + 0$ jets | ALPGEN | 17.3 | 7000 | 0.41 |
| $Wc\bar{c} + 1$ jet | ALPGEN | 19.3 | 3500 | 0.18 |
| $Wc\bar{c} + 2$ jets | ALPGEN | 11.2 | 4500 | 0.40 |
| $Wc\bar{c} + 3$ jets | ALPGEN | 6.3 | 2500 | 0.40 |
| $Z \rightarrow ee$ | PYTHIA | 1747 | 481300 | 0.28 |
| $Z \rightarrow \mu\mu$ | PYTHIA | 1826 | 185400 | 0.10 |
| $Z \rightarrow \tau\tau$ | PYTHIA | 94 | 176300 | 1.88 |
| WW | HERWIG | 38 | 16250 | 0.42 |
| ZZ | HERWIG | 3 | 29800 | 11.1 |
| WZ | HERWIG | 15 | 30000 | 2.03 |

Table 4.2: The MC generator, cross-section and luminosity is shown for each considered sample. The cross-section values include the appropriated branching ratios (see text for details) and parton jet matching efficiencies when needed. The cross-section for all the samples were normalized to the NLO theoretical calculations [108].

crossing was assumed.

The Monte Carlo samples considered as reference for the analysis are summarized in table 4.2. The additional Monte Carlo samples, used for the study of systematic uncertainties, are shown in table 4.3.

| process | generator | N_{events} |
|--|-----------|---------------------|
| $t\bar{t} \rightarrow \ell(\ell) + X$ | AcerMC | 113750 |
| $t\bar{t} \rightarrow \ell(\ell) + X$ with pile-up | MC@NLO | 82600 |
| single top (Wt channel) with pile-up | AcerMC | 20700 |
| single top (s channel) with pile-up | AcerMC | 19250 |
| single top (t channel) with pile-up | AcerMC | 10800 |
| $t\bar{t} \rightarrow \ell(\ell) + X$ ($m_t = 170$ GeV) | MC@NLO | 98966 |
| $t\bar{t} \rightarrow \ell(\ell) + X$ ($m_t = 160$ GeV) | MC@NLO | 99750 |
| $t\bar{t} \rightarrow \ell(\ell) + X$ ($m_t = 190$ GeV) | MC@NLO | 98600 |
| $t\bar{t} \rightarrow \ell(\ell) + X$ (ISR/FSR param. $\rightarrow \max m_t$) | AcerMC | 403555 |
| $t\bar{t} \rightarrow \ell(\ell) + X$ (ISR/FSR param. $\rightarrow \min m_t$) | AcerMC | 431200 |

Table 4.3: *The MC generator and number of available events is shown for each sample considered for systematic studies.*

4.3.2 Detector simulation, digitization and reconstruction

The signal and background events were passed through the complete GEANT4 simulation of the ATLAS detector, using version 12.0.31 of the ATLAS software ATHENA [119]. The ATLAS layout used in this paper is based on a perfect detector, with misaligned layout of LAr calorimeters and muon system, distorted materials in LAr and inner detector and magnetic field with initial displacement included. The signals of each sub-detector were digitized and the whole event was reconstructed with ATHENA (version 12.0.6), which includes the trigger simulation. The AOD output from the reconstruction was used as the base for the analysis.

Event reconstruction

Muons, electrons, photons and jets were reconstructed using TopView [120, 121], which is based on the EventView package [122].

Electrons were reconstructed by the calorimeters and inner tracker of ATLAS [68] in the range of pseudorapidity $|\eta| < 2.5$ and transverse momentum (p_T) above 15 GeV.

Muons were reconstructed by the muon spectrometer and the inner detector [68] for $|\eta| < 2.5$ and $p_T > 15$ GeV. Furthermore, muons were required to be isolated in what concerns calorimeter energy: the additional transverse energy in a cone with radius $\Delta R = 0.2$ around the muon was required to be less than 6 GeV.

Photons were reconstructed from calorimeters information [68] and were required to have $|\eta| < 2.4$ and $p_T > 15$ GeV.

Jets were reconstructed with the standard ATLAS cone algorithm [68], in which calorimeter towers with E_T above 1 GeV are considered as seeds. In an iterative procedure, towers within a cone with $\Delta R = 0.4$ were assigned to jets until a stable configuration was found. Reconstructed photons which overlap with reconstructed electrons within a cone of $\Delta R = 0.1$ and reconstructed jets which overlap within a cone of $\Delta R = 0.2$ with electrons or photons were not considered. The jet energy was corrected through calibration coefficients, extracted from the ratio between the jet raw energy and the energy of the corresponding generated parton.⁶

The flavour tagging of jets can provide a very useful information for the data analysis (both for the correct reconstruction of the signal topology and for background rejection). The tagging of b -jets relies on the high mass and relatively long lifetime of B -hadrons, which leads to tracks with large impact parameters with respect to the primary vertex, and to the possibility of reconstructing secondary vertices. In ATLAS, the b -tagging algorithm [68, 108, 124] evaluates a weight for each jet, based on the three dimensional impact parameter (defined as the minimum distance of the jet to the primary vertex) and on the output of the algorithm used to reconstruct the secondary vertex. The distribution of this b -tagging weight for the generated b , c and light jets is shown in figure 4.12.

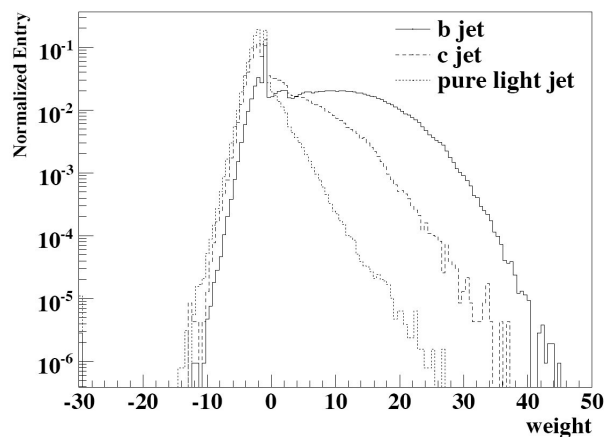


Figure 4.12: *Distribution of the b -tagging weight variable for b , c and light jets. An higher weight corresponds to an higher probability that the jet was originated by a b -quark. Figure extracted from Ref. [121].*

The missing transverse energy was evaluated as the sum of the following contributions: cells associated to reconstructed electron or photon clusters, cells inside jets, cells in topological clusters outside identified objects, muons and the cryostat correction [68].

⁶ This calibration based on Monte Carlo is intended to simulate the experimental determination of the jet energy scale (JES) with real data [123]. It is done by matching each reconstructed jet with the closest generated quark or gluon (within a cone with $\Delta R = 0.4$).

| reconstructed | generated | | | | |
|---------------|----------------|----------------|----------------|----------------|----------------|
| | e | μ | γ | τ | q/g |
| e | 76.7 ± 0.3 | <0.1 | 1.3 ± 0.3 | 18.4 ± 0.2 | 1.1 ± 0.1 |
| μ | <0.1 | 93.9 ± 0.3 | 0.1 ± 0.1 | 19.4 ± 0.2 | 0.1 ± 0.1 |
| γ | 5.4 ± 0.1 | <0.1 | 62.0 ± 2.3 | 1.1 ± 0.1 | 0.2 ± 0.1 |
| τ | 1.5 ± 0.1 | <0.1 | 1.6 ± 0.3 | 5.8 ± 0.1 | 0.4 ± 0.1 |
| jet | 15.9 ± 0.1 | 0.6 ± 0.1 | 34.6 ± 1.6 | 21.2 ± 0.2 | 93.0 ± 0.1 |

Table 4.4: Mean reconstruction efficiencies (in %) for each type of generated particles. Only particles with a generated p_T above 25 GeV and $|\eta| < 2.5$ were considered.

The reconstruction efficiency of muons, electrons and jets as a function of the η and p_T of the generated particles are shown in figure 4.13. These values take into account the pseudorapidity distributions of the mentioned types of particles, including the crack effects. Following a sharp raise, a stable behaviour of the efficiency, as a function of the particles transverse momentum, is visible. Away from the edges of the acceptance the efficiency is relatively flat with η . After an increase at low p_T , the efficiency is flat, including the high p_T region of the distributions, where statistics is low. The mean efficiencies for each generated electron, muon, photon, tau and quark/gluon (with $p_T > 25$ GeV and $|\eta| < 2.5$) to be reconstructed as electron, muon, photon, tau or jet are shown in table 4.4.

Expected trigger performance

The trigger performance is an important issue for any analysis at the LHC. For the studies of this thesis the single isolated lepton trigger was considered. This choice was done because the signal topology under study has one lepton (electron or muon) with high p_T in the final state.

A trigger chain is a particular sequence of LVL1, LVL2 and EF triggers (c.f. section 3.2.7). Two trigger chains were considered:

- e25i: composed by the EM25I LVL1 trigger and the e25i LVL2 and EF triggers;
- mu20i: composed by the MU20 or MU40 LVL1 trigger and the mu20i LVL2 and EF triggers.

All the signal and background events were required to pass either e25i or the mu20i trigger chain. The efficiency for this trigger requirement is $(52.9 \pm 0.2)\%$ and $(59.1 \pm 0.2)\%$ for the semileptonic (electron or muon) $t\bar{t}$ signal, respectively (see table 4.5). The trigger effect on the signal depends on the lepton transverse momentum and pseudorapidity, as shown in figure 4.14.

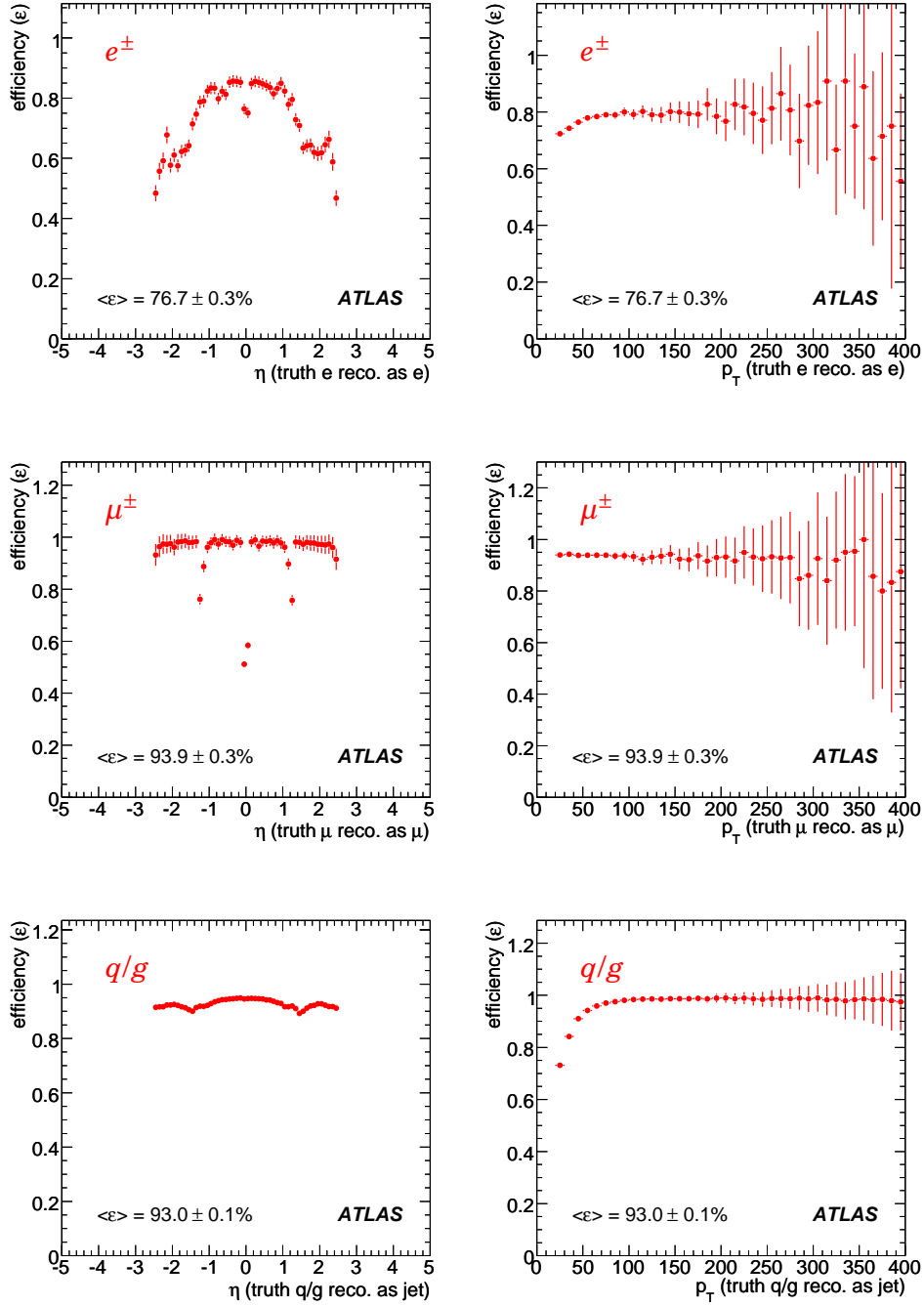


Figure 4.13: Reconstruction efficiencies for electrons, muons and quarks/gluons as function of the generated η and p_T , for the MC@NLO $t\bar{t}$ sample. Only particles with a generated p_T above 25 GeV and $|\eta| < 2.5$ are represented in these plots.

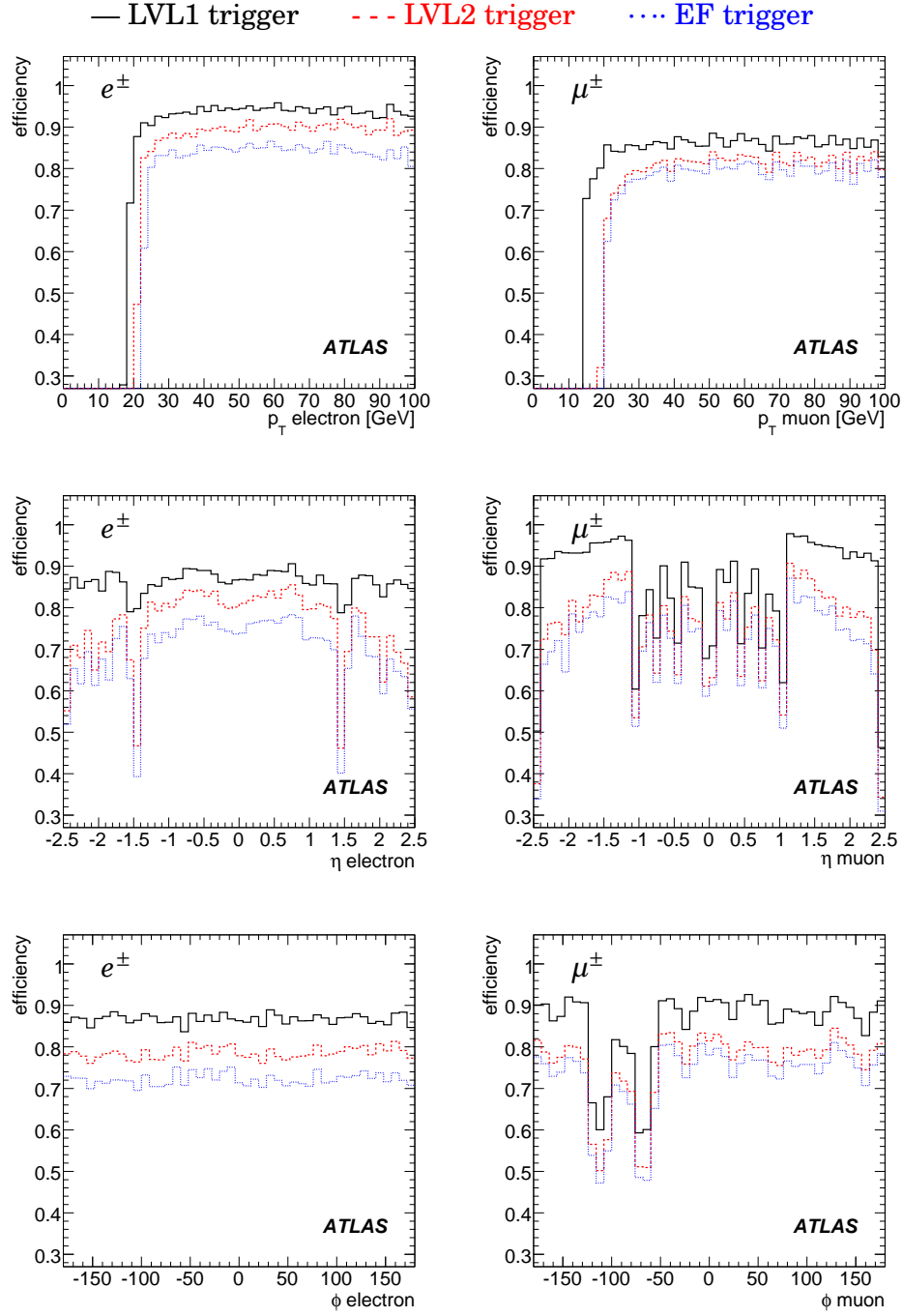


Figure 4.14: *Electrons (left plots) and muons (right plots) reconstruction efficiencies for each trigger level, as a function of p_T , η and ϕ . The single isolated electron (muon) trigger was chosen [e25i (mu20i) trigger chains]. Although no analysis requirements were explicitly applied, the evaluation of these reconstruction efficiencies requires the presence of a reconstructed electron (muon) in the final state.*

The background rejections due to the considered triggers are summarized in table 4.6. These rejections were evaluated with the available Monte Carlo samples and depend, naturally, on the cuts applied at the generator level.

| | LVL1 | LVL2 | EF |
|-----------|----------------|----------------|----------------|
| electrons | 74.4 \pm 0.2 | 61.0 \pm 0.2 | 52.9 \pm 0.2 |
| muons | 73.1 \pm 0.2 | 63.0 \pm 0.2 | 59.1 \pm 0.2 |

Table 4.5: *The trigger efficiency for semileptonic $t\bar{t}$ signal events with an electron (muon) in the final state is shown (in %) for each trigger. The considered LVL1 trigger is EM25I (MU20 or MU40), while the corresponding LVL2 and EF triggers are e25i (mu20i). These efficiencies were evaluated dividing the number of events passing each trigger by the number of signal events with a generated electron (muon) in the final state (no analysis requirements were applied).*

| | trigger rejection (%) |
|--|-----------------------|
| $t\bar{t}$ background (with leptons) | 65.3 \pm 0.3 |
| $t\bar{t}$ background (fully hadronic) | 95.9 \pm 0.1 |
| single top | 60.4 \pm 0.3 |
| W+jets | 65.3 \pm 0.3 |
| W b \bar{b} +jets | 68.4 \pm 0.5 |
| Wc \bar{c} +jets | 69.3 \pm 0.7 |
| Z+jets | 32.0 \pm 0.2 |
| WW, ZZ and WZ | 42.0 \pm 0.8 |

Table 4.6: *Background rejections for the single isolated lepton trigger (e25i or mu20i). The trigger rejection is defined as $1 - \frac{\text{events after trigger}}{\text{events before trigger}}$.*

Chapter 5

EVENT ANALYSIS

THE SIGNAL EVENTS under study have a final state topology characterised by one isolated lepton (electron or muon), missing energy, two b -jets and two light jets. Furthermore, two t -quarks and two W -bosons can be reconstructed from the final state particles. In the present chapter the selection and the full reconstruction of the events are discussed.

The analysis for $L = 10 \text{ fb}^{-1}$ is presented in section 5.1. For this luminosity, the expected amount of data will lead to small statistical errors and the systematic uncertainties should be dominant. Therefore, the Monte Carlo samples obtained from the fast simulation were used. The large statistics of these samples was used to estimate the expected impact of different systematic uncertainties in the analysis.

In order to estimate the ATLAS sensitivity to the Wtb anomalous couplings for the first data, specific analyses for a luminosity of 1 fb^{-1} were also developed and are described in section 5.2. In particular, the possible improvement due to the use of b -tagging was studied by comparing the analyses without and with b -tagging. In these analyses, the full simulation samples were used to evaluate in a more detailed way the detector effects on the observables.

For these analyses, the program `LipCbrAnalysis` was developed. Its design allows a relatively easy processing of the different kind of data formats in which the fast and full Monte Carlo events can be obtained.

5.1 Analysis for $L=10 \text{ fb}^{-1}$

The event selection was done using an analysis performed in two steps, as described in Ref. [125]. In the first level of analysis (the preselection) the events were required to fulfill simple criteria, based on the multiplicity, pseudorapidity and

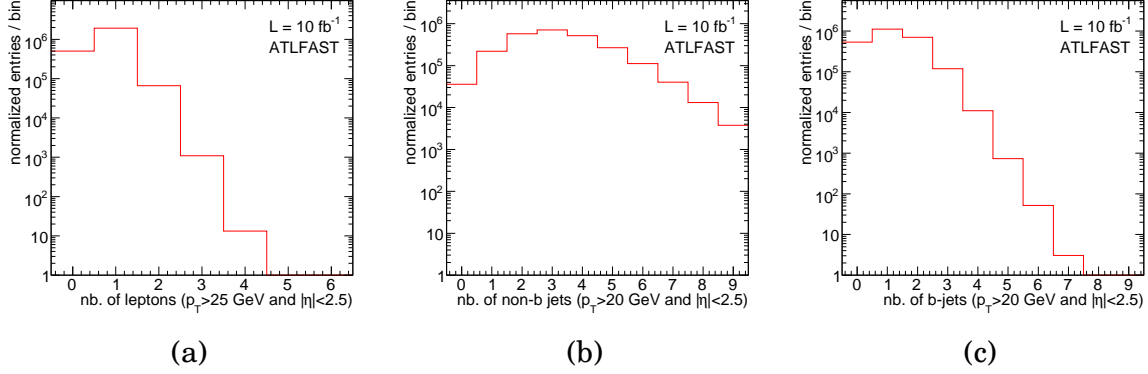


Figure 5.1: *Distributions, before the preselection, of the (a) charged lepton, (b) non b -tagged and (c) b -tagged jet multiplicity for the signal sample (fast simulation, normalized to $L = 10 \text{ fb}^{-1}$). Only charged leptons (jets) with $p_T > 25 \text{ GeV}$ ($p_T > 20 \text{ GeV}$) and $|\eta| < 2.5$ were considered.*

transverse momenta of the final state particles. The aim of the preselection is not only to reject background events, but also to select the signal events for which a full reconstruction of the event kinematics is possible. In the second step of the analysis (the final selection), a discriminant variable, based on the probability of the events being signal or background-like, was built. The event selection was completed by applying a cut on the obtained discriminant variable, reducing the background contamination. After the event selection, the $\cos\theta_\ell^*$ observable is reconstructed and the angular asymmetries, the W helicity fractions and the W helicity ratios are evaluated, as described in chapter 2.

5.1.1 Preselection

The full kinematical reconstruction of the $t\bar{t} \rightarrow \ell \nu b \bar{b} q \bar{q}'$ signal events requires the presence in the final state of one charged lepton and four jets, with two of them being tagged as b -jets. The distributions of the number of reconstructed charged leptons, non b -tagged and b -tagged jets in the signal sample are shown in figure 5.1. In order to avoid forward and low energy objects, only leptons (jets) with $p_T > 25 \text{ GeV}$ ($p_T > 20 \text{ GeV}$) and $|\eta| < 2.5$ were considered¹. In addition to these topological requirements, the signal to background ratio was improved in the preselection by requiring the events to have only one lepton (with $p_T > 25 \text{ GeV}$ and $|\eta| < 2.5$), at least four jets (with $p_T > 20 \text{ GeV}$ and $|\eta| < 2.5$), exactly two of these jets being tagged as b -jets and missing transverse momentum above 20 GeV .

The hadronic W reconstruction was done with the two non- b jets with highest transverse momentum. The invariant mass of these two jets is represented in figure 5.2, after the preselection level.

¹ Throughout this section, only the leptons and jets fulfilling this criteria are taken into account in the kinematical reconstruction of the event. These leptons and jets are ordered by decreasing p_T : the leading lepton (jet) is the one with highest p_T and $|\eta| < 2.5$. Furthermore, only isolated leptons were reconstructed by ATLFast, as described in section 4.2.2.

The mass of the hadronic top, shown in figure 5.2, was reconstructed as the invariant mass of the hadronic W and the b -jet closer to the W .

Although the leptonic W momentum cannot be directly reconstructed due to the presence of an undetected neutrino in the final state, the neutrino tetramomentum can be estimated. The transverse missing energy was assumed to be the transverse momentum of the neutrino and its longitudinal component was determined, with a quadratic ambiguity, by constraining the leptonic W mass (calculated as the invariant mass of the neutrino and the charged lepton) to its on-shell value $m_W = 80.4 \text{ GeV}$ [29]:

$$\begin{aligned}
 p_{z\nu} &= \frac{-b \pm \sqrt{b^2 - 4ac}}{2a} \\
 a &= \left(\frac{p_{z\ell}}{p_\ell} \right)^2 - 1 \\
 b &= 2 \left(\frac{p_{x\ell} \not{p}_x + p_{y\ell} \not{p}_y}{p_\ell} + \frac{m_W^2}{2p_\ell} \right) \frac{p_{z\ell}}{p_\ell} \\
 c &= \left(\frac{p_{x\ell} \not{p}_x + p_{y\ell} \not{p}_y}{p_\ell} + \frac{m_W^2}{2p_\ell} \right)^2 - \not{p}_T^2,
 \end{aligned} \tag{5.1}$$

with $\not{p}_{(x,y)}$ being the (x,y) components of the missing transverse momentum and $p_{(x,y,z)\ell}$ being the (x,y,z) components of the charged lepton transverse momentum. The twofold quadratic ambiguity in the longitudinal component was solved by choosing the solution leading to the minimum mass difference between the hadronic and the leptonic top quarks.

No solution for the longitudinal component of the neutrino momentum is found for 29% and 35% of the previously selected signal and background events, respectively. Different approaches had been proposed to recover this events [126, 108]. The events reconstructed with such solutions have a worst resolution for the leptonic top quark and W -boson reconstruction and, therefore, events for which no $p_{z\nu}$ solution is found (equation 5.1) were rejected in the present analysis.

The leptonic top was reconstructed with the leptonic W and the remaining b -quark. The reconstructed invariant mass of the leptonic top and other relevant kinematical variables are shown in figure 5.2 after the preselection.

The number of signal and background events (normalised to $L = 10 \text{ fb}^{-1}$) and the signal efficiency after the preselection are shown in table 5.1. At this level, the $t\bar{t}$ background (in particular the semileptonic events with the leptonic decay $W \rightarrow \tau\nu_\tau$ and the dileptonic events) is dominant (68.7% of the total background). The single top and W +jets background represent 23.2% and 6.8% of the background, respectively. Although no $b\bar{b}$ background events were selected at this level, it should be noticed that, due to the large $b\bar{b}$ production cross-section, the statistical error associated to these events is large. For this reason, the $b\bar{b}$ background will have to be estimated using data-driven methods [108].

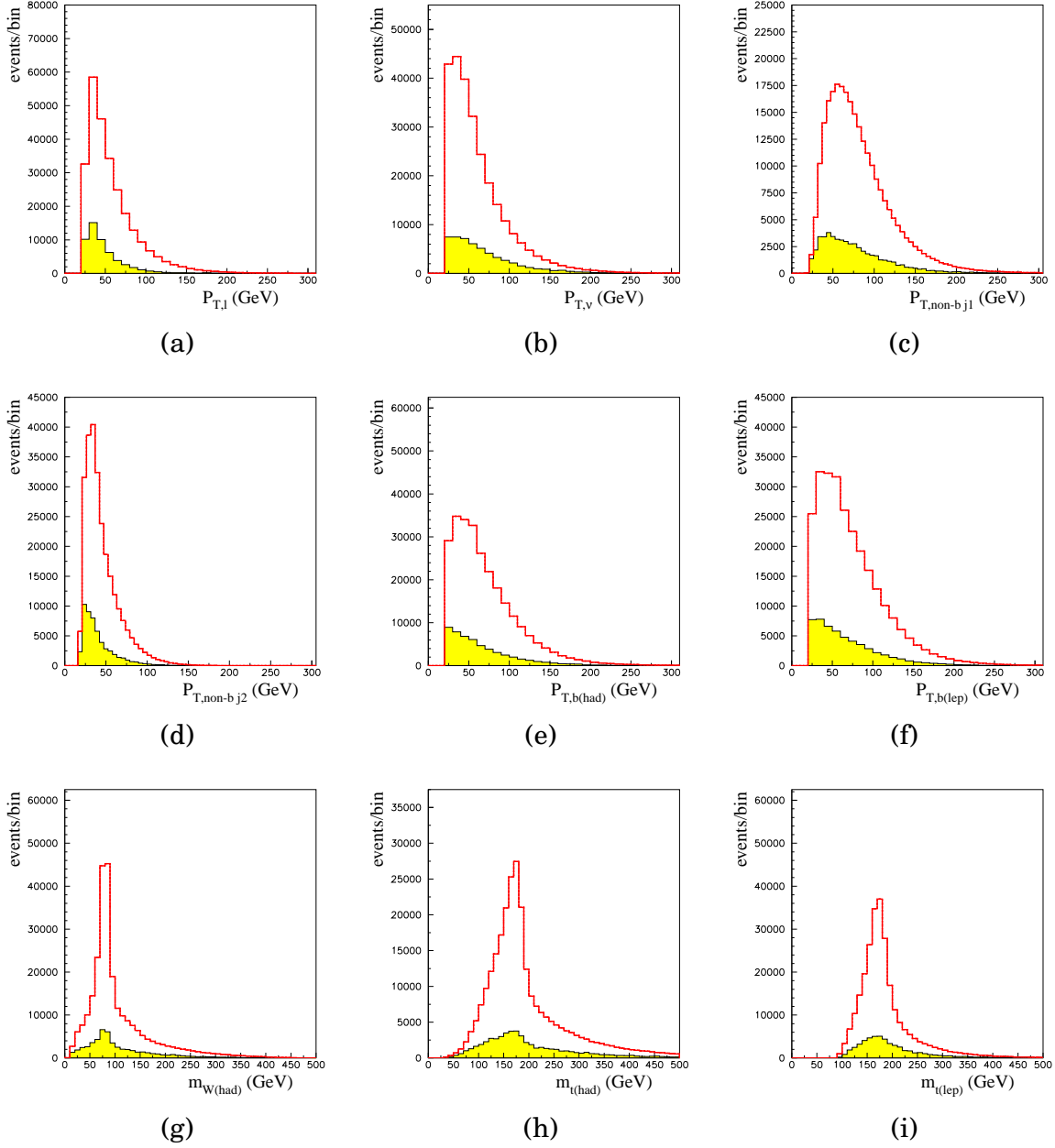


Figure 5.2: *Kinematical distributions after the preselection level for (a) the transverse momentum of the charged lepton; (b) the neutrino; (c-d) the p_T of the two non-b jets used in the hadronic W reconstruction; the b-jet from (e) the hadronic and (f) leptonic top quarks. Invariant mass distributions of the (g) hadronic W -boson; (h) the hadronic top and (i) the leptonic top. The $t\bar{t}$ signal (full line) and the SM backgrounds (shaded region) are normalised to $L = 10 \text{ fb}^{-1}$.*

| process | selected events (preselection) |
|---|--|
| signal ($t\bar{t} \rightarrow \ell \nu b\bar{b} q\bar{q}'$, $\ell = e^\pm, \mu^\pm$) | 262111 ± 382 (10.88 ± 0.02) % |
| $t\bar{t}$ (other) | 36745 ± 143 |
| Single t | 12410 ± 109 |
| Z +jets | 566 ± 85 |
| W +jets | 3627 ± 455 |
| WW, ZZ, ZW | 109 ± 8 |
| total background | 53457 ± 497 |
| S/B | 4.9 ± 0.1 |

Table 5.1: Number of signal (S) and background (B) events, normalised to $L = 10 \text{ fb}^{-1}$, after the preselection. Although no $b\bar{b}$ background events were selected, it should be noticed that the statistical error of these samples is large (due to the large $b\bar{b}$ production cross-section).

5.1.2 Final selection

After the preselection, a probabilistic type of analysis was used. For this, a signal likelihood (\mathcal{L}_S) and a background likelihood (\mathcal{L}_B) were calculated for each selected event by using probability density functions (p.d.f.) based on relevant physical variables. Neglecting correlations, the signal and background likelihoods for each preselected event are given by:

$$\mathcal{L}_S = \prod_{i=1}^n P_i^S(x_i), \quad \mathcal{L}_B = \prod_{i=1}^n P_i^B(x_i), \quad (5.2)$$

where n is the number of used p.d.f. $P_i^S(x_i)$ and $P_i^B(x_i)$ are the signal and background probabilities evaluated from the i^{th} p.d.f., as represented in figure 5.3. The discriminant variable is defined as $\mathcal{L}_R = \log_{10}(\mathcal{L}_S/\mathcal{L}_B)$.

The kinematical variables used to build the p.d.f. were the following:

- the hadronic W mass;
- the hadronic and leptonic top masses;
- the transverse momentum of the b -jets associated to the hadronic and leptonic top quarks and
- the transverse momentum of the jets used in the hadronic W reconstruction.

These seven variables are shown in figure 5.2 (c-i) and the discriminant variable is shown in figure 5.4 (a).

As expected from the choice of the p.d.f.², a significant improvement in the reconstruction of the top quarks and hadronic W -boson reconstruction can be achieved by selecting events with higher values of the discriminant variable. This effect can be seen in figure 5.5, where the reconstructed W and t invariant masses are shown for different cuts on \mathcal{L}_R .

² The hadronic W mass and the leptonic and hadronic top masses were used as p.d.f.

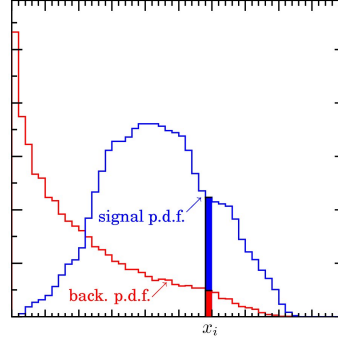


Figure 5.3: *Example of the signal (background) likelihood evaluation using the signal (background) p.d.f.. The signal (background) probability of having one specific event with value x_i is calculated as the normalized area of the corresponding histogram bin. The represented event has an higher probability of being signal-like than background-like.*

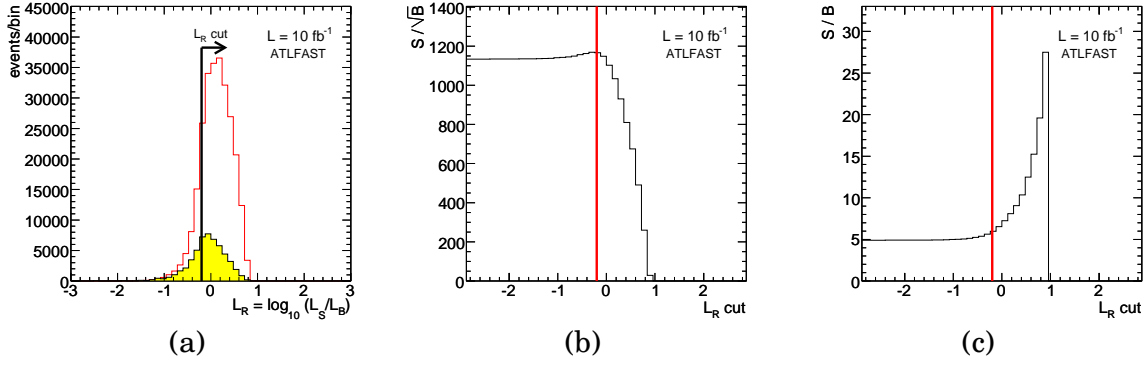


Figure 5.4: (a) *Discriminant variable distribution for the SM background (shaded region) and the $t\bar{t}$ signal (full line), normalised to $L = 10 \text{ fb}^{-1}$ (fast simulation events). The corresponding (b) S/\sqrt{B} and (c) S/B distributions (as a function of the L_R cut) are also shown. The final event selection was done by applying the cut $\mathcal{L}_R > -0.2$.*

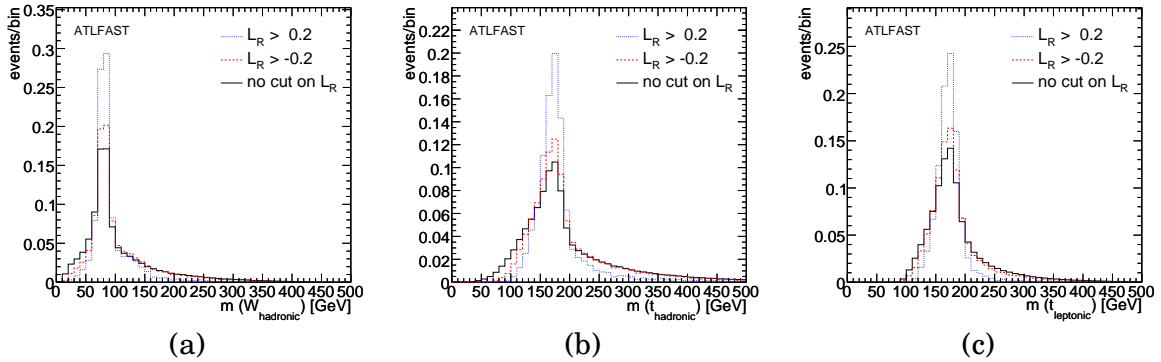


Figure 5.5: *Effect of the discriminant variable cut on the (a) hadronic W mass; (b) hadronic top mass and (c) leptonic top mass (signal fast simulation samples). The distributions were normalized to unity for a better comparison.*

| process | selected events (final selection) |
|---|---|
| signal ($t\bar{t} \rightarrow \ell \nu b\bar{b} q\bar{q}'$, $\ell = e^\pm, \mu^\pm$) | 220024 ± 346 (9.13 ± 0.02) % |
| $t\bar{t}$ (other) | 27060 ± 121 |
| Single t | 7600 ± 83 |
| Z +jets | 253 ± 46 |
| W +jets | 1307 ± 152 |
| WW, ZZ, ZW | 51 ± 5 |
| total background | 36271 ± 217 |
| S/B | 6.1 ± 0.1 |

Table 5.2: Number of signal $t\bar{t} \rightarrow \ell \nu b\bar{b} q\bar{q}'$ (S) and background (B) events, normalised to $L = 10 \text{ fb}^{-1}$, after the final selection.

In figures 5.4 (b-c) the signal to background ratios S/\sqrt{B} and S/B as a function of the discriminant variable cut are shown. The final event selection was done by applying the cut $\mathcal{L}_R > -0.2$ on the discriminant variable. The number of background events (normalised to $L = 10 \text{ fb}^{-1}$) and signal efficiency at this level are shown in table 5.2. The signal to background ratio (S/B) is improved from 4.9 to 6.1 in the final selection. At this level, the non-signal $t\bar{t}$ events represent 75% of the total background.

Using information from the generation level, the efficiencies for each reconstructed object can be evaluated. For this purpose, an object is considered to be correctly reconstructed if the corresponding generated particle is found within a cone defined by $\Delta R < 0.4$. The reconstruction efficiencies for the charged lepton (e^\pm or μ^\pm), the neutrino and the leptonic and hadronic b , W and t are shown in table 5.3. As expected, these efficiencies were improved by the final selection. Although the lepton is correctly reconstructed in almost 100% of the cases, the reconstruction efficiencies for the other objects are lower. The loss of efficiency for the b -quarks is mainly due to mistag of c and light jets by the b -tagging algorithm and to the criteria used to choose the leptonic and hadronic b . The W -boson and t -quark reconstruction is affected by the inefficiencies in the detection of final state particles and in the assignment of the jets, lepton and neutrino. Nevertheless, in more than 20% of the selected signal events the ΔR between the reconstructed top quark and the generated one is smaller than 0.4. The ΔR separation between each of the reconstructed objects and the corresponding generated particle is shown in figure 5.6. The relative differences between the momenta of the reconstructed and generated objects (as a function of the generated object momentum) are shown in figure 5.7.

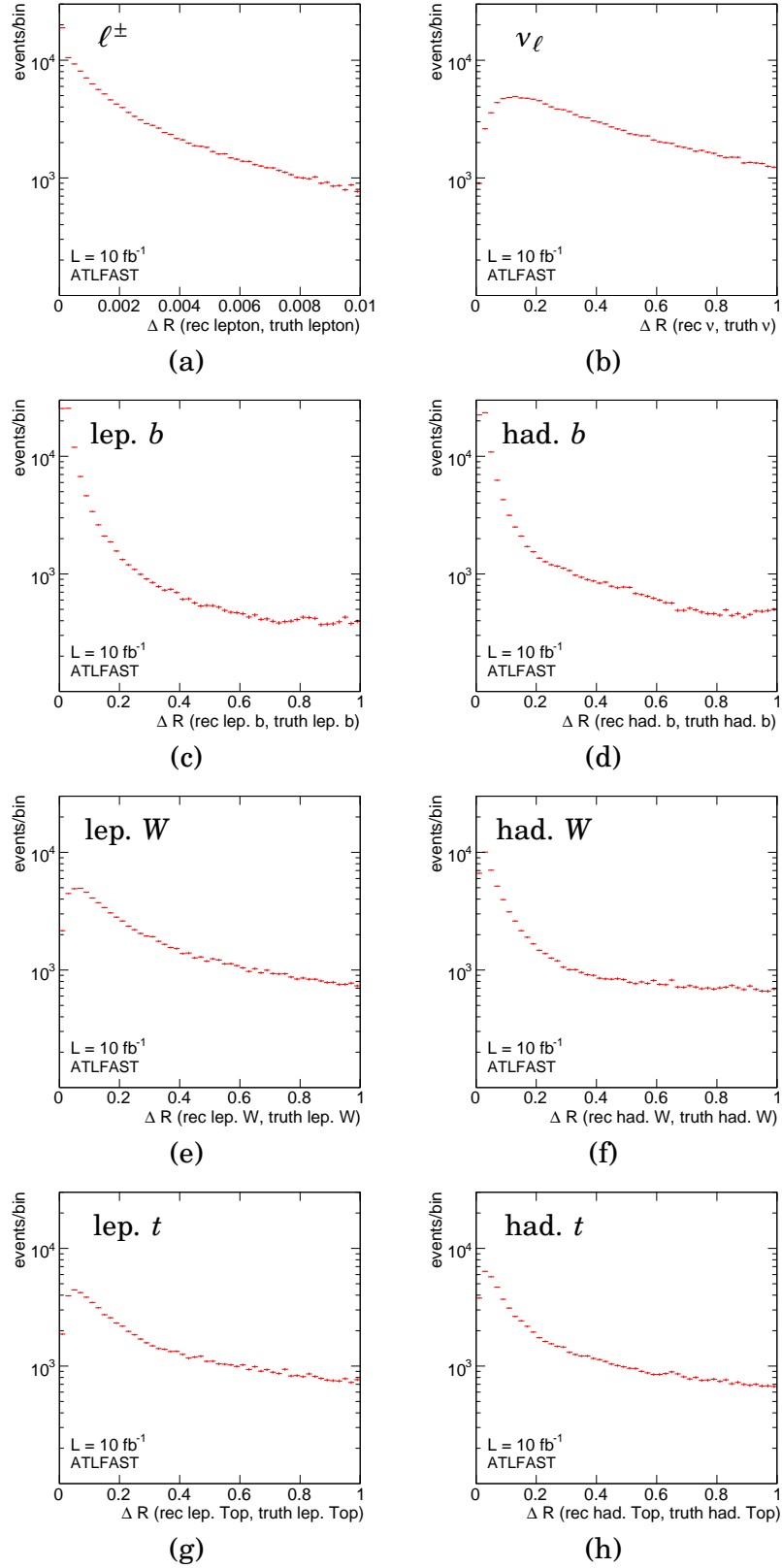


Figure 5.6: $\Delta R(\text{reconstructed, generated})$ for the fast simulation analysis: (a) lepton (electron or muon); (b) neutrino; (c-d) leptonic and hadronic b -jets; (e-f) leptonic and hadronic W -bosons; (g-h) leptonic and hadronic top quarks.

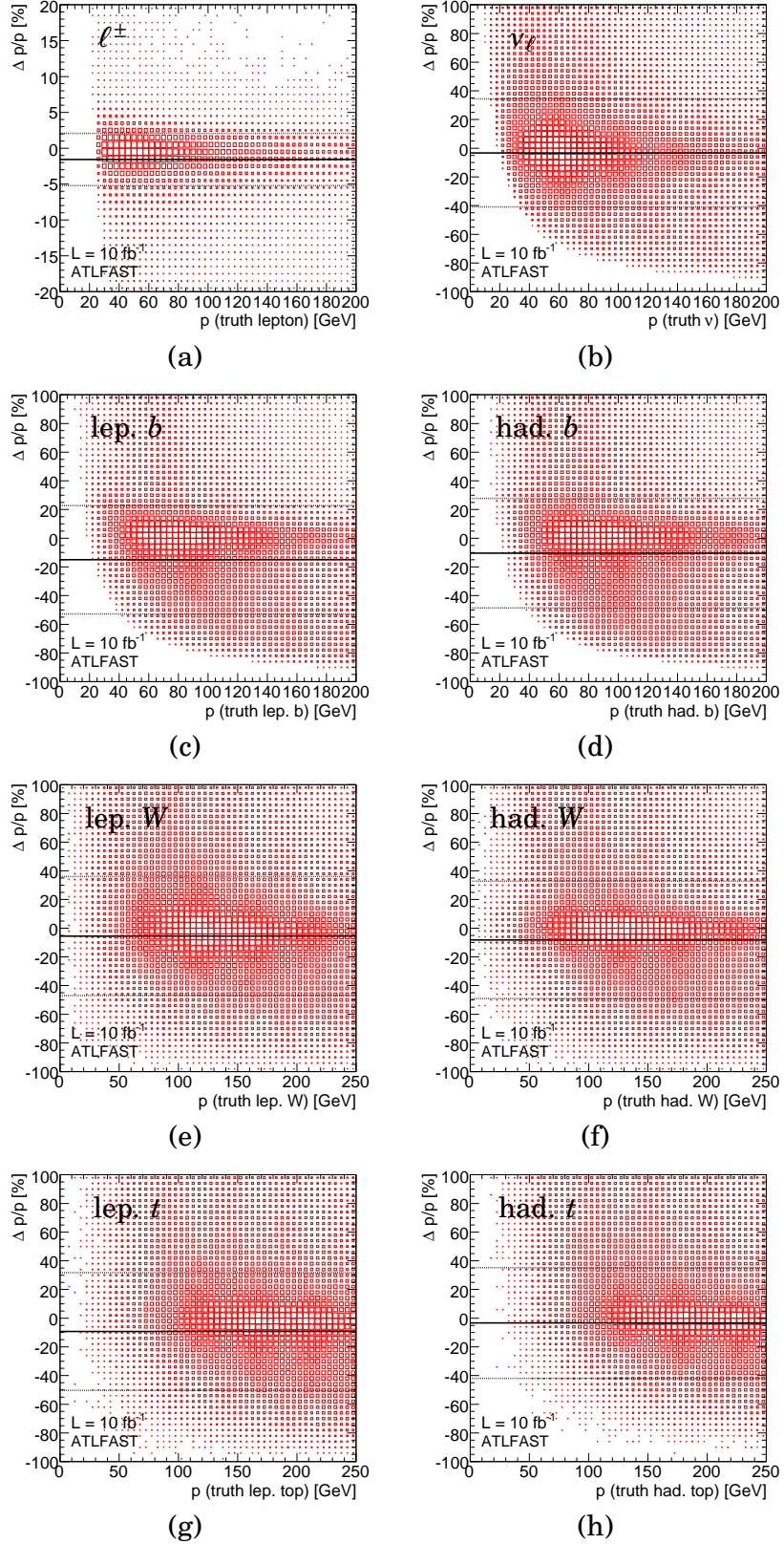


Figure 5.7: $(\Delta p)/p = (p_{\text{reconstructed}} - p_{\text{generated}})/p_{\text{generated}}$ as a function of the generated momentum for the fast simulation analysis: (a) lepton (electron or muon); (b) neutrino; (c-d) leptonic and hadronic b -jets; (e-f) leptonic and hadronic W -bosons; (g-h) leptonic and hadronic t quarks. The horizontal solid line shows the mean value of $(\Delta p)/p$ and the horizontal dashed lines show the mean value \pm the RMS (root mean square) of this distribution. The corresponding $\Delta p/p$ projections are shown in figure 5.8.

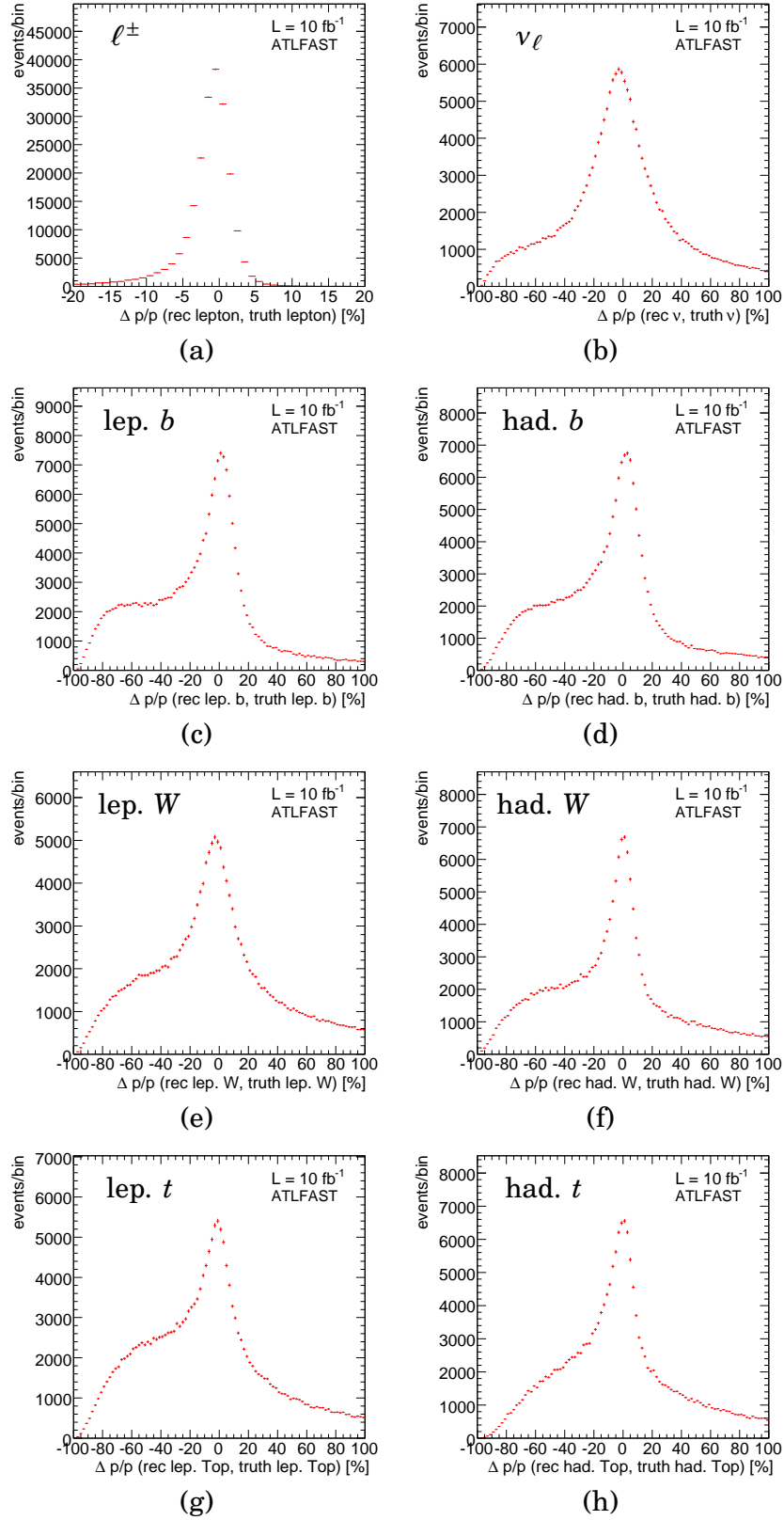


Figure 5.8: $(\Delta p)/p = (p_{\text{reconstructed}} - p_{\text{generated}})/p_{\text{generated}}$ for the fast simulation analysis: (a) lepton (electron or muon); (b) neutrino; (c-d) leptonic and hadronic b -jets; (e-f) leptonic and hadronic W -bosons; (g-h) leptonic and hadronic top quarks.

| | preselection | final selection |
|---------------------------------|----------------|-----------------|
| lepton (e^\pm or μ^\pm) | 99.6 ± 0.2 | 99.6 ± 0.2 |
| leptonic b | 43.4 ± 0.1 | 44.2 ± 0.1 |
| hadronic b | 40.6 ± 0.1 | 41.4 ± 0.1 |
| neutrino | 35.0 ± 0.1 | 35.8 ± 0.1 |
| leptonic W | 26.3 ± 0.1 | 26.8 ± 0.1 |
| hadronic W | 23.6 ± 0.1 | 25.7 ± 0.1 |
| leptonic t | 20.8 ± 0.1 | 22.6 ± 0.1 |
| hadronic t | 21.4 ± 0.1 | 23.5 ± 0.1 |

Table 5.3: *Efficiencies (in %) for each reconstructed object in the ATLFast analysis (after the preselection and final selection levels). An object is considered to be correctly reconstructed if the corresponding generated particle is found within a cone with $\Delta R < 0.4$ from the reconstructed one.*

5.1.3 W polarization and angular asymmetries

The $\cos\theta_\ell^*$ distribution³, to be observed in the experiment, will include the $t\bar{t}$ signal as well as the SM backgrounds, and will be affected by the detector resolution, $t\bar{t}$ reconstruction and selection criteria. In order to recover the theoretical distribution, it will be necessary to:

1. subtract background from data and
2. correct for the detector and reconstruction effects.

For this purpose, two sets of signal and background event samples were used: one “experimental” set, which simulates a possible experimental result, and one “reference” set, which is used to parameterise the mentioned effects and correct the first sample.

After subtracting reference background samples, the “experimental” distribution was multiplied by a correction function in order to recover the SM expectation. The correction function was determined assuming that the charged lepton distribution corresponds to the SM one. If a deviation from SM predictions (corresponding to anomalous couplings) is found, the correction function will have to be modified accordingly, and the theoretical distribution recalculated in an iterative process. These issues have been analysed in detail in Ref. [126], where it is shown that this process quickly converges. The correction function was calculated, for each bin of

³ As described in section 2.3.2, θ_ℓ^* is the angle between the charged lepton momentum (in the W -boson rest frame) and the W boson momentum (in the top quark rest frame). In the present analysis this distribution was obtained from the angle $\theta_{\ell b}$ between the charged lepton and leptonic b -quark momenta in the W -boson rest frame: $\theta_\ell^* = \pi - \theta_{\ell b}$. As the W -boson is produced with some boost (*c.f.* figure 4.6), the W rest frame allows to partially avoid the colinearity between the lepton and the b -quark. For comparison, the reconstructed angle between the charged lepton and the leptonic b -quark in the laboratory frame is shown in figure 5.9.

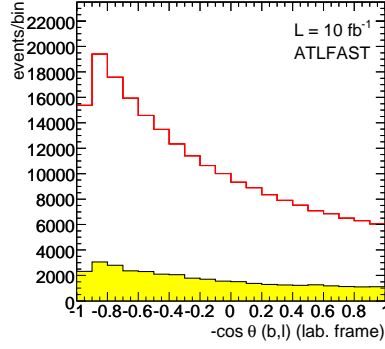


Figure 5.9: Signal (solid line) and background (shaded region) distribution of the angle between the charged lepton and the leptonic b -quark in the laboratory frame (fast simulation analysis for $L = 10 \text{ fb}^{-1}$). These distributions are shown after the final selection level.

the $\cos\theta_\ell^*$ distribution, through the division of the number of events at the generator level by the number of events after the event selection, using the reference sample. The Monte Carlo $\cos\theta_\ell^*$ distribution obtained after the simulation is shown in figure 5.10, together with the theoretical distribution and the correction function obtained from the reference sample.

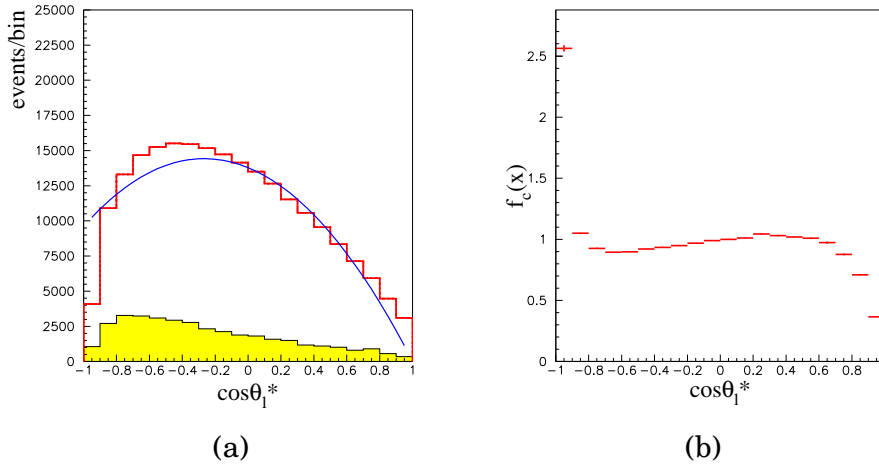


Figure 5.10: Reconstructed $\cos\theta_\ell^*$ distribution (a) and its correction function (b). In the first plot the $t\bar{t}$ signal (thick full line) and the SM backgrounds (shaded region) are normalised to $L = 10 \text{ fb}^{-1}$, while the thin full line represents the generated $\cos\theta_\ell^*$ distribution.

The angular asymmetries (A_{FB} , A_+ and A_-) were evaluated through a simple counting of the number of events below and above a specific value of the corrected $\cos\theta_\ell^*$ (c.f. equation 2.11). Thus, the asymmetry measurements are not biased by the extreme values of the angular distributions, where the correction function largely

| | theoretical | reconstructed |
|-----------------|----------------------|----------------------|
| F_0 | 0.703 | 0.700 ± 0.003 |
| F_L | 0.297 | 0.299 ± 0.003 |
| F_R | 3.6×10^{-4} | 0.0006 ± 0.0012 |
| ρ_L | 0.423 | 0.4274 ± 0.0080 |
| ρ_R | 5.1×10^{-4} | 0.0004 ± 0.0021 |
| A_{FB} | -0.2220 | -0.2231 ± 0.0035 |
| A_+ | 0.5482 | 0.5472 ± 0.0032 |
| A_- | -0.8397 | -0.8387 ± 0.0018 |

Table 5.4: *Theoretical and reconstructed values of helicity fractions, helicity ratios and angular asymmetries for $L = 10 \text{ fb}^{-1}$. The statistical error on the observables is shown.*

deviates from unity and special care is required (see figure 5.10). The helicity fractions and ratios were obtained from a fit to the corrected $\cos\theta_\ell^*$ distribution. The theoretical and reconstructed values of these observables are summarized in table 5.4.

5.1.4 Systematic uncertainties

Due to the excellent statistics achievable at LHC, which is apparent in the statistical errors of table 5.4, the systematic errors are expected to play a crucial role in the measurement of the angular distributions and asymmetries for a luminosity of 10 fb^{-1} or larger. A detailed study of the different systematic uncertainties in the determination of the correction functions has, therefore, to be made. The systematic uncertainties in the considered observables were estimated by comparing the reference values with the ones obtained using Monte Carlo samples with different parameters for the generation, simulation and reconstruction. The choice of these parameters was done in a way that allows a comparison with previous analyses [126, 101].

The following systematic uncertainties sources were considered:

1. *Monte Carlo generator:* The correction function obtained from the $t\bar{t}$ reference sample (generated with TopReX) was applied to a sample generated with ALPGEN. The difference between the values obtained at the generator level and after the ALPGEN simulation was considered as a systematic uncertainty.
2. *Structure functions:* The correction function obtained from a reference sample generated with the CTEQ 5L PDF set was applied to the samples generated with the CTEQ 6L and MRST 2001 PDFs. The largest deviations found were considered as the systematic error associated to the structure functions.
3. *Top mass dependence:* Samples corresponding to top masses of 170, 175 and 180 GeV were used, and the influence of m_t on the values obtained for the

corrected observables (using correction functions for $m_t = 175$ GeV) was determined. The systematic error was obtained from a linear fit of the observable values as a function of the top mass. The considered m_t uncertainty was 2 GeV. These fits are shown in appendix B.

4. *ISR and FSR*: The effect of ISR and FSR was studied following Ref. [101]. A Monte Carlo event sample without ISR and FSR was used. The results of the reference sample (with ISR and FSR) were compared with those obtained by adding to it a normalised fraction of the sample without ISR nor FSR (from 0% to 25%, in steps of 5%). The values obtained for the observables were fitted with a linear function and the systematic error was considered as the effect of the presence of 20% (a conservative estimate of our level of knowledge of ISR and FSR) of the sample without ISR, FSR (see appendix B).
5. *b-jet tagging efficiency*: The value of the *b*-jet tagging efficiency (and the corresponding *c*-jet and light jet rejection factors) was varied from 50 to 70%, in steps of 5%, and the values obtained for the observables were fitted with a linear function (see appendix B). The systematic error was considered as the effect on the observables of a variation of 5% in the *b*-jet tagging efficiency, as compared with the standard value of 60%.
6. *b-jet energy scale*: The value of the *b*-jet energy scale was changed from -5 to +5%, and the values obtained for the observables were fitted with a linear function (see appendix B). The systematic error was considered as the effect of a variation of 3% in the *b*-jet energy scale.
7. *Light jet energy scale*: The value of the energy scale of the light jets was changed from -3 to +3%, and the values obtained for the observables were fitted with a linear function (see appendix B). The systematic error was considered as the effect of a variation of 1% in the energy scale of the light jets.
8. *Background*: The background global normalization was varied from -25 to 25%, in steps of 5%, and the values obtained for the observables were fitted with a linear function (see appendix B). The systematic error was considered as the effect of a variation of 10% on the background level (which takes into account the uncertainties in the cross-sections).
9. *Pile-up*: The effect of pile-up events was studied by comparing the values of the observables obtained with and without adding pile-up events (2.3 events in average were assumed).
10. *b-quark fragmentation*: The parameter ϵ_b in the Peterson parameterisation for *b*-quark fragmentation [91] was changed from -0.006 to -0.0035 [101]. The difference in the observables values was considered as the systematic error.

The systematic errors in each observable, resulting from these theoretical and simulation uncertainties, are collected in table 5.5. It can be seen that ρ_R and A_- have small total systematic errors. In the case of ρ_R , the improvement over F_R

| | F_0 | F_L | F_R | ρ_L | ρ_R | A_{FB} | A_+ | A_- |
|-------------------------------|--------|--------|--------|----------|----------|-----------------|--------|--------|
| generator | 0.0002 | 0.0002 | 0.0004 | 0.0006 | 0.0000 | 0.0035 | 0.0015 | 0.0006 |
| PDFs | 0.0032 | 0.0022 | 0.0009 | 0.0046 | 0.0008 | 0.0021 | 0.0005 | 0.0014 |
| m_t | 0.0065 | 0.0060 | 0.0006 | 0.0124 | 0.0007 | 0.0034 | 0.0039 | 0.0005 |
| ISR+FSR | 0.0116 | 0.0113 | 0.0003 | 0.0218 | 0.0001 | 0.0046 | 0.0049 | 0.0011 |
| b -tag eff. | 0.0065 | 0.0062 | 0.0003 | 0.0126 | 0.0003 | 0.0039 | 0.0046 | 0.0004 |
| E_b scale | 0.0028 | 0.0030 | 0.0002 | 0.0061 | 0.0002 | 0.0021 | 0.0017 | 0.0005 |
| E_j scale | 0.0034 | 0.0037 | 0.0002 | 0.0074 | 0.0002 | 0.0038 | 0.0023 | 0.0014 |
| back. norm. | 0.0001 | 0.0000 | 0.0000 | 0.0001 | 0.0000 | 0.0001 | 0.0000 | 0.0001 |
| pile-up | 0.0091 | 0.0086 | 0.0005 | 0.0175 | 0.0002 | 0.0080 | 0.0051 | 0.0006 |
| b frag. | 0.0049 | 0.0037 | 0.0012 | 0.0078 | 0.0011 | 0.0045 | 0.0000 | 0.0012 |
| total $\sigma_{\text{syst.}}$ | 0.0189 | 0.0178 | 0.0018 | 0.0356 | 0.0016 | 0.0130 | 0.0099 | 0.0028 |

Table 5.5: Sources of systematic error in the determination of helicity fractions, helicity ratios and angular asymmetries (fast simulation analysis for $L = 10 \text{ fb}^{-1}$).

is due to the partial cancellation of the systematic errors in the ratio, while the opposite happens in the case of ρ_L , compared to F_L . The ISR/FSR and pile-up are the largest sources of uncertainty for the F_0 , F_L , ρ_L , A_{FB} and A_+ observables, while the PDFs and b -jet fragmentation are the dominant systematic errors for F_R , ρ_R and A_- .

The effect of the systematic uncertainties on the W helicities was found to be smaller with respect to a previous analysis [126]. In the present analysis, the W helicity fractions and ratios were obtained by fitting the angular distribution from -0.99 to $+0.99$, and it should be stressed that a dependence of the systematic error with the range of the fit was observed. If the fit is performed between -0.89 and $+0.89$, the systematic errors on F_0 , F_L and F_R are respectively 0.0206, 0.0188 and 0.0033 (in good agreement with the results of Ref. [126]). However, if the fit is performed in the range $[-0.89, +0.99]$ the results are respectively 0.0190, 0.0182 and 0.0017, in good agreement with the values on table 5.5. This implies that the correct reconstruction of the most extreme bins of the angular distribution is particularly important to control the error associated to the W polarisation measurements, if the fitting method is used. In the case of the asymmetries, the smaller errors found for A_{\pm} are due to the greater stability of these measurements, once they were obtained by counting events, instead of fitting the $\cos\theta_\ell^*$ distribution.

It should be pointed out that the selection of z for the definition of A_{\pm} (equations 2.11) has not been optimised in order to achieve smaller systematic errors. Instead, these asymmetries have been defined in a simple way which allows to reconstruct easily the helicity fractions, using the equations 2.14. The expected results for $L = 10 \text{ fb}^{-1}$, including statistical and systematic uncertainties, are summarised in table 5.6.

| | | | |
|-----------------|---------|---------------------------|--------------------------|
| F_0 | 0.700 | $\pm 0.003(\text{stat})$ | $\pm 0.019(\text{sys})$ |
| F_L | 0.299 | $\pm 0.003(\text{stat})$ | $\pm 0.018(\text{sys})$ |
| F_R | 0.0006 | $\pm 0.0012(\text{stat})$ | $\pm 0.0018(\text{sys})$ |
| ρ_L | 0.4274 | $\pm 0.0080(\text{stat})$ | $\pm 0.0356(\text{sys})$ |
| ρ_R | 0.0004 | $\pm 0.0021(\text{stat})$ | $\pm 0.0016(\text{sys})$ |
| A_{FB} | -0.2231 | $\pm 0.0035(\text{stat})$ | $\pm 0.0130(\text{sys})$ |
| A_+ | 0.5472 | $\pm 0.0032(\text{stat})$ | $\pm 0.0099(\text{sys})$ |
| A_- | -0.8387 | $\pm 0.0018(\text{stat})$ | $\pm 0.0028(\text{sys})$ |

Table 5.6: *Summary of the results obtained from the simulation for the observables studied, including statistical and systematic uncertainties (fast simulation analysis for $L = 10 \text{ fb}^{-1}$).*

5.2 Analyses for $L=1 \text{ fb}^{-1}$

In this section the analyses developed for the study of the Wtb vertex with $L = 1 \text{ fb}^{-1}$ of data are presented. For these analyses, the full simulation Monte Carlo events were used. In order to be prepared for the first LHC data, an analysis without using the b -tagging tool [68] was developed (section 5.2.1). Once b -tagging is well understood, the analysis can be improved by using additional information (section 5.2.2).

5.2.1 Analysis without b -tagging

As for the 10 fb^{-1} analysis, a two-level probabilistic analysis was adopted. In the preselection level, a cleaner sample was obtained by requiring events with exactly one isolated electron (muon) with $|\eta| < 2.5$ and $p_T > 25 \text{ GeV}$ ($p_T > 20 \text{ GeV}$), at least 4 jets with $|\eta| < 2.5$ and $p_T > 30 \text{ GeV}$ and missing transverse momentum above 20 GeV . Additionally, the considered electron or muon and the four jets were required to have no other reconstructed object (electron, muon, photon or jet) within a cone with $\Delta R = 0.4$.

The ATLAS event display software (ATLANTIS [127]) allows the visualization of reconstructed events and the corresponding hits in the detector. As an example, the projections in the plane transverse to the beam axis of two simulated semileptonic $t\bar{t}$ events which pass the above selection criteria are shown in figures 5.11 (event with an electron) and 5.12 (event with a muon).

In order to avoid the use of b -tagging, the full event reconstruction was performed through the minimization of a χ^2 function, defined as

$$\chi^2 = \frac{(m_{\ell\nu ja} - m_t)^2}{\sigma_t^2} + \frac{(m_{jbjcjd} - m_t)^2}{\sigma_t^2} + \frac{(m_{\ell\nu} - m_W)^2}{\sigma_W^2} + \frac{(m_{jcjd} - m_W)^2}{\sigma_W^2}, \quad (5.3)$$

where $m_t = 175 \text{ GeV}$, $m_W = 80.4 \text{ GeV}$, $\sigma_t = 14 \text{ GeV}$ and $\sigma_W = 10 \text{ GeV}$ are the ex-

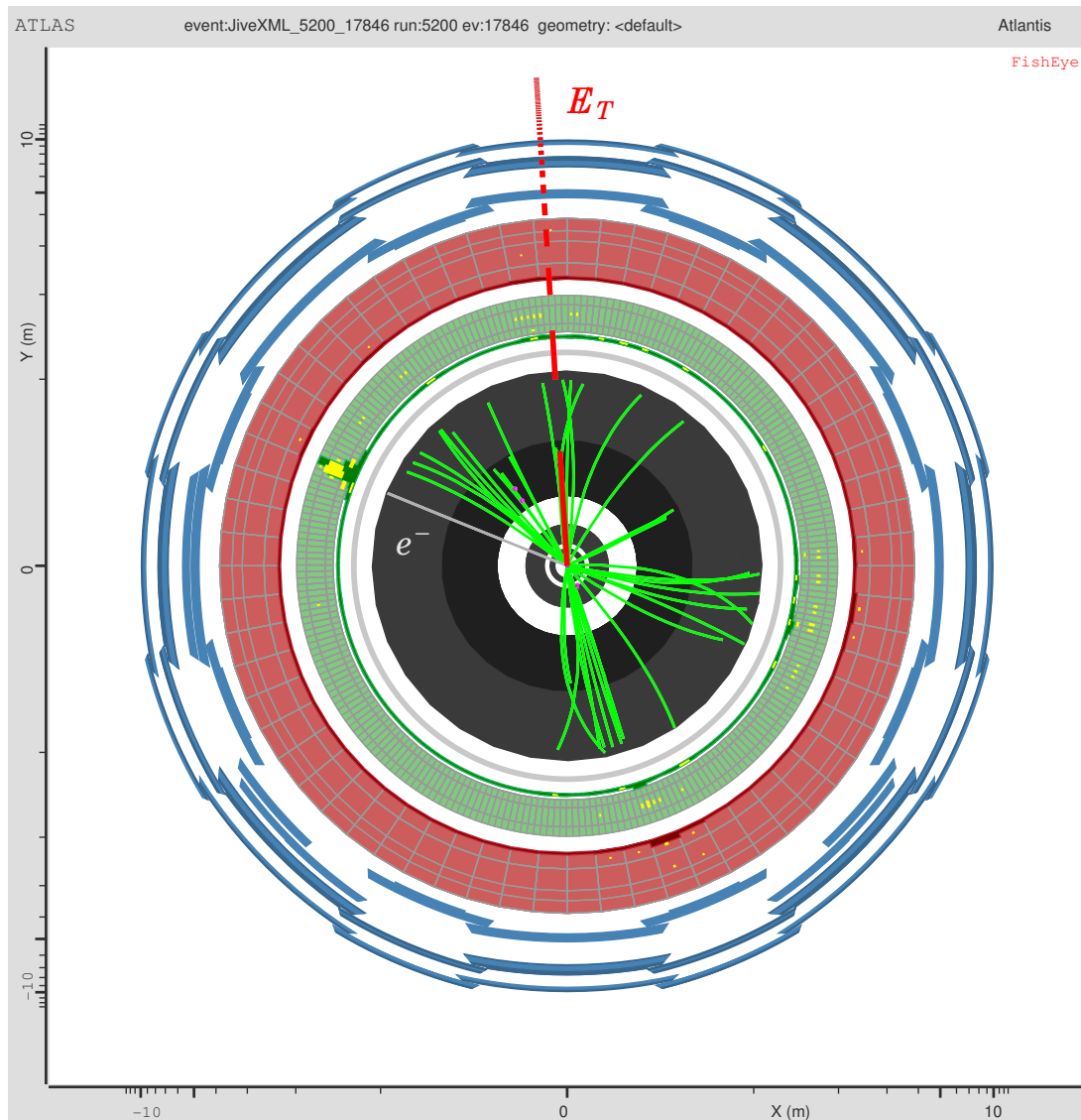


Figure 5.11: ATLANTIS event display of a simulated semileptonic $t\bar{t}$ event. The xy projection (i.e. the plane transverse to the beam axis) is shown. The reconstructed electron has a transverse momentum of 74 GeV and the missing transverse energy is 48 GeV. Only tracks with $p_T > 1$ GeV were represented.

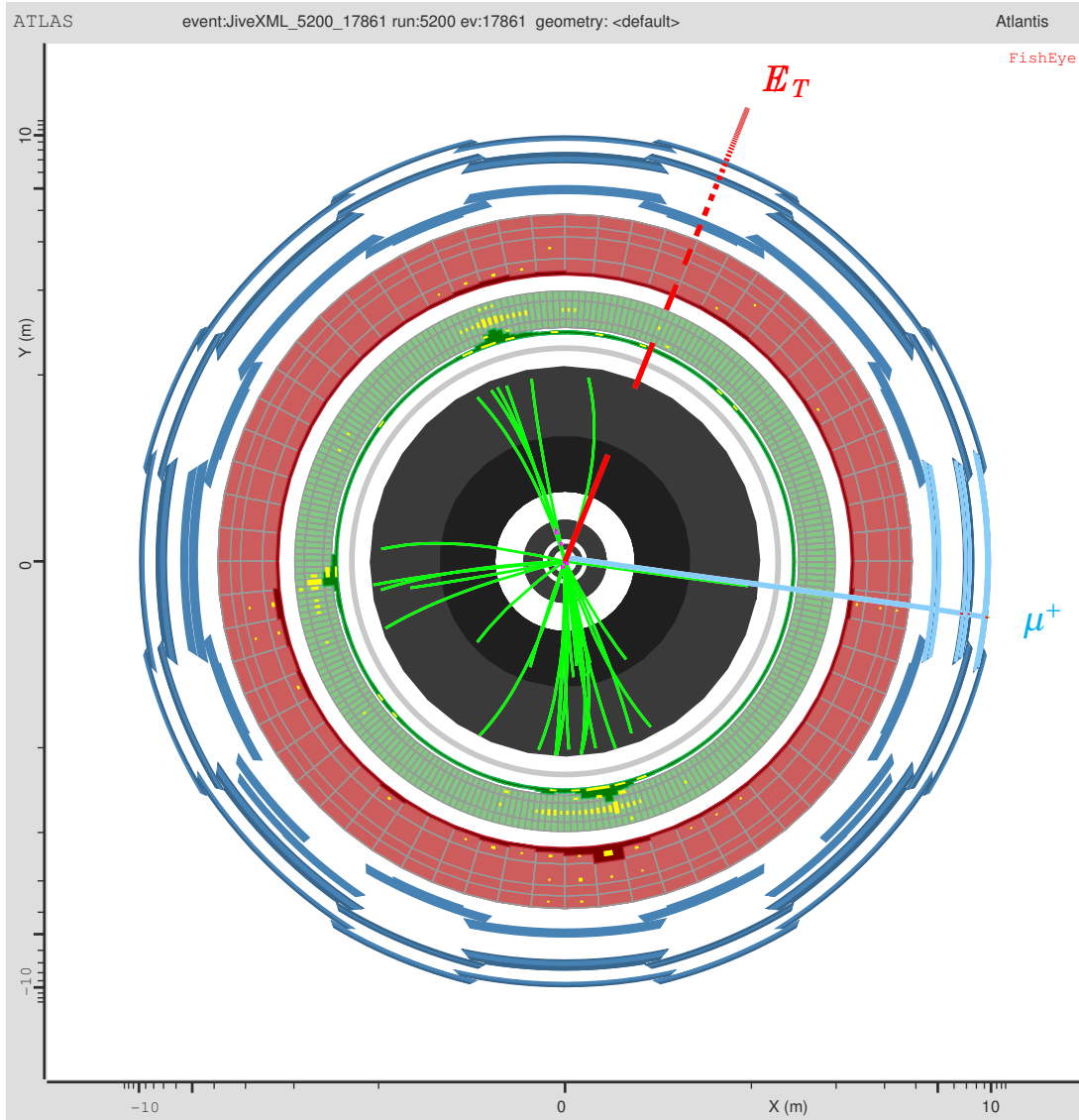


Figure 5.12: ATLANTIS event display of a simulated semileptonic $t\bar{t}$ event. The xy projection (i.e. the plane transverse to the beam axis) is shown. The reconstructed anti-muon has a transverse momentum of 55 GeV and the missing transverse energy is 90 GeV. Only tracks with $p_T > 1$ GeV were represented.

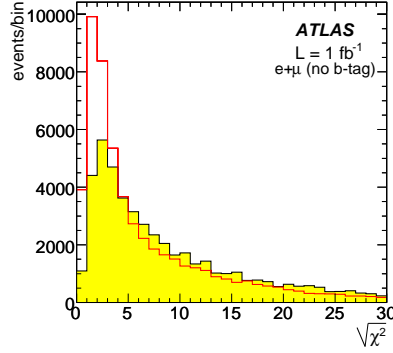


Figure 5.13: Distribution of the $\sqrt{\chi^2}$ variable for signal (solid line) and background (shaded region), normalized to $L = 1 \text{ fb}^{-1}$ (analysis without b -tagging). In this plot no trigger requirements were applied to the events.

pected top quark and W -boson mass resolutions, ℓ represents the selected electron or muon, $m_{\ell\nu}$ is the invariant mass of the electron (muon) and the neutrino, and $j_{a,b,c,d}$ corresponds to all the possible combinations among the four jets with highest p_T (with $m_{\ell\nu j_a}$, $m_{j_b j_c j_d}$ and $m_{\ell\nu j_a}$ being the corresponding invariant masses). The neutrino was reconstructed using the missing transverse energy and allowing the p_z^ν to vary in the range $[-500, +500]$ GeV. The solution corresponding to the minimum χ^2 was chosen for each event. The jets used to reconstruct the hadronic W will be labeled “non- b ” jets and the remaining two are labelled “ b -jets”. It should be stressed that no b -tagging information was used so far.

The χ^2 minimization reconstruction has the advantage of reducing the wrong association of particles, when compared with the method adopted for the $L = 10 \text{ fb}^{-1}$ analysis (*c.f.* section 5.1). It has, however, the drawback of using the value of the top mass as an input.

The distribution of the $\sqrt{\chi^2}$ variable for signal and background is shown in figure 5.13. As this variable tends to have higher values for background than for signal, the preselection was finalized by requiring $\sqrt{\chi^2} < 4$. This cut was done in order to reject the events which cannot be correctly reconstructed (*i.e.* the events with higher values of χ^2). Less than 11% of the signal events were rejected by this cut.

The number of expected signal and background events for $L = 1 \text{ fb}^{-1}$ is shown in table 5.7. The effect of each trigger level on the event preselection was studied by considering the single lepton trigger chains (e25i or mu20i, as described in section 4.3.2). The results are summarized in table 5.7. For comparison, the number of events expected when the selected lepton is required to be an electron (e sample) or a muon (μ sample) are also shown. The trigger efficiency for the electron (muon) signal sample is 86% (77%). The background composition, after the preselection and EF trigger, is shown in table 5.8. At this level, the W +jets processes, including $Wb\bar{b}$ +jets and $Wc\bar{c}$ +jets, are the dominant background (56% of the total).

The signal and background distributions of relevant variables at this level are

| | | $e + \mu$ sample | e sample | μ sample |
|------------|--------------|------------------|----------------|-----------------|
| signal | no trigger | 27439 ± 150 | 11978 ± 99 | 15461 ± 113 |
| | LVL1 trigger | 24824 ± 143 | 11435 ± 97 | 13389 ± 105 |
| | LVL2 trigger | 23131 ± 138 | 10895 ± 95 | 12236 ± 100 |
| | EF trigger | 22258 ± 135 | 10303 ± 92 | 11955 ± 99 |
| background | no trigger | 15784 ± 419 | 7158 ± 298 | 8626 ± 301 |
| | LVL1 trigger | 14054 ± 400 | 6450 ± 289 | 7604 ± 282 |
| | LVL2 trigger | 12989 ± 388 | 5984 ± 280 | 7005 ± 275 |
| | EF trigger | 12413 ± 379 | 5571 ± 270 | 6842 ± 272 |

Table 5.7: *Expected number of signal and background events, normalised to $L = 1 \text{ fb}^{-1}$, after the preselection for the $e + \mu$, only e and only μ samples (no b -tagging analysis). The effect of each trigger level is also shown.*

shown in figure 5.14. The reconstructed masses of the W bosons and t -quarks (figure 5.15) have smaller tails than those obtained with the $L = 10 \text{ fb}^{-1}$ analysis. This is due to the χ^2 minimization method, which favours the jets combinations and neutrino p_z solution leading to W and t masses closer to 80.4 GeV and 175 GeV, respectively. The lost of signal/background discrimination in these variables is compensated by the $\sqrt{\chi^2}$ distribution, shown in figure 5.14(g).

Similarly to the procedure described in the previous section, a second level of analysis was adopted. For that, p.d.f. were built from the following relevant physical variables:

- the transverse momentum of the lepton;
- the transverse momentum of the two “ b -jets”;
- the $\sqrt{\chi^2}$;
- the transverse momentum of the hadronic W ;
- the hadronic and leptonic top masses and
- the cosine of the angle between the leptonic top and the leptonic “ b -jet”.

The distributions, after the preselection level, of these variables are shown in figures 5.14 and 5.15. The discriminant variable (\mathcal{L}_R) for signal and background is shown in figure 5.16.

The final event selection was done by requiring $\mathcal{L}_R > 0.1$. The number of selected events (normalized to 1 fb^{-1}) for signal and each background process after the preselection and the final selection is summarized in table 5.8. After the final selection level, the background composition is the following: 33% of $t\bar{t}$, 49% of W +jets (including $Wb\bar{b}$ and $Wc\bar{c}$) and 13% of single top. Further reduction on non $t\bar{t}$ background could be achieved by choosing an higher cut on the discriminant variable. This solution has, however, to be balanced with the corresponding decrease in

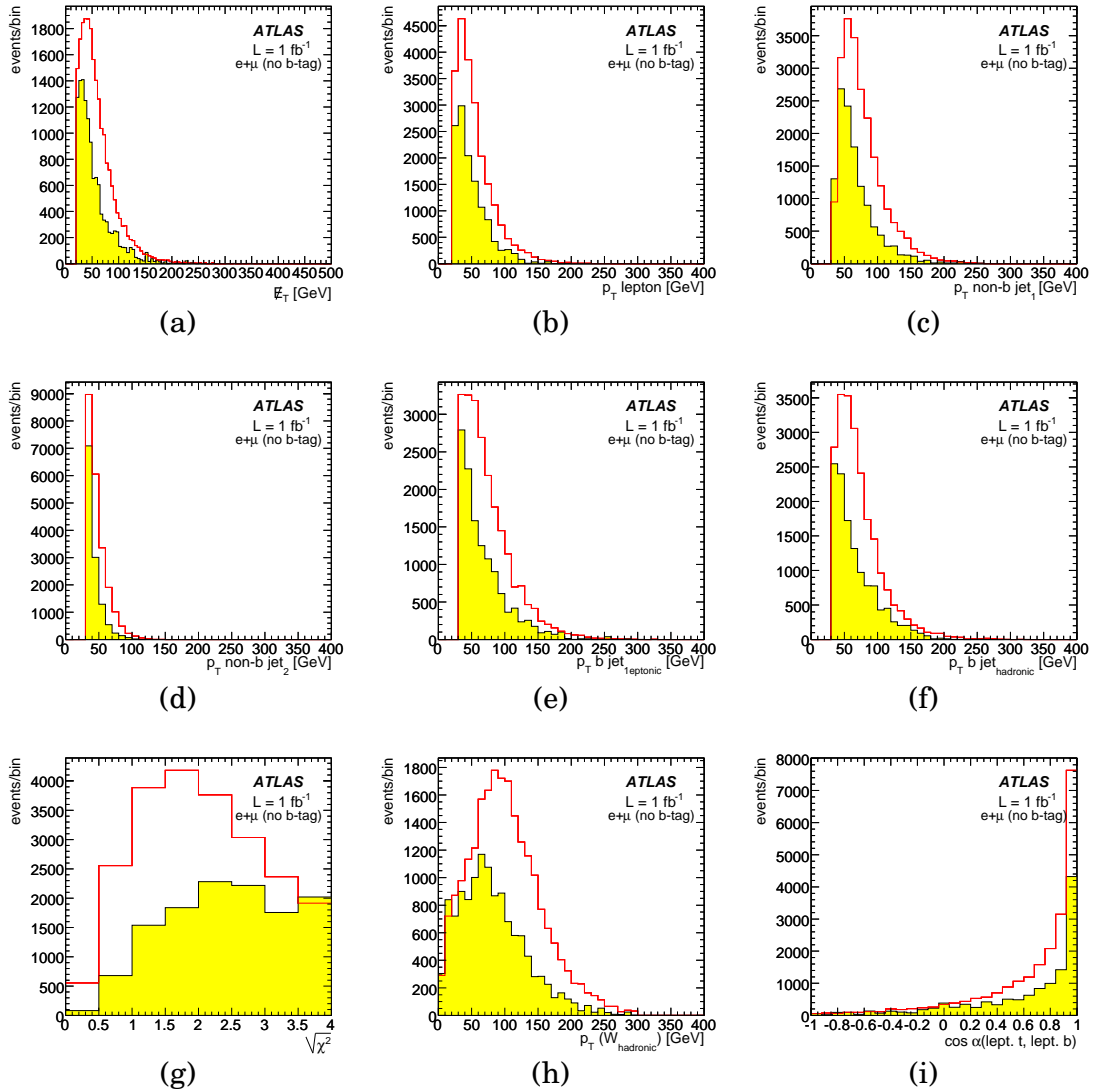


Figure 5.14: Analysis without b -tagging: distributions, after the preselection level and normalized to 1 fb^{-1} , of the signal (solid line) and background (shaded region) events which pass the trigger: (a) missing transverse energy; (b) transverse momentum of the lepton; (c-d) transverse momentum of the “non- b ” jets (i.e. the two jets used in the hadronic W reconstruction) ordered by decreasing p_T ; (e-f) transverse momentum of the “ b -jets” used to reconstruct the leptonic and hadronic top quarks; (g) $\sqrt{\chi^2}$; (h) transverse momentum of the hadronic W ; and (i) cosine of the angle between the leptonic top and the leptonic “ b -jet”.

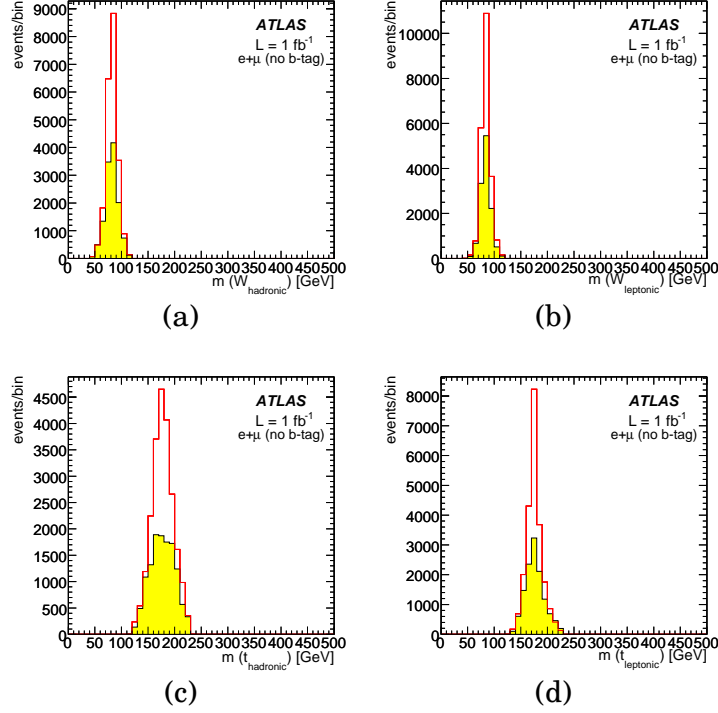


Figure 5.15: Analysis without b -tagging: distributions, after the preselection level and normalized to 1 fb^{-1} , of the signal (solid line) and background (shaded region) events which pass the trigger: reconstructed (a) hadronic and (b) leptonic W mass; (c) hadronic and (d) leptonic t mass.

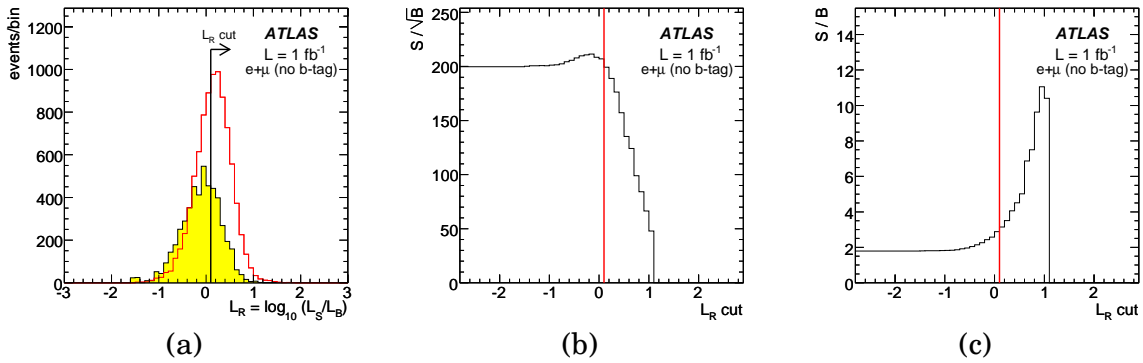


Figure 5.16: (a) Discriminant variables for the background (shaded region) and the $t\bar{t}$ signal (full line), normalised to $L = 1 \text{ fb}^{-1}$ (analysis without b -tagging). The corresponding (b) S/\sqrt{B} and (c) S/B distributions (as a function of the L_R cut) are also shown. The final event selection was done by applying the cut $\mathcal{L}_R > 0.1$.

| | | $e + \mu$ sample | e sample | μ sample |
|----------------------------|------------|------------------|-----------------|-----------------|
| signal | presel. | 22258 ± 135 | 10303 ± 92 | 11955 ± 99 |
| | final sel. | 12627 ± 103 | 5824 ± 70 | 6886 ± 76 |
| signal efficiency (%) | presel. | 9.29 ± 0.06 | 4.28 ± 0.04 | 5.02 ± 0.04 |
| | final sel. | 5.12 ± 0.04 | 2.35 ± 0.03 | 2.82 ± 0.03 |
| Z +jets | presel. | 977 ± 115 | 441 ± 59 | 536 ± 101 |
| | final sel. | 164 ± 44 | 112 ± 35 | 48 ± 30 |
| $Wb\bar{b}$ | presel. | 281 ± 33 | 143 ± 23 | 138 ± 23 |
| | final sel. | 59 ± 16 | 32 ± 13 | 22 ± 10 |
| $Wc\bar{c}$ | presel. | 1654 ± 194 | 645 ± 122 | 1009 ± 151 |
| | final sel. | 640 ± 122 | 221 ± 72 | 368 ± 92 |
| W +jets | presel. | 4961 ± 285 | 2388 ± 224 | 2572 ± 185 |
| | final sel. | 1262 ± 141 | 622 ± 121 | 637 ± 105 |
| WW, ZZ, ZW | presel. | 167 ± 33 | 80 ± 23 | 87 ± 24 |
| | final sel. | 40 ± 16 | 16 ± 10 | 17 ± 10 |
| $t\bar{t}$ (except signal) | presel. | 2924 ± 77 | 1226 ± 48 | 1698 ± 60 |
| | final sel. | 1314 ± 55 | 540 ± 34 | 785 ± 43 |
| single t | presel. | 1446 ± 56 | 645 ± 36 | 800 ± 43 |
| | final sel. | 532 ± 33 | 253 ± 22 | 267 ± 22 |
| total background | presel. | 12413 ± 379 | 5571 ± 270 | 6842 ± 272 |
| | final sel. | 4011 ± 203 | 1797 ± 152 | 2144 ± 152 |
| S/B | presel. | 1.8 ± 0.1 | 1.9 ± 0.1 | 1.7 ± 0.1 |
| | final sel. | 3.1 ± 0.2 | 3.2 ± 0.3 | 3.2 ± 0.2 |

Table 5.8: *Analysis without b -tagging: number of signal (S) and background (B) events, normalised to $L = 1 \text{ fb}^{-1}$, after the preselection and final selection levels (including the trigger selection) for the $e + \mu$, only e and only μ samples. The contribution from each background process is also shown.*

the number of selected signal events, which leads to an increase of the statistical errors on the observables. The impact of the background composition and its global normalization effects on the analysis will be studied as a systematic uncertainty (this will be discussed in section 5.2.4).

The reconstruction efficiencies for the lepton (e^\pm or μ^\pm), the neutrino and the leptonic and hadronic b , W and t are shown in table 5.9. Due to the choice of a χ^2 minimization method for the event reconstruction, these efficiencies are higher than those obtained for the $L = 10 \text{ fb}^{-1}$ analysis (table 5.3). This improvement is more significant after the final selection level.

The ΔR separation between each of the reconstructed objects and the corresponding generated particle is shown in figure 5.17. The relative differences between the momenta of the reconstructed and generated objects (as a function of the generated object momentum) are shown in figure 5.18.

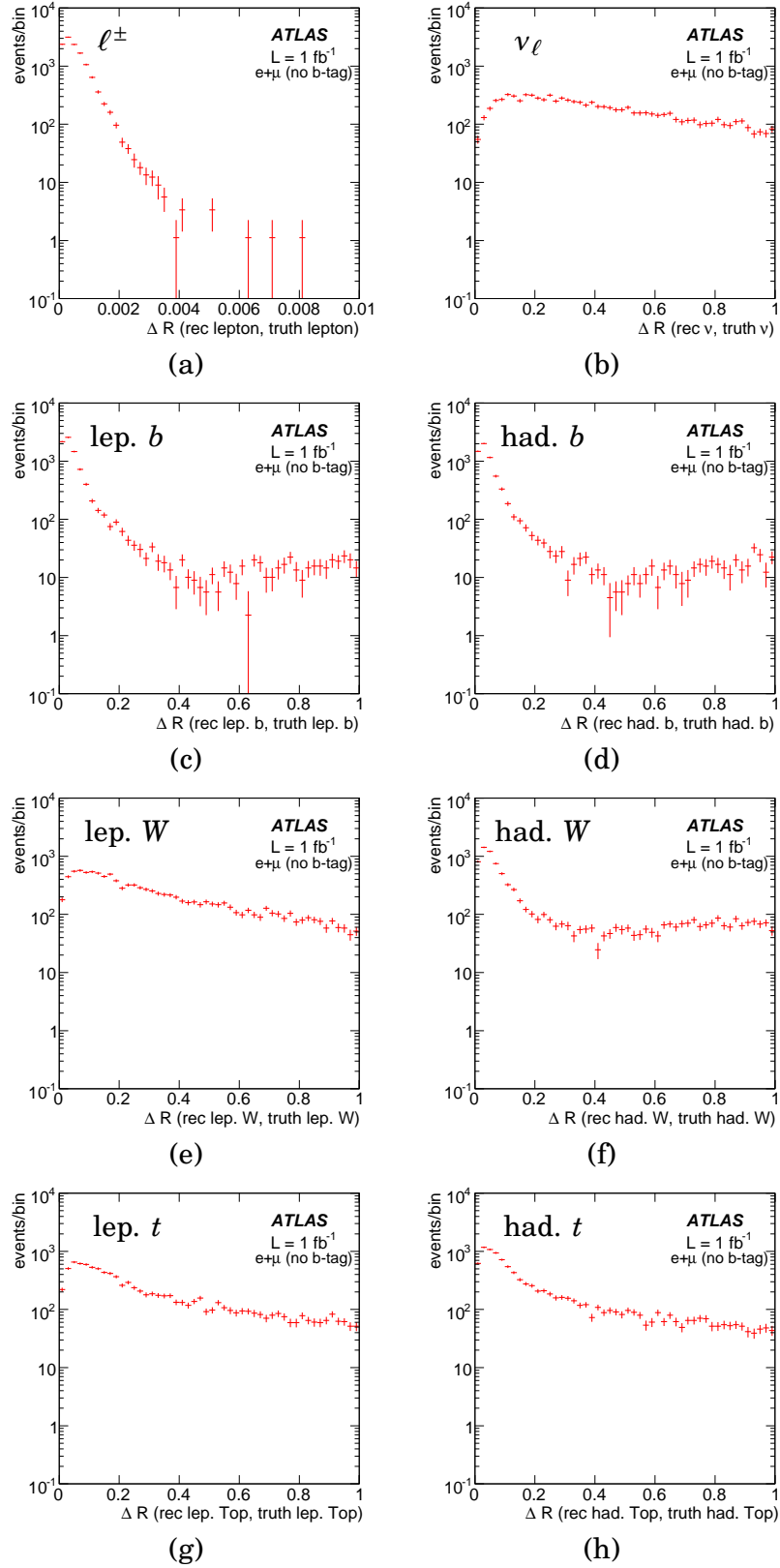


Figure 5.17: $\Delta R(\text{reconstructed, generated})$ for the full simulation analysis without b -tagging: (a) lepton (electron or muon); (b) neutrino; (c-d) leptonic and hadronic “ b -jets”; (e-f) leptonic and hadronic W -bosons; (g-h) leptonic and hadronic top quarks.

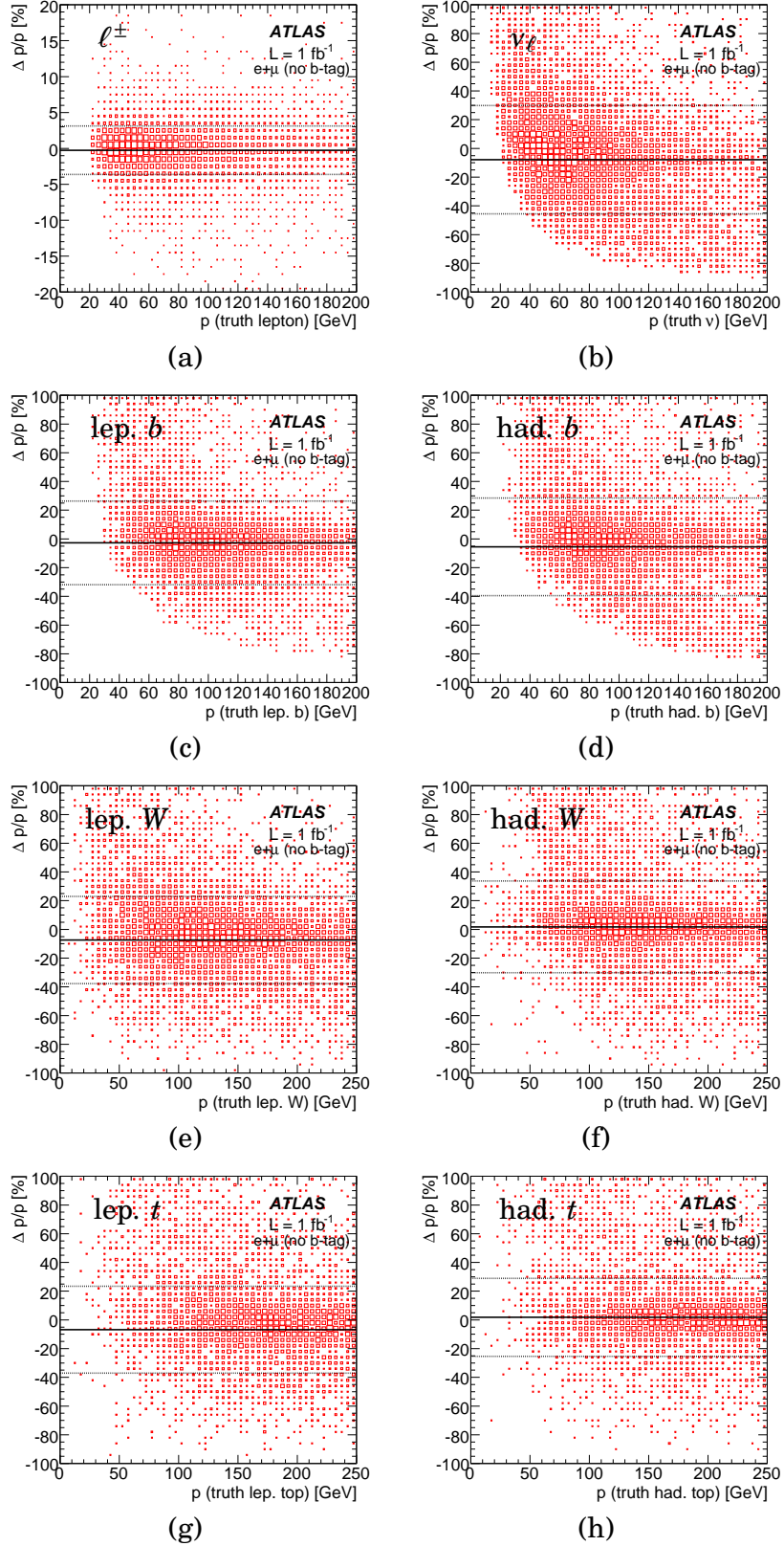


Figure 5.18: $(\Delta p)/p = (p_{\text{reconstructed}} - p_{\text{generated}})/p_{\text{generated}}$ as a function of the generated momentum for the full simulation analysis without b -tagging: (a) lepton (electron or muon); (b) neutrino; (c-d) leptonic and hadronic “ b -jets”; (e-f) leptonic and hadronic W -bosons; (g-h) leptonic and hadronic top quarks. The horizontal solid line shows the mean value of $(\Delta p)/p$ and the horizontal dashed lines show the mean value \pm the RMS (root mean square) of this distribution. The corresponding $\Delta p/p$ projections are shown in figure 5.19.

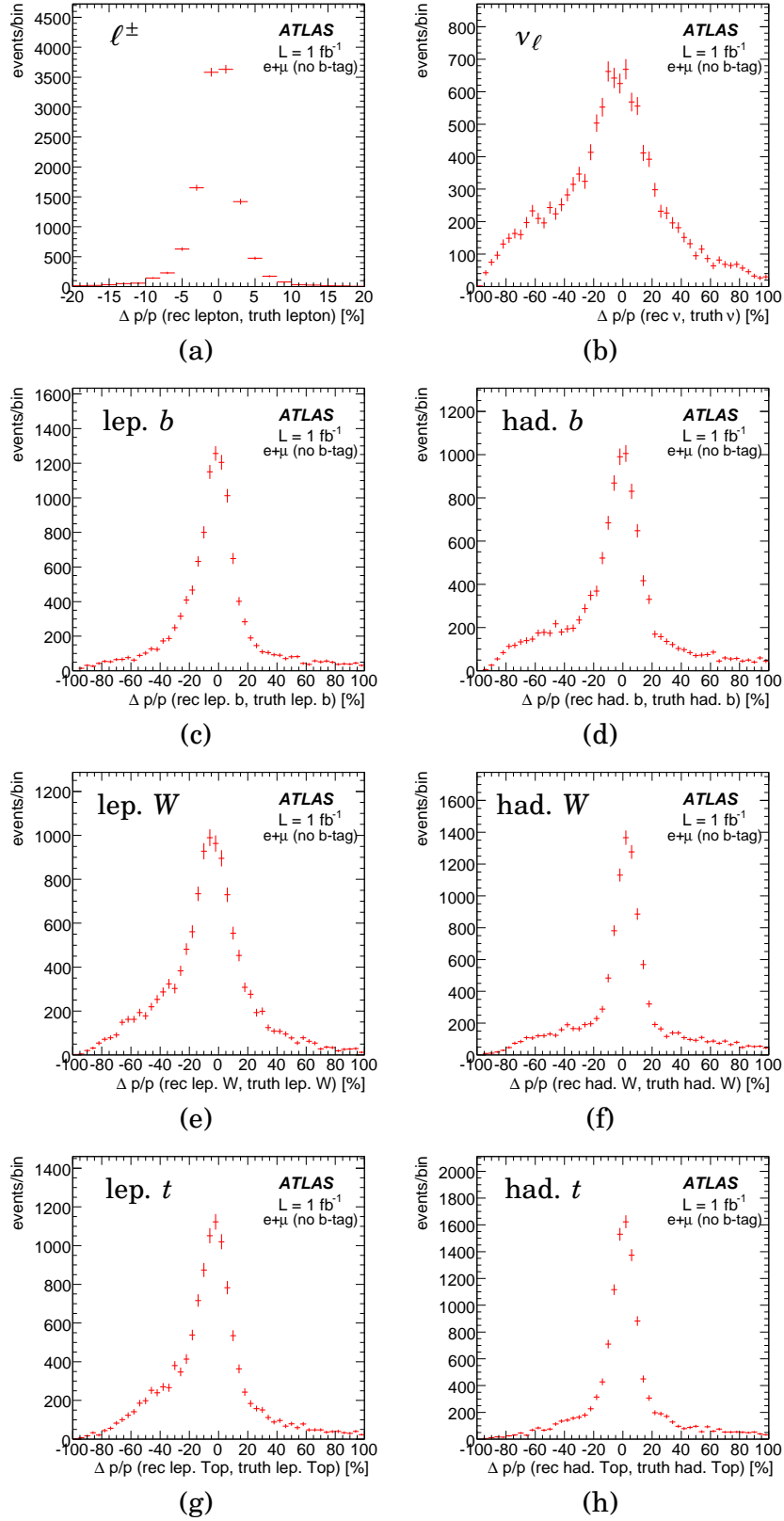


Figure 5.19: $(\Delta p)/p = (p_{\text{reconstructed}} - p_{\text{generated}})/p_{\text{generated}}$ for $L = 1 \text{ fb}^{-1}$ analysis without b -tagging: (a) lepton (electron or muon); (b) neutrino; (c-d) leptonic and hadronic b -jets; (e-f) leptonic and hadronic W -bosons; (g-h) leptonic and hadronic t quarks.

| | preselection | final selection |
|---------------------------------|----------------|-----------------|
| lepton (e^\pm or μ^\pm) | 99.6 ± 0.6 | 99.6 ± 0.8 |
| leptonic b | 53.7 ± 0.4 | 63.8 ± 0.7 |
| hadronic b | 42.3 ± 0.4 | 49.6 ± 0.6 |
| neutrino | 35.2 ± 0.4 | 38.9 ± 0.5 |
| leptonic W | 51.1 ± 0.4 | 56.7 ± 0.6 |
| hadronic W | 40.3 ± 0.4 | 49.7 ± 0.6 |
| leptonic t | 42.1 ± 0.4 | 52.7 ± 0.6 |
| hadronic t | 48.8 ± 0.4 | 60.4 ± 0.6 |

Table 5.9: *Efficiencies (in %) for each reconstructed object in the $L = 1 \text{ fb}^{-1}$ analysis without b -tagging (at the preselection and after the final selection). An object is considered to be correctly reconstructed if the corresponding generated particle is found within a cone with $\Delta R < 0.4$ from the reconstructed one.*

5.2.2 Analysis with b -tagging

Once b -tagging becomes available, additional information can be used for each jet in the event (*c.f.* figure 4.12 in section 4.3.2). In this case, an additional constraint can be included in the χ^2 evaluation: only jets with a positive b -tagging weight were considered as b -jets candidates. The resulting χ^2 distribution is shown in figure 5.20. Similarly to the procedure adopted for the analysis without b -tagging, only events with $\sqrt{\chi^2} < 4$ were preselected.

In figure 5.21, the distributions of the weights produced by the b -tagging algorithm for the “ b -jets” associated by the χ^2 minimization method to the leptonic and the hadronic top quarks are shown. In addition to the p.d.f. used for the analysis without b -tagging, these weights were also used in the discriminant variable evaluation. The resulting discriminant variable distributions for signal and background are shown in figure 5.22.

The final selection was done by requiring events with $L_R > 0.1$. The number of selected signal and background events for $L = 1 \text{ fb}^{-1}$ is summarized in table 5.10. Unlike the expectation for the analysis without b -tagging, the $t\bar{t}$ background is clearly dominant (72% of the total background expected after the final selection), while the W +jets and the single top backgrounds represent less than 14% and 15% of the total, respectively.

The improvement due to the use of b -tagging can be seen by comparing the values obtained for the object reconstruction efficiencies in the analyses with (table 5.11) and without (table 5.9) this information. As expected, reconstruction efficiencies for the top quarks rise from 53% to 65% and from 60% to 73% (leptonic and hadronic top quarks, respectively). The ΔR separation between each of the reconstructed objects and the corresponding generated particle is shown in figure 5.23. The relative differences between the momenta of the reconstructed and generated objects (as a function of the generated object momentum) are shown in figure 5.24.

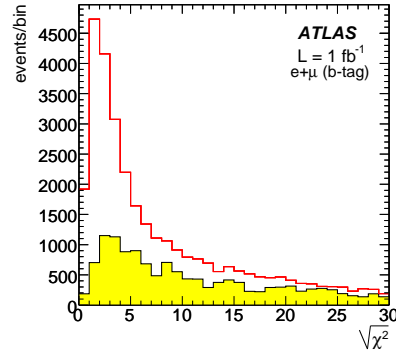


Figure 5.20: Distributions, before the $\sqrt{\chi^2} < 4$ cut and before any trigger requirements, of the $\sqrt{\chi^2}$ variable for signal (solid line) and background (shaded region), normalized to $L = 1 \text{ fb}^{-1}$ (analysis with b -tagging).

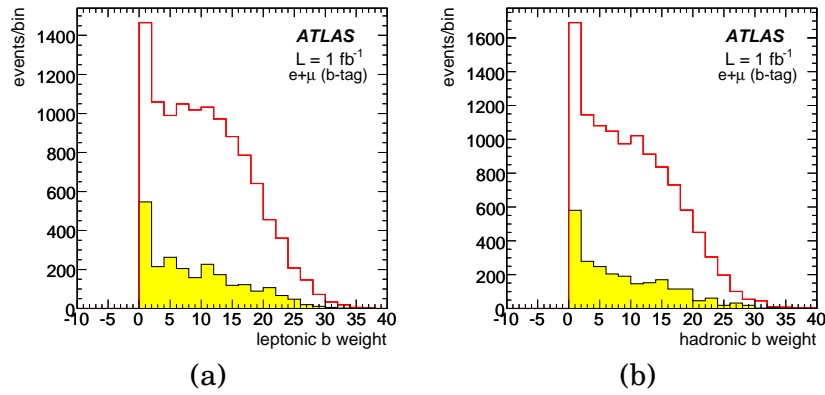


Figure 5.21: Distributions, after the preselection level and normalized to $L = 1 \text{ fb}^{-1}$, of the signal (solid line) and background (shaded area) weights provided by the b -tagging algorithm for the “ b -jets” associated by the χ^2 minimization method to (a) the leptonic and (b) the hadronic top quarks. The higher weights correspond to the more b -like jets.

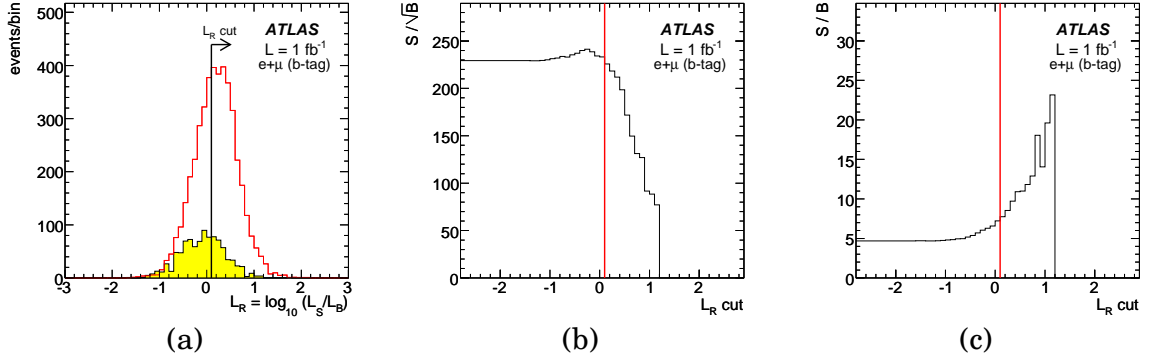


Figure 5.22: (a) Discriminant variables for the background (shaded region) and the $t\bar{t}$ signal (full line), normalised to $L = 1 \text{ fb}^{-1}$ (analysis with b-tagging). The corresponding (b) S/\sqrt{B} and (c) S/B distributions (as a function of the L_R cut) are also shown. The final event selection was done by applying the cut $\mathcal{L}_R > 0.1$.

| | | $e + \mu$ sample | e sample | μ sample |
|----------------------------|------------|------------------|-----------------|-----------------|
| signal | presel. | 11200 ± 96 | 5152 ± 66 | 6048 ± 70 |
| | final sel. | 6586 ± 74 | 3163 ± 52 | 3629 ± 55 |
| signal eff. (%) | presel. | 4.64 ± 0.04 | 2.11 ± 0.03 | 2.53 ± 0.03 |
| | final sel. | 2.67 ± 0.03 | 1.28 ± 0.02 | 1.48 ± 0.02 |
| Z +jets | presel. | 186 ± 51 | 81 ± 31 | 105 ± 46 |
| | final sel. | 0 ± 21 | 0 ± 21 | 0 ± 21 |
| $Wb\bar{b}$ | presel. | 84 ± 19 | 37 ± 14 | 47 ± 15 |
| | final sel. | 27 ± 13 | 15 ± 10 | 12 ± 10 |
| $Wc\bar{c}$ | presel. | 197 ± 68 | 111 ± 51 | 86 ± 45 |
| | final sel. | 60 ± 37 | 5 ± 27 | 30 ± 27 |
| W +jets | presel. | 181 ± 82 | 72 ± 78 | 109 ± 78 |
| | final sel. | 26 ± 73 | 0 ± 73 | 7 ± 73 |
| WW, ZZ, ZW | presel. | 2 ± 7 | 0 ± 7 | 2 ± 7 |
| | final sel. | 0 ± 7 | 0 ± 7 | 0 ± 7 |
| $t\bar{t}$ (except signal) | presel. | 1377 ± 52 | 584 ± 33 | 793 ± 41 |
| | final sel. | 613 ± 35 | 233 ± 21 | 389 ± 28 |
| single t | presel. | 359 ± 24 | 134 ± 13 | 224 ± 21 |
| | final sel. | 125 ± 14 | 66 ± 10 | 74 ± 11 |
| total background | presel. | 2385 ± 133 | 1020 ± 106 | 1365 ± 112 |
| | final sel. | 851 ± 94 | 318 ± 85 | 513 ± 88 |
| S/B | presel. | 4.7 ± 0.3 | 5.1 ± 0.5 | 4.4 ± 0.4 |
| | final sel. | 7.7 ± 0.9 | 9.9 ± 2.7 | 7.1 ± 1.2 |

Table 5.10: Analysis with b-tagging: number of signal and background events, normalised to $L = 1 \text{ fb}^{-1}$, after the preselection and final selection levels (including the trigger selection) for the $e + \mu$, only e and only μ samples. The contribution from each background process is also shown.

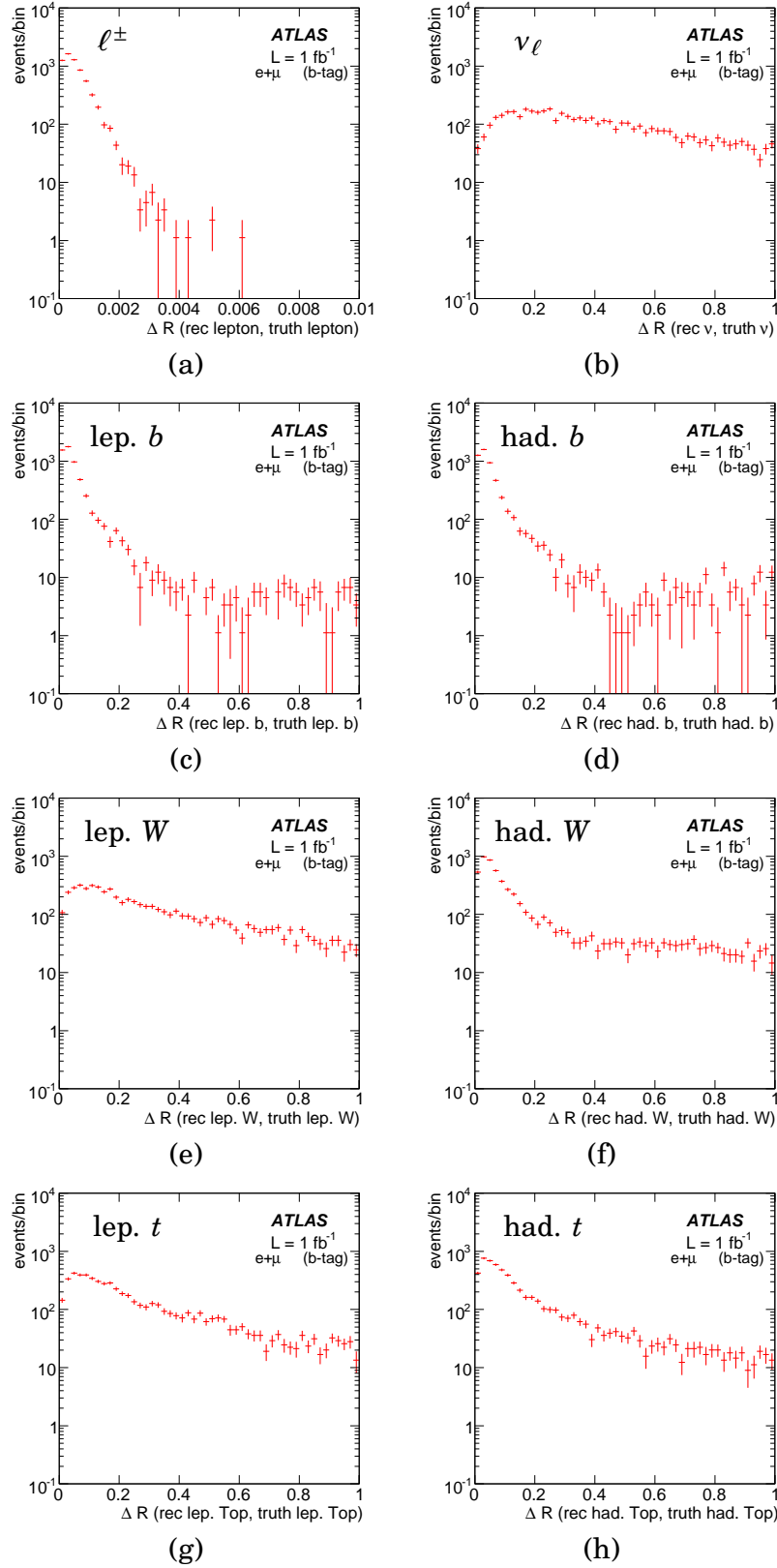


Figure 5.23: ΔR (reconstructed,generated) for the full simulation analysis with b -tagging: (a) lepton (electron or muon); (b) neutrino; (c-d) leptonic and hadronic “ b -jets”; (e-f) leptonic and hadronic W -bosons; (g-h) leptonic and hadronic top quarks.

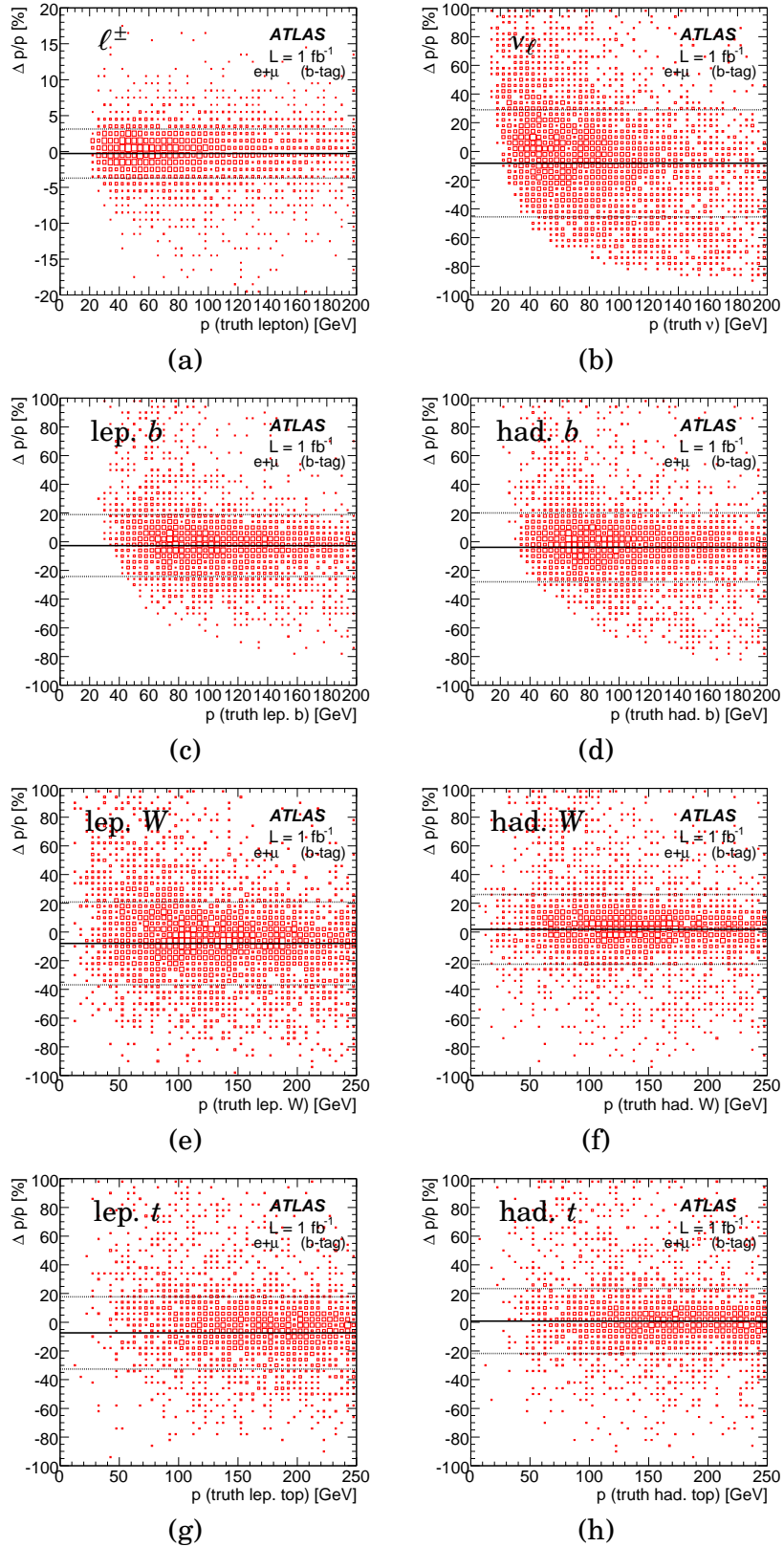


Figure 5.24: $(\Delta p)/p = (p_{\text{reconstructed}} - p_{\text{generated}})/p_{\text{generated}}$ as a function of the generated momentum for the full simulation analysis with b -tagging: (a) lepton (electron or muon); (b) neutrino; (c-d) leptonic and hadronic “ b -jets”; (e-f) leptonic and hadronic W -bosons; (g-h) leptonic and hadronic top quarks. The horizontal solid line shows the mean value of $(\Delta p)/p$ and the horizontal dashed lines show the mean value \pm the RMS (root mean square) of this distribution. The corresponding $\Delta p/p$ projections are shown in figure 5.25.

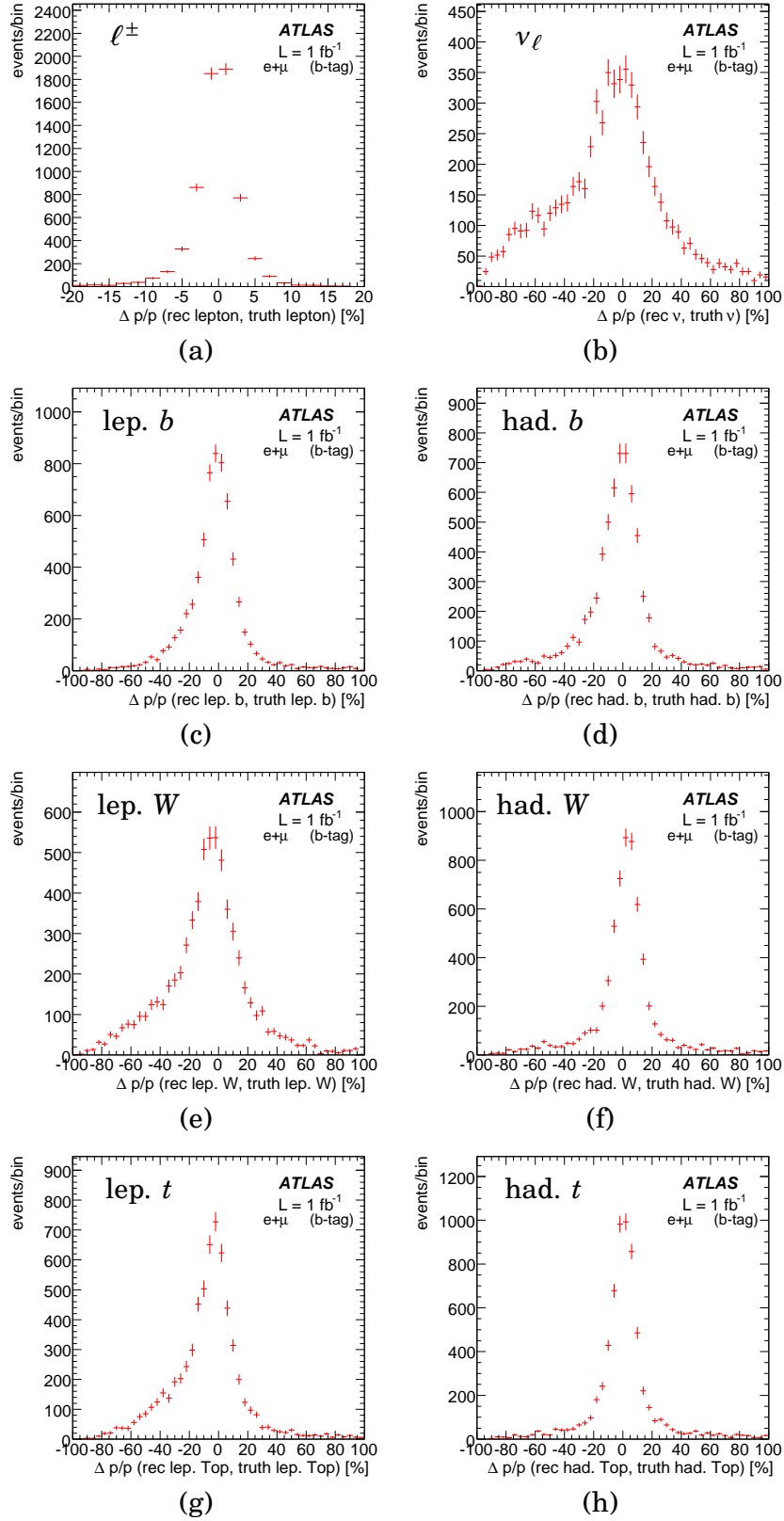


Figure 5.25: $(\Delta p)/p = (p_{\text{reconstructed}} - p_{\text{generated}})/p_{\text{generated}}$ for $L = 1 \text{ fb}^{-1}$ analysis with b -tagging: (a) lepton (electron or muon); (b) neutrino; (c-d) leptonic and hadronic b -jets; (e-f) leptonic and hadronic W -bosons; (g-h) leptonic and hadronic t quarks.

| | preselection | final selection |
|---------------------------------|----------------|-----------------|
| lepton (e^\pm or μ^\pm) | 99.6 ± 0.9 | 99.6 ± 1.1 |
| leptonic b | 74.1 ± 0.7 | 83.7 ± 1.0 |
| hadronic b | 67.7 ± 0.7 | 76.8 ± 1.0 |
| neutrino | 36.8 ± 0.5 | 39.8 ± 0.7 |
| leptonic W | 53.0 ± 0.6 | 59.1 ± 0.9 |
| hadronic W | 58.5 ± 0.7 | 70.2 ± 0.9 |
| leptonic t | 53.3 ± 0.6 | 64.5 ± 0.9 |
| hadronic t | 60.1 ± 0.7 | 72.9 ± 1.0 |

Table 5.11: *Efficiencies (in %) for each reconstructed object in the $L = 1 \text{ fb}^{-1}$ analysis with b -tagging (after the preselection and final selection levels). An object is considered to be correctly reconstructed if the corresponding generated particle is found within a cone with $\Delta R < 0.4$ from the reconstructed one.*

5.2.3 W polarization and angular asymmetries

The reconstructed $\cos\theta_\ell^*$ distributions (for the analyses with and without the use of b -tagging) are shown in figure 5.26. The background subtraction and the correction for the selection and detector effects was done in the same way as for the $L = 10 \text{ fb}^{-1}$ analysis (section 5.1). Two sets of signal and background event samples were used: one “experimental” set, which simulates a possible experimental result, and one “reference” set, which is used to parametrise the effects mentioned, and correct the previous sample. After subtracting the background, the full “experimental” distribution was multiplied by a correction function (figure 5.27). In order to avoid non-physical fluctuations due to the limited number of MC events, a smoothing procedure was applied to the obtained correction function, as shown in figure 5.27. The corrected $\cos\theta_\ell^*$ distributions are shown in figure 5.28.

As the asymmetry measurements are less biased by the extreme values of the angular distributions, these observables are particularly interesting for the low statistics analyses. Moreover, it should be noticed that, as explained in section 5.1, the $\cos\theta_\ell^*$ bins near $+1$ have a significant impact on the measurement of the F_R helicity fraction (and thus on the ρ_R helicity ratio). Due to the statistics expected for $L = 1 \text{ fb}^{-1}$, the correction function in the bin near -1 may have a large value (*c.f.* figure 5.27) and therefore it is expected to have a large statistical uncertainty. For these two reasons, the helicity fractions and ratios were obtained from a fit to the corrected $\cos\theta_\ell^*$ distribution in the range $[-0.9, +1]$. An example of the $\cos\theta_\ell^*$ fit is shown in figure 5.28 for the analyses without and with b -tagging.

The obtained values (and corresponding statistical errors) for the helicity fractions, helicity ratios and angular asymmetries ($L = 1 \text{ fb}^{-1}$) are shown in table 5.12. Although the selected number events is higher for the analyses without b -tagging, the statistical errors on the W helicity fractions and ratios are larger than those obtained for the analysis with b -tagging. This is explained by a larger background contamination, which increases the statistical uncertainty in the background sub-

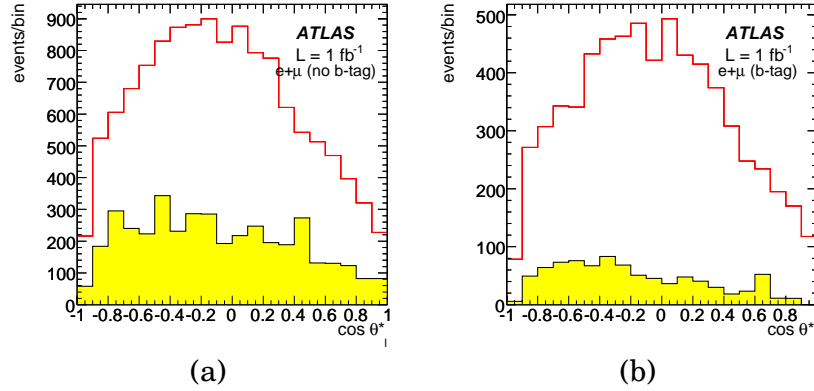


Figure 5.26: Reconstructed $\cos\theta_\ell^*$ distributions, after the final selection and normalized to $L = 1 \text{ fb}^{-1}$ for: (a) the analysis without b -tagging and (b) the analysis with b -tagging. The solid line corresponds to the signal and the shaded region to the background.

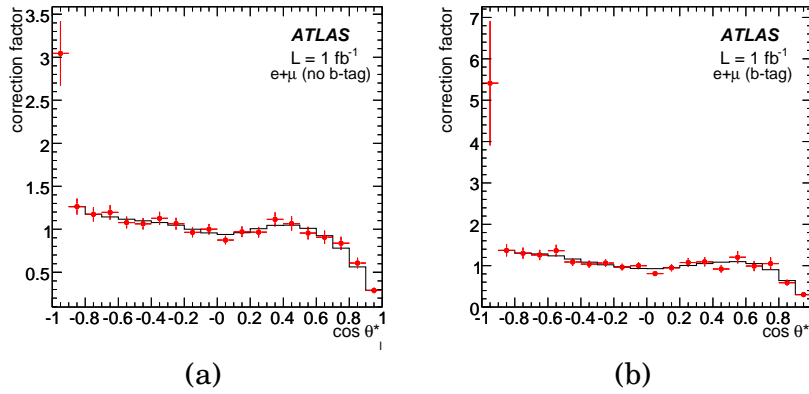


Figure 5.27: Correction functions for: (a) the analysis without b -tagging and (b) the analysis with b -tagging. The applied smooth is also shown (solid line).

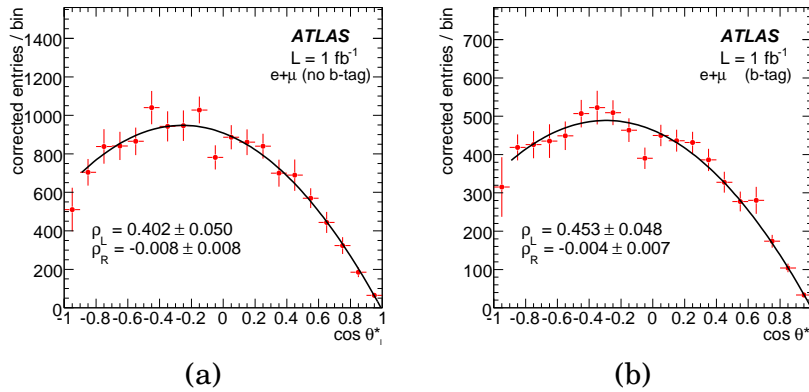


Figure 5.28: Corrected $\cos\theta_\ell^*$ distributions for: (a) the analysis without b -tagging and (b) the analysis with b -tagging. The fit used to extract the W helicity ratios (ρ_L and ρ_R) are also shown.

traction, due to the limited statistics of the MC samples.

| | without b -tag | with b -tag |
|-----------------|--------------------|--------------------|
| F_0 | 0.717 ± 0.022 | 0.690 ± 0.019 |
| F_L | 0.289 ± 0.021 | 0.312 ± 0.019 |
| F_R | -0.006 ± 0.006 | -0.003 ± 0.005 |
| ρ_L | 0.402 ± 0.050 | 0.453 ± 0.048 |
| ρ_R | -0.008 ± 0.008 | -0.004 ± 0.007 |
| A_{FB} | -0.220 ± 0.025 | -0.229 ± 0.026 |
| A_+ | 0.560 ± 0.024 | 0.542 ± 0.028 |
| A_- | -0.845 ± 0.012 | -0.830 ± 0.014 |

Table 5.12: *Expected values and corresponding statistical errors for the helicity fractions, helicity ratios and angular asymmetries. The results for an integrated luminosity of 1 fb^{-1} (analyses with and without b -tagging) are shown.*

5.2.4 Systematic uncertainties

Even for $L = 1 \text{ fb}^{-1}$, systematic errors are expected to play an important role in the measurement of the angular distribution and asymmetries. Although the available Monte Carlo full simulation samples do not allow a precise determination of the systematic uncertainties (due to the relatively small statistics of these samples), a study of relevant uncertainties was performed for the $L = 1 \text{ fb}^{-1}$ analysis. It should be stressed that, unlikely the studies done for $L = 10 \text{ fb}^{-1}$ with the fast simulation, the determination of the systematic uncertainties is contaminated by the statistical errors. Therefore, it can be considered that the systematic error evaluation for the full simulation analyses was done in a conservative way.

The following systematic uncertainties were considered in the present study:

1. *Jet energy scale:* The value of the jet energy scale was changed from -15 to +15%, and the values obtained for the observables are fitted with a linear function (see appendix B). The systematic uncertainty was considered as the effect of a variation of 5% in the jet energy scale.
2. *Luminosity:* The value of the luminosity was changed from -20 to +20%, and the values obtained for the observables are fitted with a linear function (see appendix B). The systematic uncertainty is considered as the effect of a variation of 20% in the luminosity.
3. *Top mass dependence:* Samples corresponding to top masses of 160, 170, 175 and 190 GeV were simulated, and the influence of m_t on the values obtained for the observables was estimated (see appendix B). The systematic uncertainty used here was obtained from a linear fit of the values found, corresponding to a top mass uncertainty of 2 GeV.

4. *Background normalization:* The cross-sections for each background process were changed (12% for $t\bar{t}$, 3% for Wt channel of single top, 6% for s -channel of single top, 4% for t -channel of single top, 50% for W +jets and 15% for the remaining background processes [108]⁴). This change was done for each process at a time. The systematic uncertainty was the quadratic sum of all the variations.
5. *ISR and FSR:* Their effect was studied by changing the different switches of the Monte Carlo generators which control the ISR and FSR, as explained in section 4.3.1. The maximum change in the value of the observables was considered as the systematic uncertainty.
6. *Monte Carlo generator:* the results obtained with the MC@NLO and AcerMC generators were compared. The difference between the obtained observables was considered as a systematic uncertainty associated to the modeling of the Monte Carlo.
7. *Pile-up:* The effect of pile-up events was studied by comparing the values of the observables obtained with and without adding pile-up events (conservatively, 4.6 collisions per bunch-crossing were considered).

Similarly to the procedure adopted for the $L = 10 \text{ fb}^{-1}$ analysis, only the simulation used as the “experimental” set (which fakes the data) was changed for each systematic source of uncertainty. The correction function and the MC sample used to perform the background subtraction were kept unchanged. This method allows to estimate the systematic uncertainty caused by discrepancy between the data and the Monte Carlo simulation. Such impact on the observables is summarized in tables 5.13 and 5.14.

As in the current method a background subtraction is performed based on Monte Carlo simulation, the luminosity value is used in the background estimation. Once the cross-sections for known backgrounds are measured with experimental data, a data-driven normalization will be possible and the luminosity systematic error should be eliminated. Moreover, with data it will be possible to compare the discriminant variable distributions for signal obtained from data and MC. This comparison will allow to estimate any systematic errors caused by an inaccurate description of data by the Monte Carlo simulation. Systematic uncertainties associated with the lepton identification and trigger (either affecting the global efficiency or the lepton p_T dependence) are expected to be small and have not been considered in the present study.

The effect of the b -tagging weight on the χ^2 minimization reconstruction method (in the analysis with b -tagging) was evaluated by changing the requirement for a jet to be a b candidate from $\text{weight}_{b\text{-tag}} > 0$ to $\text{weight}_{b\text{-tag}} > 2$. This effect was found to be smaller than the statistical error for all the considered observables.

⁴ The changes in the background cross-sections were done according to the corresponding theoretical error, except for the W +jets process, where a more conservative approach was chosen.

| | F_0 | F_L | F_R | ρ_L | ρ_R | A_{FB} | A_+ | A_- |
|------------------|-------|-------|-------|----------|----------|-----------------|-------|-------|
| jet energy scale | 0.014 | 0.012 | 0.003 | 0.023 | 0.003 | 0.004 | 0.006 | 0.002 |
| luminosity | 0.009 | 0.007 | 0.002 | 0.015 | 0.002 | 0.006 | 0.005 | 0.001 |
| top mass | 0.009 | 0.010 | 0.001 | 0.019 | 0.002 | 0.009 | 0.006 | 0.004 |
| background | 0.005 | 0.004 | 0.002 | 0.009 | 0.002 | 0.005 | 0.003 | 0.002 |
| ISR+FSR | 0.064 | 0.060 | 0.006 | 0.132 | 0.009 | 0.044 | 0.046 | 0.011 |
| MC generator | 0.087 | 0.079 | 0.009 | 0.181 | 0.013 | 0.039 | 0.042 | 0.001 |
| pile-up | 0.068 | 0.064 | 0.003 | 0.141 | 0.004 | 0.053 | 0.039 | 0.017 |
| total | 0.129 | 0.119 | 0.012 | 0.267 | 0.017 | 0.080 | 0.074 | 0.021 |

Table 5.13: Sources of systematic error in the determination of the helicity fractions, helicity ratios and angular asymmetries ($L = 1 \text{ fb}^{-1}$ full simulation analysis without b -tagging).

| | F_0 | F_L | F_R | ρ_L | ρ_R | A_{FB} | A_+ | A_- |
|------------------|-------|-------|-------|----------|----------|-----------------|-------|-------|
| jet energy scale | 0.019 | 0.018 | 0.001 | 0.038 | 0.001 | 0.010 | 0.004 | 0.002 |
| luminosity | 0.003 | 0.003 | 0.000 | 0.007 | 0.000 | 0.006 | 0.005 | 0.001 |
| top mass | 0.013 | 0.015 | 0.002 | 0.026 | 0.003 | 0.013 | 0.008 | 0.006 |
| background | 0.002 | 0.002 | 0.000 | 0.005 | 0.000 | 0.003 | 0.002 | 0.004 |
| ISR+FSR | 0.025 | 0.026 | 0.004 | 0.052 | 0.006 | 0.024 | 0.028 | 0.015 |
| MC generator | 0.009 | 0.004 | 0.005 | 0.012 | 0.008 | 0.009 | 0.011 | 0.000 |
| pile-up | 0.081 | 0.076 | 0.005 | 0.146 | 0.006 | 0.012 | 0.041 | 0.022 |
| total | 0.089 | 0.084 | 0.008 | 0.163 | 0.012 | 0.033 | 0.052 | 0.027 |

Table 5.14: Sources of systematic error in the determination of the helicity fractions, helicity ratios and angular asymmetries ($L = 1 \text{ fb}^{-1}$ full simulation analysis with b -tagging).

The results obtained for the different observables for the analyses with and without b -tagging are summarized in tables 5.15 and 5.16, respectively.

| | | | | | | | |
|-----------------|--------|-------|-------|--------|-------|-------|---------|
| F_0 | 0.717 | \pm | 0.022 | (stat) | \pm | 0.129 | (syst.) |
| F_L | 0.289 | \pm | 0.021 | (stat) | \pm | 0.119 | (syst.) |
| F_R | -0.006 | \pm | 0.006 | (stat) | \pm | 0.012 | (syst.) |
| ρ_L | 0.402 | \pm | 0.050 | (stat) | \pm | 0.267 | (syst.) |
| ρ_R | -0.008 | \pm | 0.008 | (stat) | \pm | 0.017 | (syst.) |
| A_{FB} | -0.220 | \pm | 0.025 | (stat) | \pm | 0.080 | (syst.) |
| A_+ | 0.560 | \pm | 0.024 | (stat) | \pm | 0.074 | (syst.) |
| A_- | -0.845 | \pm | 0.012 | (stat) | \pm | 0.021 | (syst.) |

Table 5.15: *Summary of the results obtained from the simulation for the observables studied, including statistical and systematic uncertainties (full simulation analysis without b -tagging for $L = 1 \text{ fb}^{-1}$).*

| | | | | | | | |
|-----------------|--------|-------|-------|--------|-------|-------|---------|
| F_0 | 0.690 | \pm | 0.019 | (stat) | \pm | 0.089 | (syst.) |
| F_L | 0.312 | \pm | 0.019 | (stat) | \pm | 0.084 | (syst.) |
| F_R | -0.003 | \pm | 0.005 | (stat) | \pm | 0.008 | (syst.) |
| ρ_L | 0.453 | \pm | 0.048 | (stat) | \pm | 0.163 | (syst.) |
| ρ_R | -0.004 | \pm | 0.007 | (stat) | \pm | 0.012 | (syst.) |
| A_{FB} | -0.229 | \pm | 0.026 | (stat) | \pm | 0.033 | (syst.) |
| A_+ | 0.542 | \pm | 0.028 | (stat) | \pm | 0.052 | (syst.) |
| A_- | -0.830 | \pm | 0.014 | (stat) | \pm | 0.027 | (syst.) |

Table 5.16: *Summary of the results obtained from the simulation for the observables studied, including statistical and systematic uncertainties (full simulation analysis with b -tagging for $L = 1 \text{ fb}^{-1}$).*

Chapter 6

EXPECTED CONSTRAINTS ON THE Wtb ANOMALOUS COUPLINGS

IN THIS CHAPTER the expected ATLAS sensitivity to Wtb anomalous couplings is discussed. For this, the results obtained in chapter 5 were used. The most sensitive observables (A_{\pm} and $\rho_{R,L}$) were used to derive the expected 95% confidence level (CL) limits on the anomalous couplings (section 6.1). This was done using the program TopFit [57], in which the parametric dependence of the studied observables on V_R , g_L and g_R is implemented. A brief discussion on additional observables, which could be used to improve the limits is done in section 6.2.

6.1 Expected limits at ATLAS

The 1σ limits on a coupling ($x = V_R, g_L, g_R$) can be naively derived from the measurement of some observable O , by finding the values of x for which O deviates 1σ from its central value.¹ Nevertheless, due to the quadratic dependence of the observables on V_R and g_L near the SM point $V_R = g_L = 0$, this procedure leads to overcoverage of the obtained confidence intervals [57], because their p.d.f.s are not Gaussian, even if the p.d.f. of the observable O is so.

In order to obtain the limits on an anomalous coupling x , given by the measurement of an observable O , the p.d.f. of x was determined numerically, using the acceptance-rejection method [129]:

- (1) a random value with uniform probability, x_i , was generated within a suitable interval;

¹ This intersection method is followed in the previous ATLAS studies [128, 126]. For an observable O and a coupling x , the intersection of the plot of $O(x)$ with the two horizontal lines $O = O_{\text{exp}} \pm \sigma(O_{\text{exp}})$, which correspond to the 1σ variation of O , gives the pretended 1σ interval on x .

- (2) the probability of $O(x_i)$, given by the p.d.f. of O was determined;
- (3) an independent random number (r_i) with uniform probability was generated;
- (4) the value x_i is accepted if the probability of $O(x_i)$ is larger than r_i .

The resulting set of values $\{x_i\}$ is distributed according to the p.d.f. of x given by the measurement of O . The determination of a central interval with a given CL γ is done numerically by requiring that:

- (a) it contains a fraction γ of the total number of values $\{x_i\}$;
- (b) it is central, i.e. a fraction $(1 - \gamma)/2$ of the values generated are on each side of the interval.

For $x = g_R$ this method gives results very similar to the intersection method [126, 128], whereas for V_R and g_L the confidence intervals were found to be 20% and 30% smaller, respectively.

The 1σ limits derived from the measurement of each observable (fast simulation analysis for $L = 10 \text{ fb}^{-1}$) are collected in table 6.1, assuming that only one coupling is different from zero at a time. The best limits on V_R and g_L are obtained from the measurement of ρ_R and the best limits on g_R are provided by A_+ . This is due to the smaller (systematic and statistical) uncertainties of these new observables and to their stronger dependence on the anomalous couplings.

| | V_R ($g_L = g_R = 0$) | g_L ($V_R = g_R = 0$) | g_R ($V_R = g_L = 0$) |
|-----------------|------------------------------|------------------------------|------------------------------|
| F_0 | — | $[-0.133, 0.102]$ | $[-0.032, 0.022]$ |
| F_L | $[-0.196, 0.186]$ | $[-0.167, 0.136]$ | $[-0.029, 0.021]$ |
| F_R | $[-0.037, 0.107]$ | $[-0.049, 0.017]$ | — |
| ρ_L | $[-0.254, 0.206]$ | — | $[-0.026, 0.023]$ |
| ρ_R | $[-0.028, 0.099]$ | $[-0.046, 0.0129]$ | — |
| A_{FB} | $[-0.118, 0.148]$ | $[-0.090, 0.0585]$ | $[-0.027, 0.023]$ |
| A_+ | $[-0.140, 0.146]$ | $[-0.112, 0.0819]$ | $[-0.021, 0.016]$ |
| A_- | $[-0.066, 0.120]$ | $[-0.062, 0.0299]$ | $[-0.017, 0.028]$ |

Table 6.1: *Expected 1σ limits on anomalous couplings obtained from the different observables (expectation for $L = 10 \text{ fb}^{-1}$). Only one anomalous coupling was allowed to be nonzero at a time. Dashes are shown where no significant sensitivity was found.*

These limits can be further improved by combining the measurements of the four most sensitive observables $\rho_{R,L}$ and A_{\pm} . In this case, the correlations among them have to be considered. It should be pointed out that the correlations among A_{\pm} , $\rho_{R,L}$ depend on the method followed to extract these observables. The angular asymmetries A_{\pm} were obtained by a simple event counting above and below a specific value of $z = \cos\theta_{\ell}^*$, while $\rho_{R,L}$ were obtained from a fit to the $\cos\theta_{\ell}^*$ distribution, divided in 20 bins.

| | A_+ | A_- | ρ_L | ρ_R |
|----------|--------|--------|----------|----------|
| A_+ | 1 | 0.159 | -0.822 | -0.123 |
| A_- | 0.159 | 1 | -0.086 | 0.569 |
| ρ_L | -0.822 | -0.086 | 1 | 0.396 |
| ρ_R | -0.123 | 0.569 | 0.396 | 1 |

Table 6.2: Correlation matrix for A_{\pm} , $\rho_{R,L}$ ($L = 10 \text{ fb}^{-1}$ analysis).

| | A_+ | A_- | ρ_L | ρ_R |
|----------|--------|--------|----------|----------|
| A_+ | 1 | 0.159 | -0.731 | -0.141 |
| A_- | 0.159 | 1 | -0.103 | 0.549 |
| ρ_L | -0.731 | -0.103 | 1 | 0.419 |
| ρ_R | -0.141 | 0.549 | 0.419 | 1 |

Table 6.3: Correlation matrix for A_{\pm} , $\rho_{R,L}$ ($L = 1 \text{ fb}^{-1}$ analyses).

The correlations among these observables were derived as follows. A set of Monte Carlo pseudoexperiments, in which each element of the set is a binned $\cos\theta_\ell^*$ distribution, was used. For each pseudoexperiment, the number of events in each $\cos\theta_\ell^*$ bin was obtained randomly using a Gaussian distribution centered at the expected SM value. The average of the ten independent products of observables ($\langle A_+^2 \rangle$, $\langle A_+ A_- \rangle$, $\langle A_+ \rho_L \rangle$, etc.) was calculated and, from this, the correlation matrix was obtained [130]. The resulting correlation matrix is shown in tables 6.2 and 6.3, for the $L = 10 \text{ fb}^{-1}$ and $L = 1 \text{ fb}^{-1}$ analyses, respectively. The difference in the correlations obtained for the $L = 10 \text{ fb}^{-1}$ and $L = 1 \text{ fb}^{-1}$ analyses is explained by the experimental method used to obtain the $\rho_{R,L}$ observables: in the first case the fit to the $\cos\theta_\ell^*$ was done in the range $[-1,1]$, while in the second case the range was $[-0.9,1]$ (see chapter 5). The correlation between A_+ and A_- is the same in both cases because the method used to evaluate the angular asymmetries for both analyses was the same. The obtained correlations among A_{\pm} , $\rho_{R,L}$ are not affected by systematic uncertainties, as long as these do not significantly distort the shape of the $\cos\theta_\ell^*$ distribution with respect to the expected SM one.

In table 6.4 the expected 1σ limits on the Wtb anomalous couplings, obtained from the $\rho_{L,R}$ and A_{\pm} observables are shown for luminosities of 1 fb^{-1} and 10 fb^{-1} . In these limits only one anomalous coupling was allowed to be nonzero at a time.

When the four observables A_{\pm} and $\rho_{R,L}$ are combined, the assumption that only one coupling is nonzero at a time can be relaxed. However, if V_R and g_L are simultaneously allowed to be arbitrary, the limits are very loose and correlated, because for fine-tuned values of these couplings their effects on helicity fractions cancel to a large extent. In this way, values around 0.4 for V_R and g_L are possible yielding minimal deviations on the observables studied. Therefore, in the combined limits, which are presented in table 6.5 for $L = 10 \text{ fb}^{-1}$, either V_R or g_L were required to be zero. Simultaneous limits on V_R , g_L require the use of additional observables

| | 1 fb^{-1} (no b -tag) | 1 fb^{-1} (b -tag) | 10 fb^{-1} |
|-------|-----------------------------------|---------------------------------|----------------------|
| V_R | $[-0.091, 0.155]$ | $[-0.062, 0.128]$ | $[-0.020, 0.091]$ |
| g_L | $[-0.072, 0.040]$ | $[-0.060, 0.028]$ | $[-0.041, 0.009]$ |
| g_R | $[-0.113, 0.107]$ | $[-0.118, 0.085]$ | $[-0.011, 0.017]$ |

Table 6.4: *Expected 1σ limits on the Wtb anomalous couplings for luminosities of 1 fb^{-1} (with and without b -tag) and 10 fb^{-1} . These limits were obtained from the $\rho_{L,R}$ and A_{\pm} observables and only one anomalous coupling was allowed to be nonzero at a time.*

| V_R | g_L | g_R |
|-------------------|-------------------|-------------------|
| \times | $[-0.041, 0.009]$ | $[-0.011, 0.018]$ |
| $[-0.020, 0.090]$ | \times | $[-0.013, 0.016]$ |

Table 6.5: *Expected 1σ limits on the anomalous couplings, obtained from the combined measurement of A_{\pm} , $\rho_{R,L}$ ($L = 10 \text{ fb}^{-1}$). In each case, the couplings fixed to zero are denoted by a cross.*

beyond the ones directly related to W helicity fractions, which are beyond the scope of the present thesis.

In order to make a comparison with the previous published results, 2σ limits on the anomalous couplings (when only one of them is nonzero) were also obtained:

$$\begin{aligned}
V_R(2\sigma) & \quad [-0.057, 0.128] \quad (g_L = g_R = 0), \\
g_L(2\sigma) & \quad [-0.058, 0.026] \quad (V_R = g_R = 0), \\
g_R(2\sigma) & \quad [-0.026, 0.031] \quad (V_R = g_L = 0).
\end{aligned} \tag{6.1}$$

A significant improvement (by factors of 3.2, 3.1 and 1.4, respectively) is obtained with respect to the results presented in Ref [126], which include the dilepton channel. This improvement is mainly due to:

- (i) The better sensitivity obtained for the W helicity ratios, especially for F_0 . This leads to a moderate improvement for g_L and V_R (with limits about 1.13 times smaller) and to a more significant improvement for g_R (a factor of 1.34).
- (ii) The combination of the $\rho_{R,L}$ and A_{\pm} observables.
- (iii) The different statistical method used to derive the limits. For V_R and g_L , the Monte Carlo method used to obtain the true 1σ intervals also reduces their size by 20%–30%, as explained above.

A similar procedure was used to obtain the 68.3% CL regions on the anomalous couplings:

1. Values for two of the anomalous couplings (*e.g.* g_L and g_R) were randomly generated with an uniform distribution. The third anomalous coupling (*e.g.* V_R) was fixed to zero.
2. The corresponding values for the observables were evaluated (using the equations 2.6, presented in chapter 2).
3. The vector d was evaluated, for each point, with the differences between the measured and the generated value for each observable:

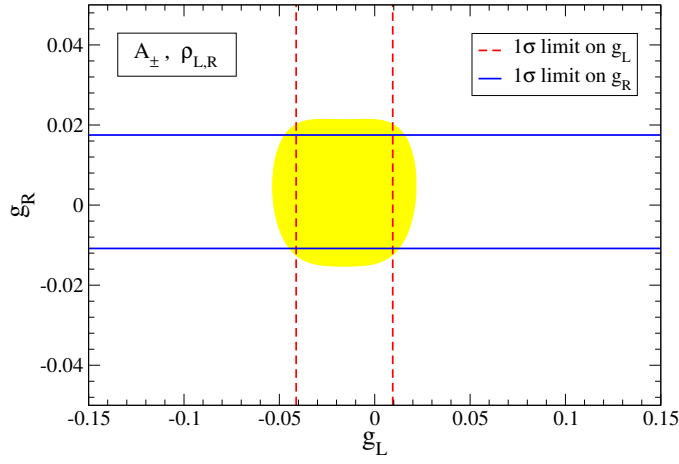
$$d = \begin{pmatrix} A_+ (\text{measured}) - A_+ (\text{generated}) \\ A_- (\text{measured}) - A_- (\text{generated}) \\ \rho_L (\text{measured}) - \rho_L (\text{generated}) \\ \rho_R (\text{measured}) - \rho_R (\text{generated}) \end{pmatrix}.$$

4. The corresponding χ^2 was evaluated by the expression $\chi^2 = d^T V^{-1} d$, where d^T is the transpose of vector d and V^{-1} is the inverse of the covariance matrix ($V_{ij} = \rho_{ij} \sigma_i \sigma_j$, where ρ_{ij} is the correlation between the observable i and j , and σ_i, σ_j are the experimental errors on these observables).
5. The boundary of the 68% CL regions was chosen as a contour of constant χ^2 . If the p.d.f. of V_R and g_L were Gaussian, the boundaries would be ellipses corresponding to $\chi^2 = 2.30$ [130]. In the present case the χ^2 for which the confidence regions have 68.3% probability was determined numerically. The probability for each generated point to be accepted is given by $P = e^{-\chi^2/2}$.

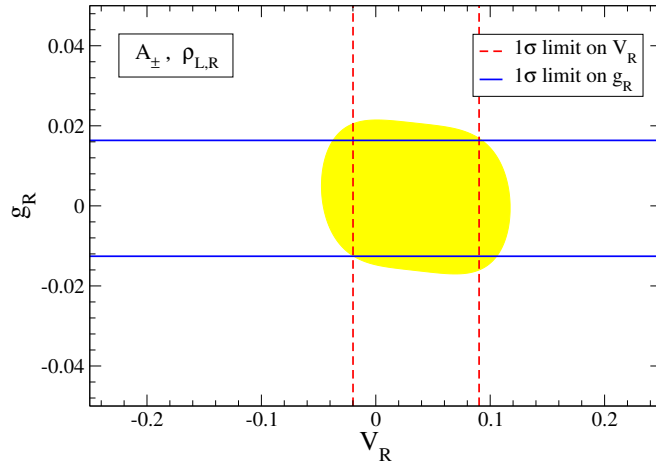
The expected 68.3% CL confidence regions on the anomalous couplings for $L = 10 \text{ fb}^{-1}$ are shown in figure 6.1. In addition to these regions, additional solutions can be found at $g_R \sim 0.75$, as shown in figure 6.2. Such solutions are due to a large cancellation between $\mathcal{O}(g_R)$ and $\mathcal{O}(g_R^2)$ terms (*c.f.* equations 2.6) and lead to a large single top cross-section [41]. Therefore, the measurement at the LHC of the single top production cross-section will allow to either exclude these additional solutions or to find an evidence for new physics.

The comparison between the limits expected for $L = 10 \text{ fb}^{-1}$ and $L = 1 \text{ fb}^{-1}$ (analysis with and without b -tagging) is shown in figure 6.3. It should be noticed that these limits were obtained using observables from different analyses and, therefore, the difference between them is larger than what would be expectable from the reduction of the statistical errors due to the increase in luminosity. In fact, the systematic errors of the A_{\pm} observables got degraded by a factor 6 to 9 when comparing the $L = 10 \text{ fb}^{-1}$ and the $L = 1 \text{ fb}^{-1}$ analyses. These observables are the most sensitive ones for the determination of the g_R coupling, which depends linearly on them. The g_L and V_R couplings are determined essentially by the ρ_R observable, which is degraded by a factor ~ 3 . Moreover, it should be noticed that the dependence of ρ_R with g_L and V_R is quadratic and, therefore, the impact of the systematic error increase is less important in this case.

The degradation of the systematic error for the $L = 1 \text{ fb}^{-1}$ analyses is due to a more conservative approach. It is expectable that for $L = 10 \text{ fb}^{-1}$ the systematic



(a)



(b)

Figure 6.1: *Expected 68.3% CL confidence regions on the anomalous couplings for $L = 10 \text{ fb}^{-1}$: (a) g_R vs. g_L , for $V_R = 0$ and (b) g_R vs. V_R , for $g_L = 0$. The 1σ combined limits shown in table 6.5 are also displayed. The χ^2 corresponding to 68.3% CL is, in this case, approximately 1.8.*

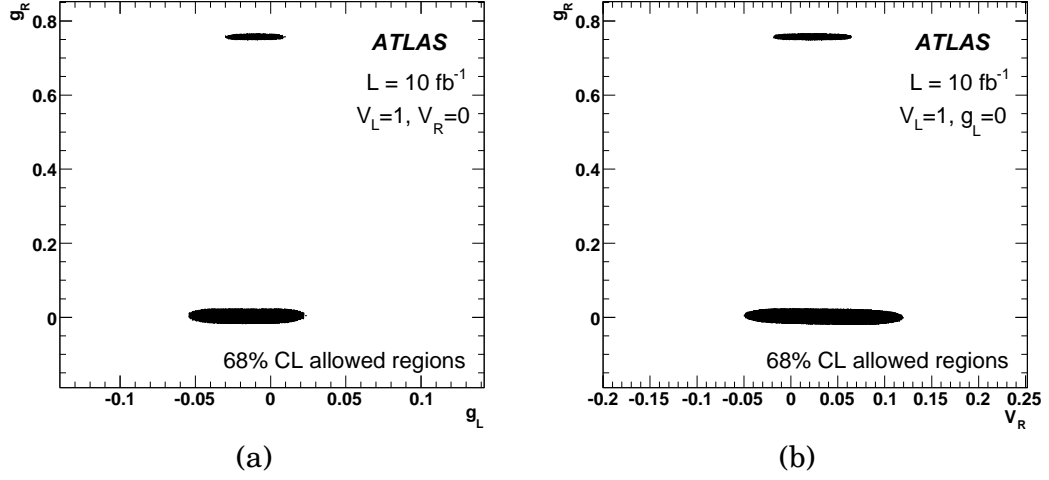


Figure 6.2: *Expected 68.3% CL confidence regions on the anomalous couplings for $L = 10 \text{ fb}^{-1}$: (a) g_R vs. g_L , for $V_R = 0$ and (b) g_R vs. V_R , for $g_L = 0$. The additional solutions at $g_R \sim 0.75$ are due to a large cancellation between linear and quadratic terms in g_R . Further information on these additional solutions will be provided by the measurement of the single top cross-section at the LHC.*

uncertainties will be reduced, due to a better understanding of the detector and backgrounds. As an example, it should be noticed that a 50% error on the W +jets background normalization and 5% error in the jet energy scale were assumed for $L = 1 \text{ fb}^{-1}$, while for $L = 10 \text{ fb}^{-1}$ a 10% error in the W +jets cross-section and 1% error in the light jet energy scale were considered. Moreover, the determination of the systematic uncertainties for $L = 1 \text{ fb}^{-1}$ is affected by the statistical errors (due to the limited statistics of the full simulation samples, as discussed in section 5.2.4).

Using the results obtained by the CDF collaboration for the W helicity fractions ($L = 1.9 \text{ fb}^{-1}$) [131],

$$F_0 = 0.65 \pm 0.19(\text{stat}) \pm 0.03(\text{syst})$$

$$F_R = -0.03 \pm 0.07(\text{stat}) \pm 0.03(\text{syst}) \quad (6.2)$$

(with the correlation coefficient being -0.82), limits on the anomalous couplings were derived using TopFit [57]. These limits are compared with the ATLAS expectations for $L = 1 \text{ fb}^{-1}$ in figure 6.4. A significant improvement on present limits is expected at ATLAS, even for $L = 1 \text{ fb}^{-1}$.

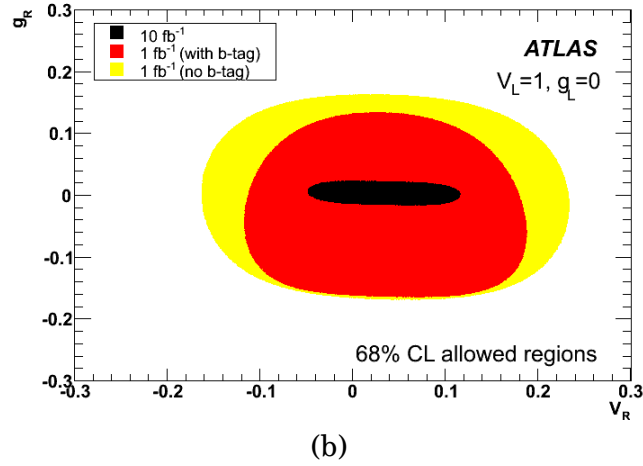
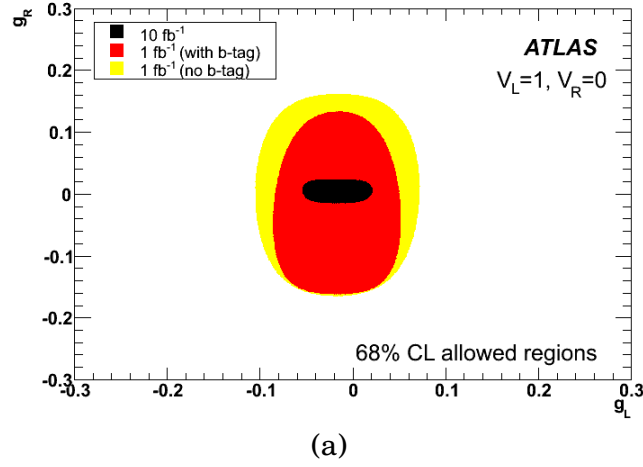
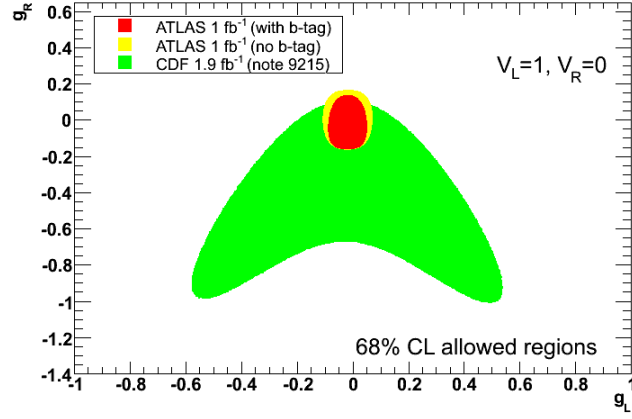
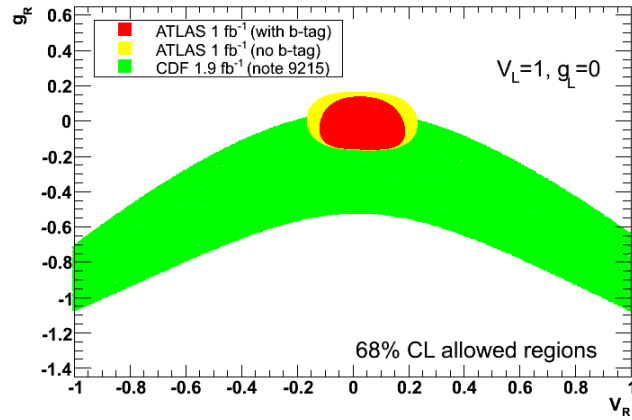


Figure 6.3: *Expected 68.3% CL confidence regions on the anomalous couplings: (a) g_R vs. g_L , for $V_R = 0$ and (b) g_R vs. V_R , for $g_L = 0$. The comparison between the limits obtained for $L = 10 \text{ fb}^{-1}$ and $L = 1 \text{ fb}^{-1}$ (analyses with and without b -tagging) is shown. The χ^2 corresponding to 68.3% CL is approximately 1.8 for $L = 10 \text{ fb}^{-1}$ analysis, 2.4 for the $L = 1 \text{ fb}^{-1}$ analysis without b -tagging and 2.3 for $L = 1 \text{ fb}^{-1}$ analysis with b -tagging.*



(a)



(b)

Figure 6.4: Expected 68.3% CL allowed regions on the Wtb anomalous couplings for ATLAS ($L = 1 \text{ fb}^{-1}$, analyses with and without b -tag) and Tevatron ($L = 1.9 \text{ fb}^{-1}$). Two anomalous couplings were allowed to vary and the third one was fixed to zero: (a) (g_L, g_R) plane and (b) (V_R, g_R) plane.

6.2 Possible improvements on the limits

The limits on the Wtb anomalous couplings can be improved if additional observables (besides A_{\pm} and $\rho_{R,L}$) are considered. In particular, the study of single top production will allow to obtain limits when all the anomalous couplings vary at the same time. Although the study of single top production is beyond the scope of the present thesis, a brief review is done in this section. A detailed discussion on single top quark production with anomalous couplings can be found in Ref. [41].

The single top production at the LHC has a cross-section about three times smaller than the one expected for $t\bar{t}$. Nevertheless, single top quarks will also be produced with large statistics at the LHC and, being produced through an electroweak Wtb interaction, they will provide essential information about the Wtb vertex. The single top production cross-sections are proportional to the size of this interaction, allowing to measure the value of the CKM matrix element V_{tb} , as well as bounds on possible anomalous couplings [41, 55, 132]. Moreover, single top quarks will be produced with a high degree of polarisation [133] (unlike the QCD $t\bar{t}$ production), which allows to build top spin asymmetries in the leptonic decay $t \rightarrow Wb \rightarrow \ell \nu b$ [57]. Such asymmetries will complement the A_{\pm} and $\rho_{R,L}$ observables measured in the W rest frame, allowing to test anomalous Wtb couplings in a model-independent way.

For the decay $t \rightarrow W^+ b \rightarrow \ell^+ \nu b, q \bar{q}' b$, the angular distributions of the top decay products ($X = \ell^+, \nu, q, \bar{q}', W^+, b$; which are called “spin analysers”) in the top quark rest frame are given by [134, 135]

$$\frac{1}{\Gamma} \frac{d\Gamma}{d\cos\theta_X} = \frac{1}{2}(1 + \alpha_X \cos\theta_X) \quad (6.3)$$

with θ_X being the angle between the three-momentum of X in the t rest frame and the top spin direction². The constant α_X is the “spin analysing power” of X and take values between -1 and 1 . For the decay of a top antiquark the distributions are the same, with $\alpha_{\bar{X}} = -\alpha_X$ as long as CP is conserved in the decay. In the SM, $\alpha_{\ell^+} = \alpha_{\bar{q}'} = 1$, $\alpha_{\nu} = \alpha_q = -0.319$, $\alpha_{W^+} = -\alpha_b = 0.406$ at the tree level (q and q' are the up- and down-type quarks, respectively, resulting from the W decay). Tree-level expressions of the spin analysing power constants for a CP-conserving Wtb vertex with t and b on-shell can be found in Ref. [57].

In the single top t -channel process, the top quarks are produced with a high degree of polarisation along the direction of the final state spectator jet [133]. The corresponding distributions are:

$$\frac{1}{\Gamma} \frac{d\Gamma}{d\cos\theta_X} = \frac{1}{2}(1 + P\alpha_X \cos\theta_X), \quad (6.4)$$

where the angles θ_X are measured using the jet momentum in the top quark rest frame as the spin direction (spectator basis), and $P \simeq 0.89$ is the top polarisation

² From the experimental point of view, different basis can be used to estimate the top spin axis [136, 133].

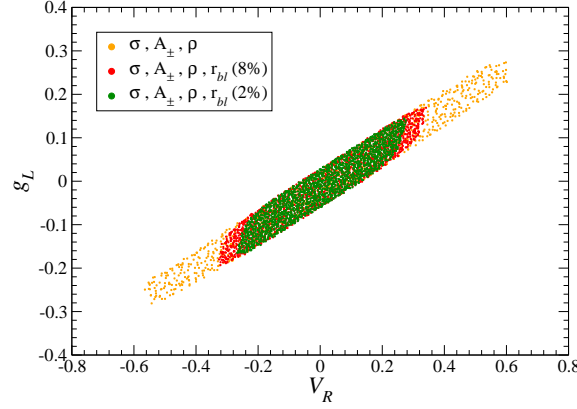


Figure 6.5: *Expected 68.3% CL confidence regions on the anomalous couplings, obtained from the A_{\pm} , $\rho_{R,L}$, single top cross-section and r_{bl} observables (figure taken from Ref. [41]). The projection on the (V_R, g_L) plane of the tetradimensional combined limits (V_L , V_R , g_L and g_R) is shown for the cases where r_{bl} is not measured or it is measured with precisions of 8% and 2%.*

along this axis. Forward-backward asymmetries can be built using these distributions,

$$A_X = \frac{N(\cos\theta_X > 0) - N(\cos\theta_X < 0)}{N(\cos\theta_X > 0) + N(\cos\theta_X < 0)} = \frac{1}{2}P\alpha_X. \quad (6.5)$$

These spin asymmetries depend on the top polarisation (P) but their ratios,

$$r_{bl} \equiv \frac{A_b}{A_\ell} = \frac{\alpha_b}{\alpha_\ell}$$

and

$$r_{vl} \equiv \frac{A_v}{A_\ell} = \frac{\alpha_v}{\alpha_\ell}, \quad (6.6)$$

only depend on anomalous couplings and on the masses of the particles involved. Additionally, the systematic errors associated to these ratios are expected to be smaller than those for the spin asymmetries themselves.

The inclusion of the spin asymmetry ratio r_{bl} in the limits evaluation allows to partially solve the problem of the fine-tuned cancellation between V_R and g_L . The single top cross-section allows to exclude the solutions found at $g_R \sim 0.75$. Additionally, the inclusion of these new observables allows to obtain meaningful limits when all the anomalous couplings (V_L , V_R , g_L and g_R) are different from zero. In figure 6.5 the projection on the (V_R, g_L) plane of the tetradimensional combined limits is shown ³ for the cases where r_{bl} is not measured or it is measured with precisions of 8% and 2%.

In $t\bar{t}$ production the top quarks are unpolarised at the tree level, but their spins are correlated [137, 138]. Therefore, r_{bl} and r_{vl} can be measured in top pair production through the choice of suitable ratios of spin asymmetries [57]. The precision in

³ This figure was taken from Ref. [41], where a detailed discussion on these results is done.

$t\bar{t}$ production will likely be worse than in single top production, because spin correlation asymmetries are numerically smaller (by a factor of 8 in the $t\bar{t}$ semileptonic decay channel).

Chapter 7

CONCLUSIONS

THE ATLAS SENSITIVITY to Wtb anomalous couplings was discussed in the present thesis. The semileptonic $t\bar{t}$ (with an electron or muon in the final state) was the studied signal. Specific probabilistic analyses were developed for luminosities of 10 and 1 fb⁻¹. For this, the LipCbrAnalysis program was developed.

Due to the large statistics achievable at the LHC, the systematic errors are expected to be dominant. Consequently, a detailed discussion on possible systematic sources of uncertainties was done, using large Monte Carlo samples, obtained with the fast simulation. The detector and trigger effects on the analyses were studied using the full GEANT4 simulation samples which, although with smaller statistics, allow a detailed description of the ATLAS detector geometry and reconstruction algorithms. For the first LHC data ($L = 1 \text{ fb}^{-1}$), the performance of the analyses with and without b -tagging were compared.

After selecting the $t\bar{t}$ signal (and subtracting the background), the $\cos\theta_\ell^*$ distribution was reconstructed and corrected for the selection and detector effects. Using this distribution, the ATLAS sensitivity to the W helicity fractions was evaluated. Additional observables, such as the W helicity ratios and the angular asymmetries were proposed. The ρ_R helicity ratio benefits from a smaller error, mainly due to some cancellation of systematic errors. The angular asymmetries were obtained through a simple counting of the number of events below and above a specific value of the $\cos\theta_\ell^*$ distribution and, therefore, are less biased by the extreme values of the angular distributions, where large corrections are needed.

The obtained ATLAS expectations for the different observables are:

$$\begin{aligned}
F_0 &= 0.700 \pm 0.003(\text{stat}) \pm 0.019(\text{sys}) & [L = 10 \text{ fb}^{-1}] \\
&= 0.690 \pm 0.019(\text{stat}) \pm 0.089(\text{sys}) & [L = 1 \text{ fb}^{-1}, \text{ with } b\text{-tag}] \\
F_L &= 0.299 \pm 0.003(\text{stat}) \pm 0.018(\text{sys}) & [L = 10 \text{ fb}^{-1}] \\
&= 0.312 \pm 0.019(\text{stat}) \pm 0.084(\text{sys}) & [L = 1 \text{ fb}^{-1}, \text{ with } b\text{-tag}] \\
F_R &= 0.001 \pm 0.001(\text{stat}) \pm 0.002(\text{sys}) & [L = 10 \text{ fb}^{-1}] \\
&= -0.003 \pm 0.005(\text{stat}) \pm 0.008(\text{sys}) & [L = 1 \text{ fb}^{-1}, \text{ with } b\text{-tag}] \\
\rho_L &= 0.427 \pm 0.008(\text{stat}) \pm 0.036(\text{sys}) & [L = 10 \text{ fb}^{-1}] \\
&= 0.453 \pm 0.048(\text{stat}) \pm 0.163(\text{sys}) & [L = 1 \text{ fb}^{-1}, \text{ with } b\text{-tag}] \\
\rho_R &= 0.0004 \pm 0.0021(\text{stat}) \pm 0.0016(\text{sys}) & [L = 10 \text{ fb}^{-1}] \\
&= -0.004 \pm 0.007(\text{stat}) \pm 0.012(\text{sys}) & [L = 1 \text{ fb}^{-1}, \text{ with } b\text{-tag}] \\
A_{\text{FB}} &= -0.223 \pm 0.004(\text{stat}) \pm 0.013(\text{sys}) & [L = 10 \text{ fb}^{-1}] \\
&= -0.229 \pm 0.026(\text{stat}) \pm 0.033(\text{sys}) & [L = 1 \text{ fb}^{-1}, \text{ with } b\text{-tag}] \\
A_+ &= 0.547 \pm 0.003(\text{stat}) \pm 0.001(\text{sys}) & [L = 10 \text{ fb}^{-1}] \\
&= 0.542 \pm 0.028(\text{stat}) \pm 0.052(\text{sys}) & [L = 1 \text{ fb}^{-1}, \text{ with } b\text{-tag}] \\
A_- &= -0.839 \pm 0.002(\text{stat}) \pm 0.003(\text{sys}) & [L = 10 \text{ fb}^{-1}] \\
&= -0.830 \pm 0.014(\text{stat}) \pm 0.027(\text{sys}) & [L = 1 \text{ fb}^{-1}, \text{ with } b\text{-tag}]
\end{aligned}$$

With the most sensitive observables (A_{\pm} and $\rho_{R,L}$), the ATLAS sensitivity to Wtb anomalous couplings was evaluated using TopFit. Assuming that only one of the anomalous couplings are nonzero, the following 1σ limits were obtained:

$$\begin{aligned}
V_R: & [-0.020, 0.091] & (L = 10 \text{ fb}^{-1}) \\
& [-0.062, 0.128] & (L = 1 \text{ fb}^{-1}, \text{ with } b\text{-tag}) \\
g_L: & [-0.041, 0.009] & (L = 10 \text{ fb}^{-1}) \\
& [-0.060, 0.028] & (L = 1 \text{ fb}^{-1}, \text{ with } b\text{-tag}) \\
g_R: & [-0.011, 0.017] & (L = 10 \text{ fb}^{-1}) \\
& [-0.118, 0.085] & (L = 1 \text{ fb}^{-1}, \text{ with } b\text{-tag})
\end{aligned}$$

Relaxing the assumption that only one coupling is nonzero at a time, expected 68.3% CL regions were obtained (figure 6.3). A significant improvement on present anomalous couplings limits (obtained from the CDF measurement of F_0 and F_R with $L = 1.9 \text{ fb}^{-1}$) is expected at ATLAS, even for $L = 1 \text{ fb}^{-1}$ (figure 6.4).

The results obtained in the present thesis were presented in several workshops and conferences [19, 139, 140, 141, 142], and published in ATLAS reports [108, 128] and peer-reviewed articles, published in international scientific journals [57, 125].

The obtained limits can be improved if additional observables, related with single top production, are considered. In fact, the full potential of LHC to probe the Wtb vertex will only be achieved if the pair and single top production results are combined. A detailed knowledge of this vertex is an important contribution to top

quark physics. These measurements at the LHC will allow to probe the Standard Model as well as to test new physics associated to the top quark, with an unprecedented precision.

Appendix A

EFFECT OF m_b IN THE HELICITY FRACTIONS

AS IT CAN BE OBSERVED in chapter 2 (equations 2.6), the interference terms involving V_R (or g_L) and the dominant SM coupling V_L are proportional to $x_b = m_b/m_t$. These terms are of equal size as the quadratic terms for small values of V_R , g_L , and cannot be neglected in the analysis.

The dependence of the three helicity fractions on the anomalous couplings is shown in figure A.1, for the cases where the b -quark mass is set to 4.8 GeV and when m_b is neglected. For F_0 , a more extreme effect is observed: the only dependence of this quantity on V_R is through the x_b term.

As it can be seen in figure A.1, if m_b is neglected, the resulting confidence intervals on V_R , g_L will be artificially symmetric.

This mass dependence of the limits originates a systematic uncertainty on m_b . The b -quark pole mass ($m_b = 4.8$ GeV) was used and, therefore, an ambiguity of the order of $\Lambda_{\text{QCD}} \sim 220$ MeV is expected [57]. The maximum effect observed in the V_R , g_L and g_R was 8%, 6% and 1%, respectively.

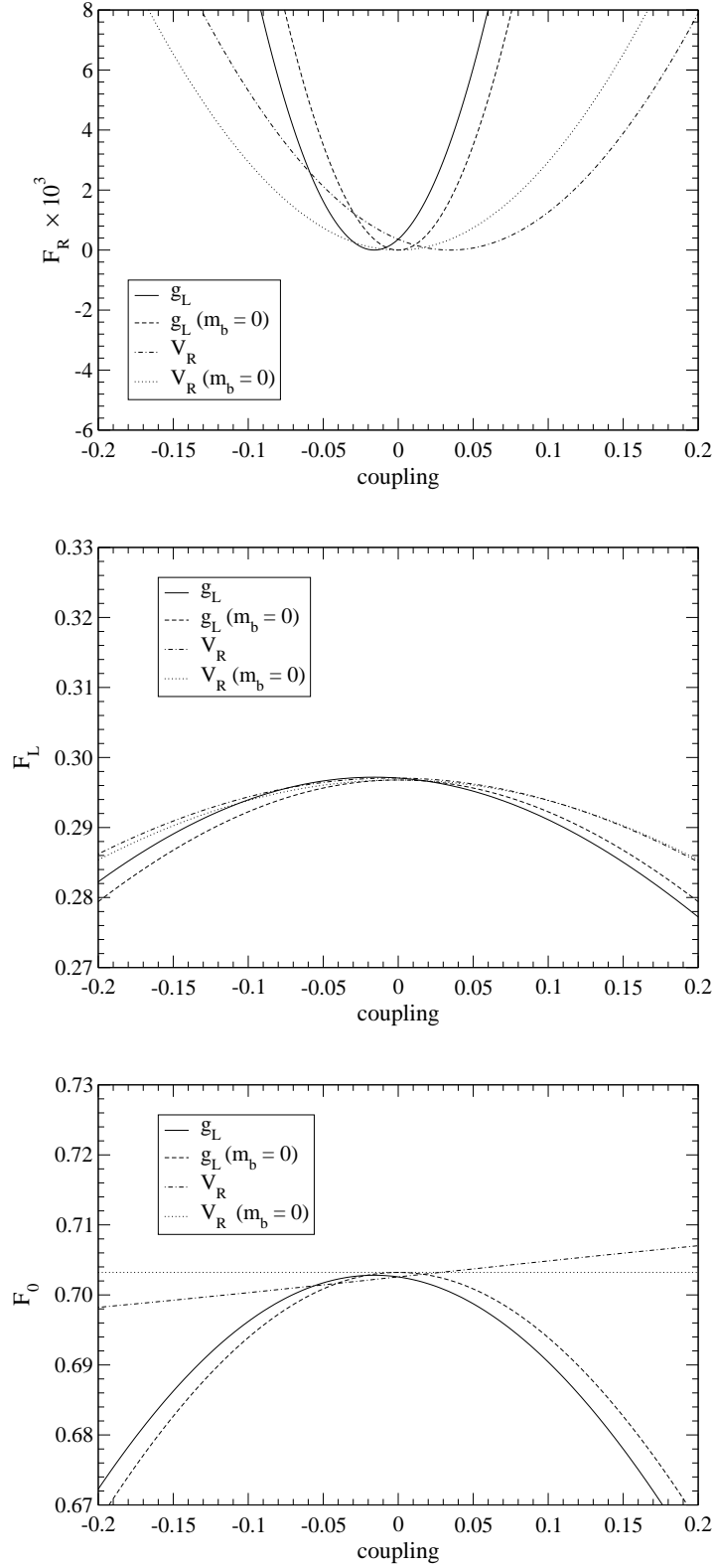


Figure A.1: Dependence of the helicity fractions F_i on V_R and g_L , for the cases when the b -quark is taken into account ($m_b = 4.8$ GeV) and when it is neglected.

Appendix B

FITS USED IN THE SYSTEMATIC ERROR EVALUATION

THE STUDY OF SYSTEMATIC UNCERTAINTIES was done by changing different parameters in the generation, simulation or reconstruction of the Monte Carlo samples, as described in chapters 4 and 5. For some of these studies, the dependence of the observables with the changed parameter was assumed to be linear. In this case, the corresponding systematic uncertainty was evaluated through a fit of the different values obtained for each observable. In the present appendix, these fits are shown for the A_{\pm} angular asymmetries and for the $\rho_{L,R}$ helicity ratios. The dependence with the b -jet energy scale, light jet energy scale, background normalization, top mass, ISR/FSR and b -tagging efficiency uncertainties are shown in figures B.1 to B.6, for the $L = 10 \text{ fb}^{-1}$ fast simulation analysis, described in section 5.1. The dependence with the jet energy scale, luminosity evaluation and top mass uncertainties is shown in figures B.7 to B.12, for the $L = 1 \text{ fb}^{-1}$ full simulation analysis (without and with b -tagging), described in section 5.2. The estimated systematic effect on each observable was evaluated as the slope of the fitted linear function times the corresponding expected systematic uncertainty.

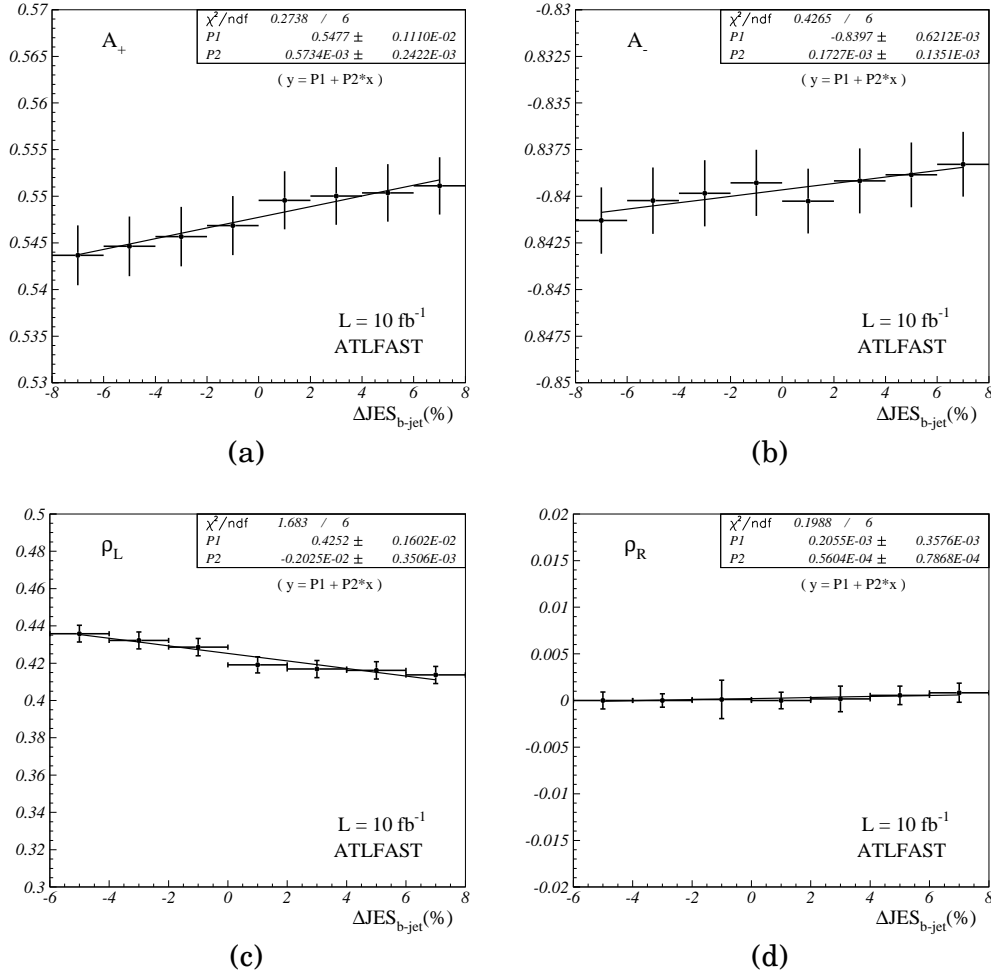


Figure B.1: Fits used in the b -jet energy scale systematic error evaluation (fast simulation analysis, $L = 10 \text{ fb}^{-1}$): (a) A_+ , (b) A_- , (c) ρ_L and (d) ρ_R .

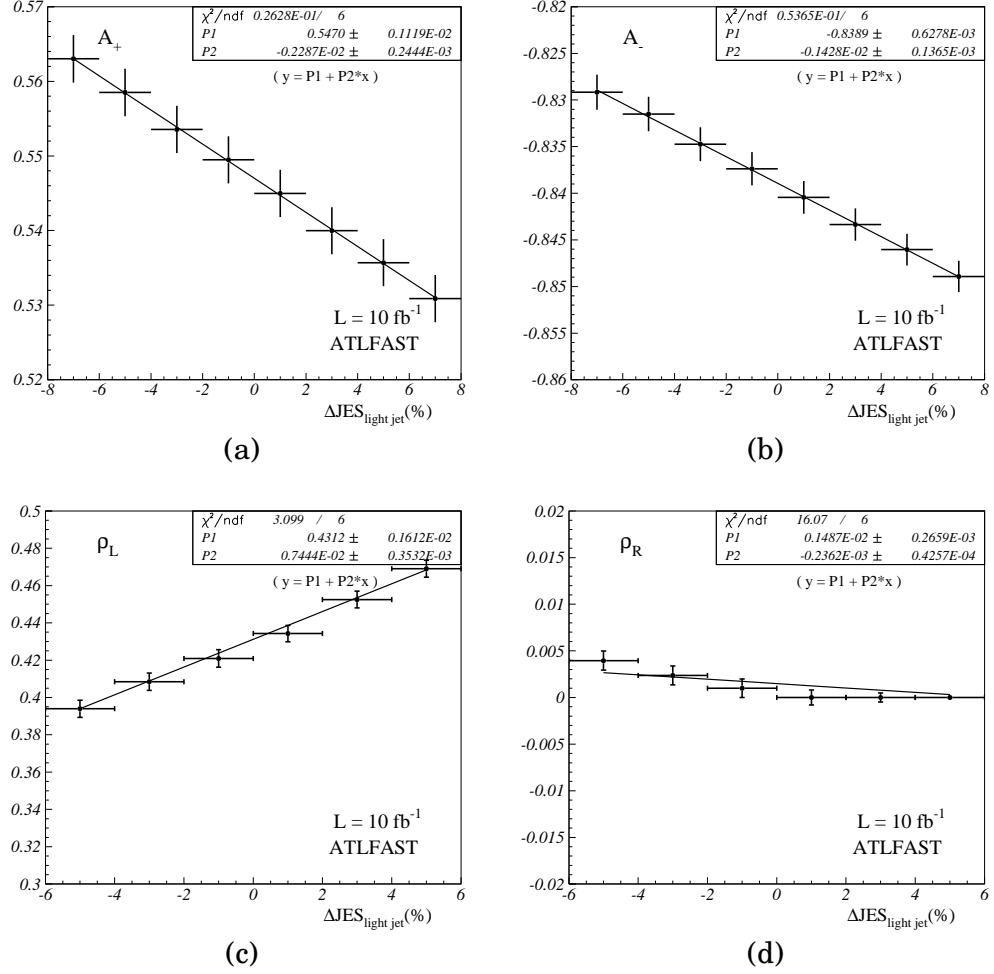


Figure B.2: Fits used in the light jet energy scale systematic error evaluation (fast simulation analysis, $L = 10 \text{ fb}^{-1}$): (a) A_+ , (b) A_- , (c) ρ_L and (d) ρ_R .

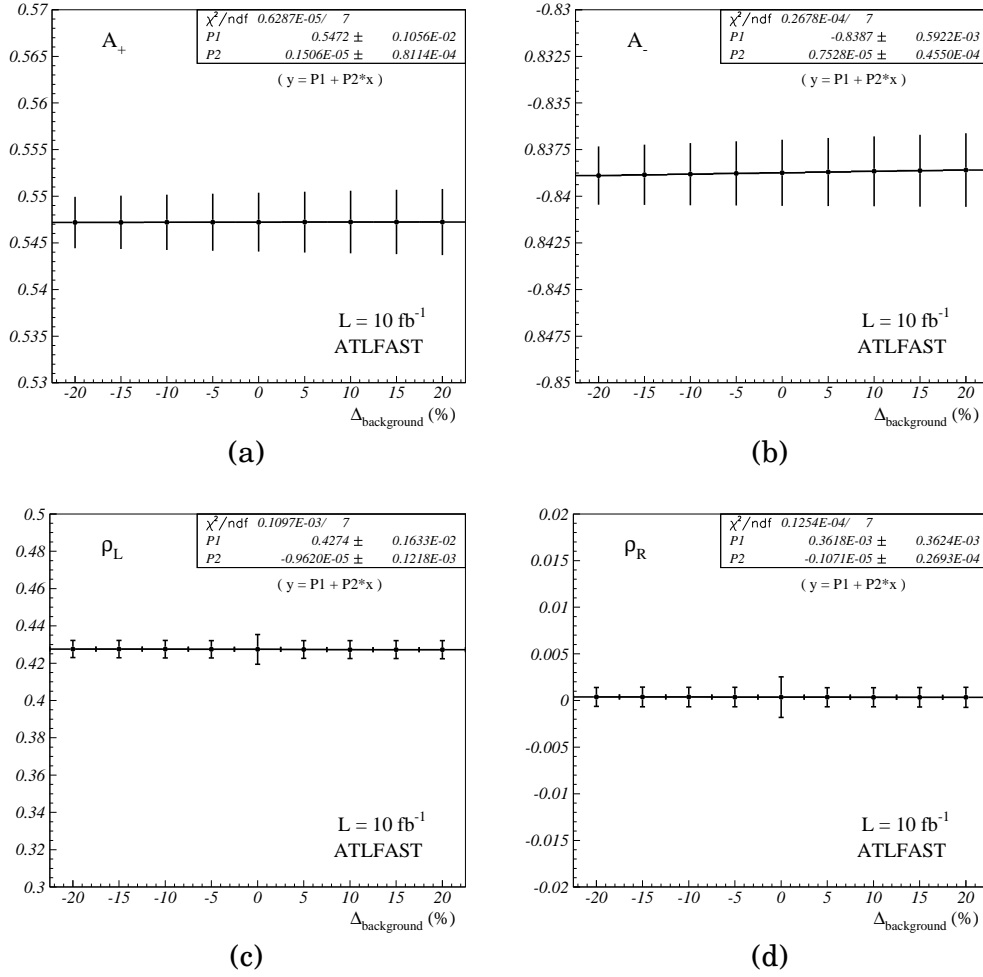


Figure B.3: Fits used in the background normalization systematic error evaluation (fast simulation analysis, $L = 10 \text{ fb}^{-1}$): (a) A_+ , (b) A_- , (c) ρ_L and (d) ρ_R .

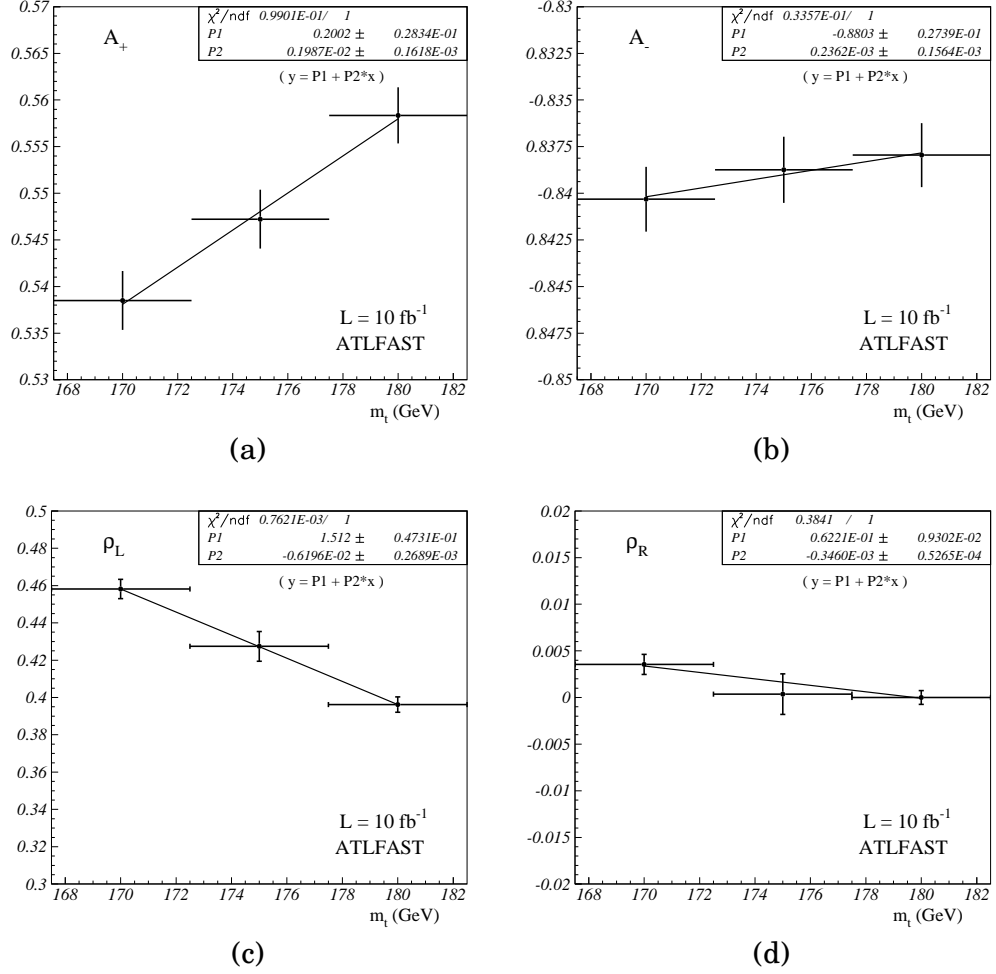


Figure B.4: Fits used in the top mass systematic error evaluation (fast simulation analysis, $L = 10 \text{ fb}^{-1}$): (a) A_+ , (b) A_- , (c) ρ_L and (d) ρ_R .

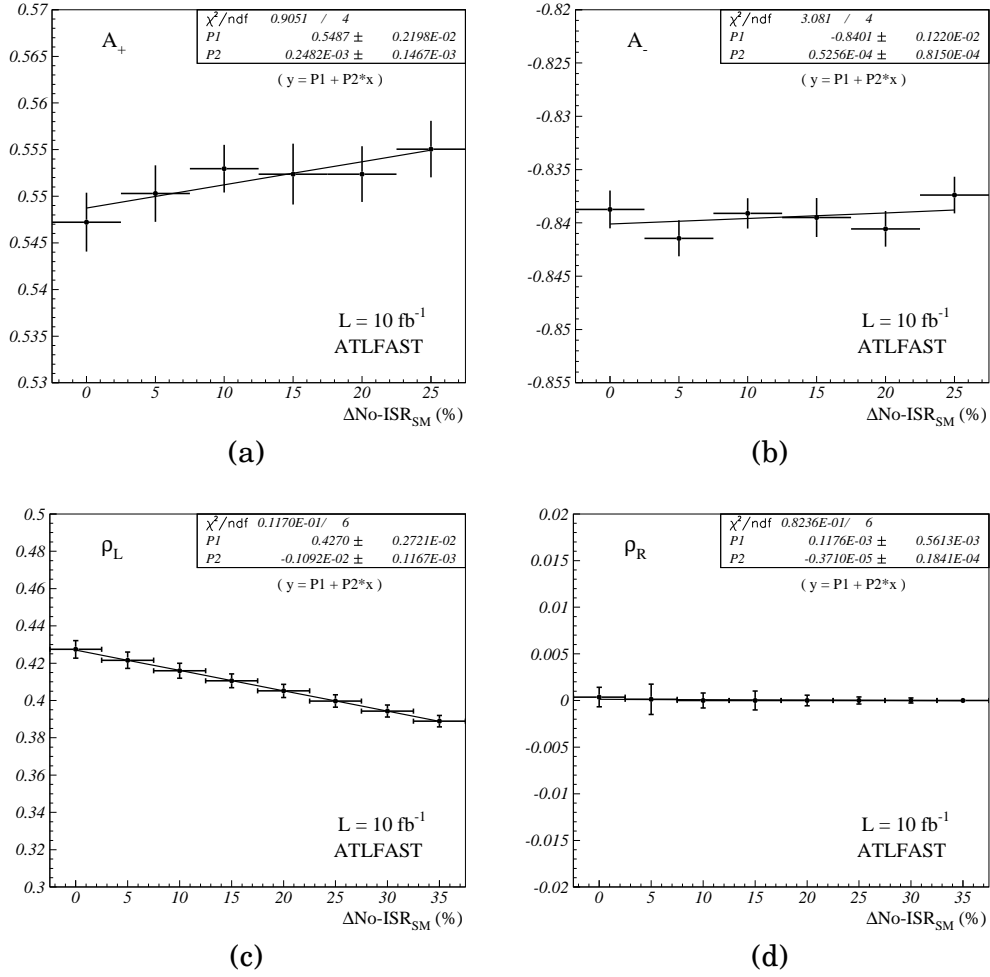


Figure B.5: Fits used in the ISR/FSR systematic error evaluation (fast simulation analysis, $L = 10 \text{ fb}^{-1}$): (a) A_+ , (b) A_- , (c) ρ_L and (d) ρ_R .

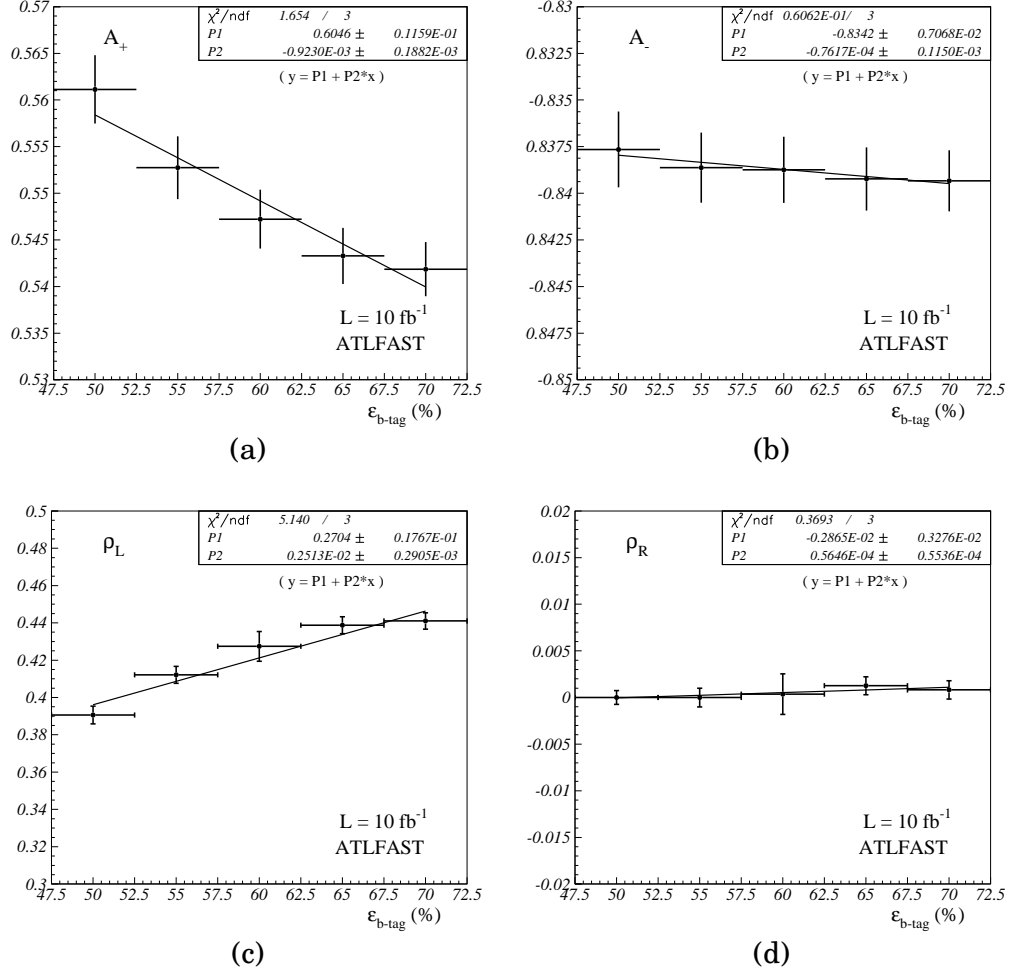


Figure B.6: Fits used in the b -tagging efficiency systematic error evaluation (fast simulation analysis, $L = 10 \text{ fb}^{-1}$): (a) A_+ , (b) A_- , (c) ρ_L and (d) ρ_R .

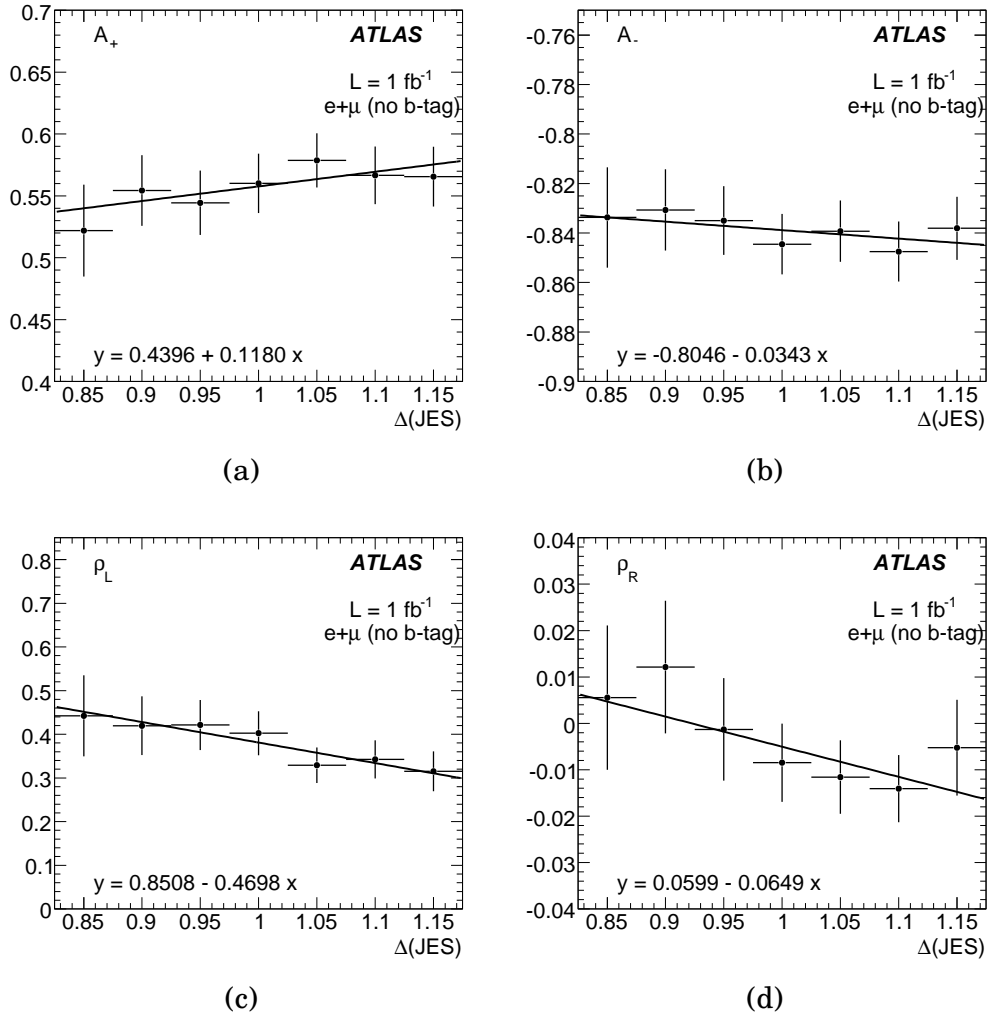


Figure B.7: Fits used in the jet energy scale systematic error evaluation (full simulation analysis without b -tagging, $L = 1 \text{ fb}^{-1}$): (a) A_+ , (b) A_- , (c) ρ_L and (d) ρ_R .

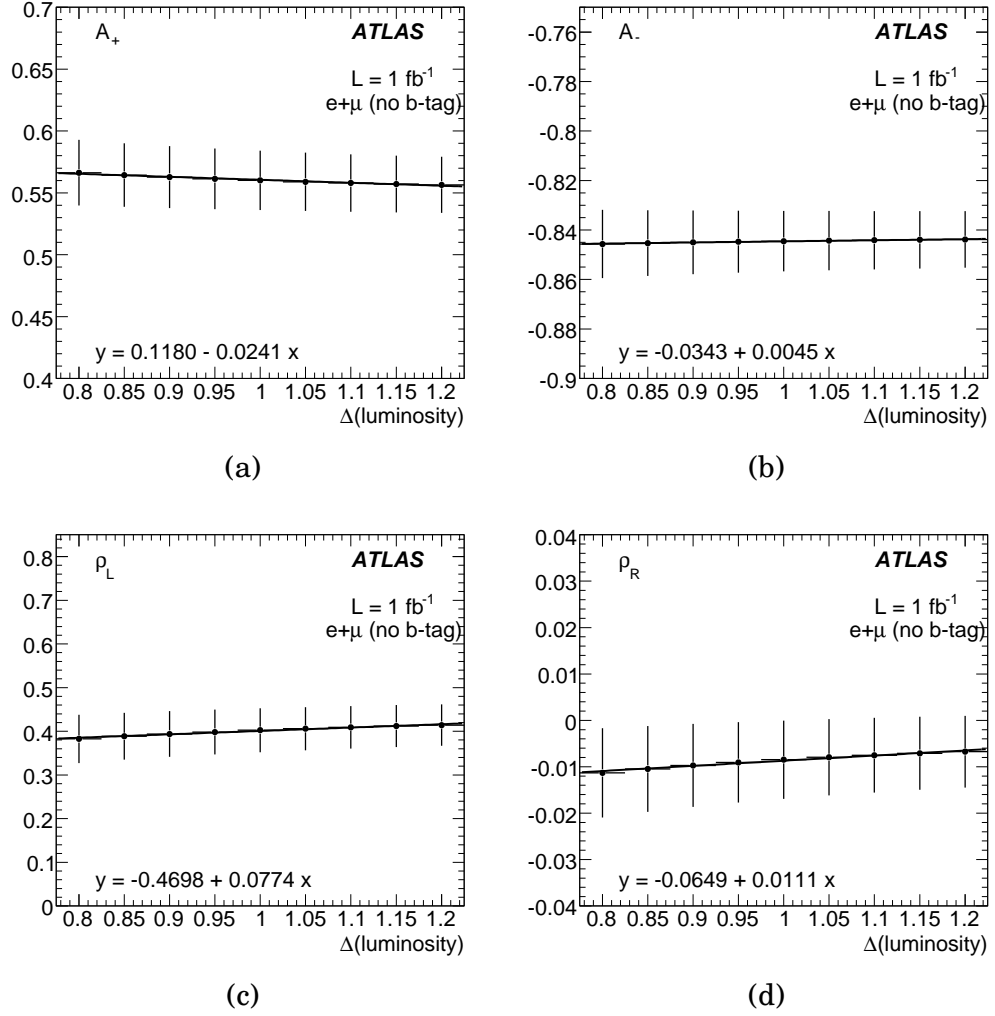


Figure B.8: Fits used in the luminosity systematic error evaluation (full simulation analysis without b -tagging, $L = 1 \text{ fb}^{-1}$): (a) A_+ , (b) A_- , (c) ρ_L and (d) ρ_R .

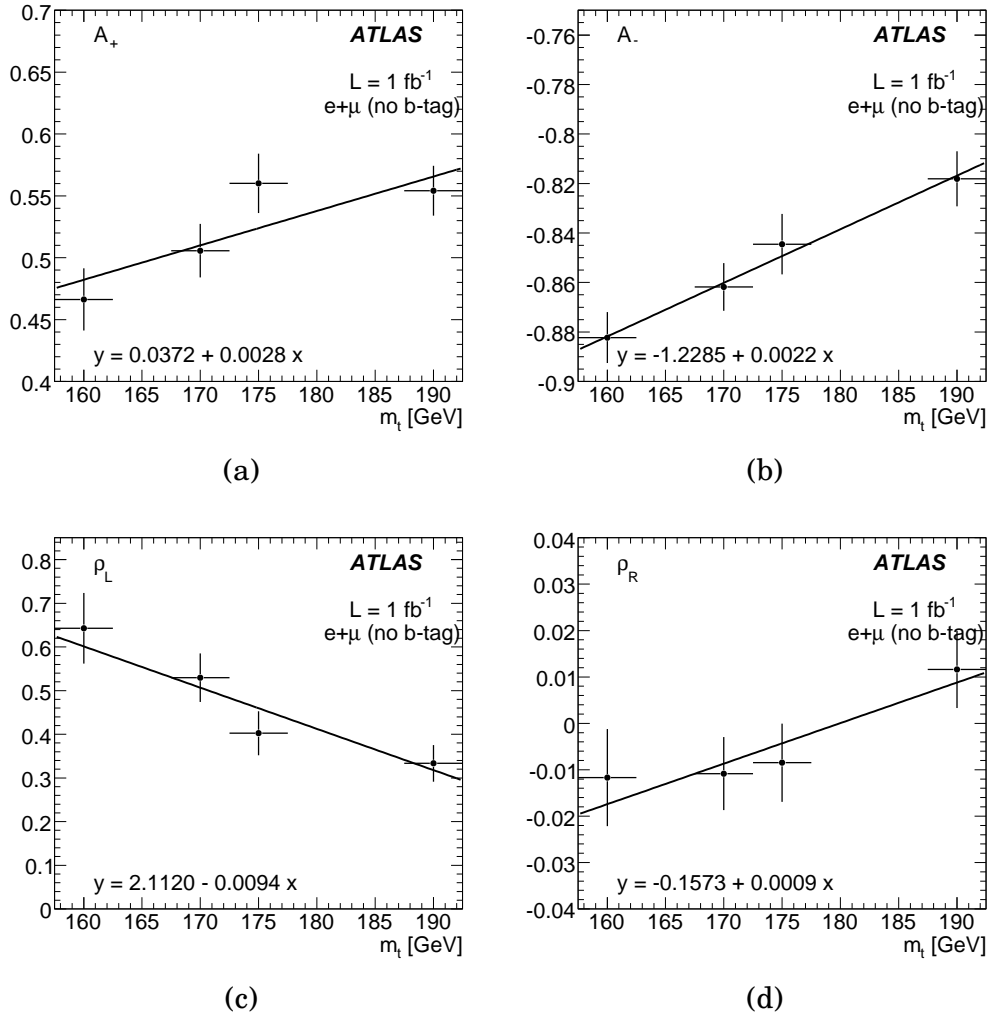


Figure B.9: Fits used in the top mass systematic error evaluation (full simulation analysis without b -tagging, $L = 1 \text{ fb}^{-1}$): (a) A_+ , (b) A_- , (c) ρ_L and (d) ρ_R .

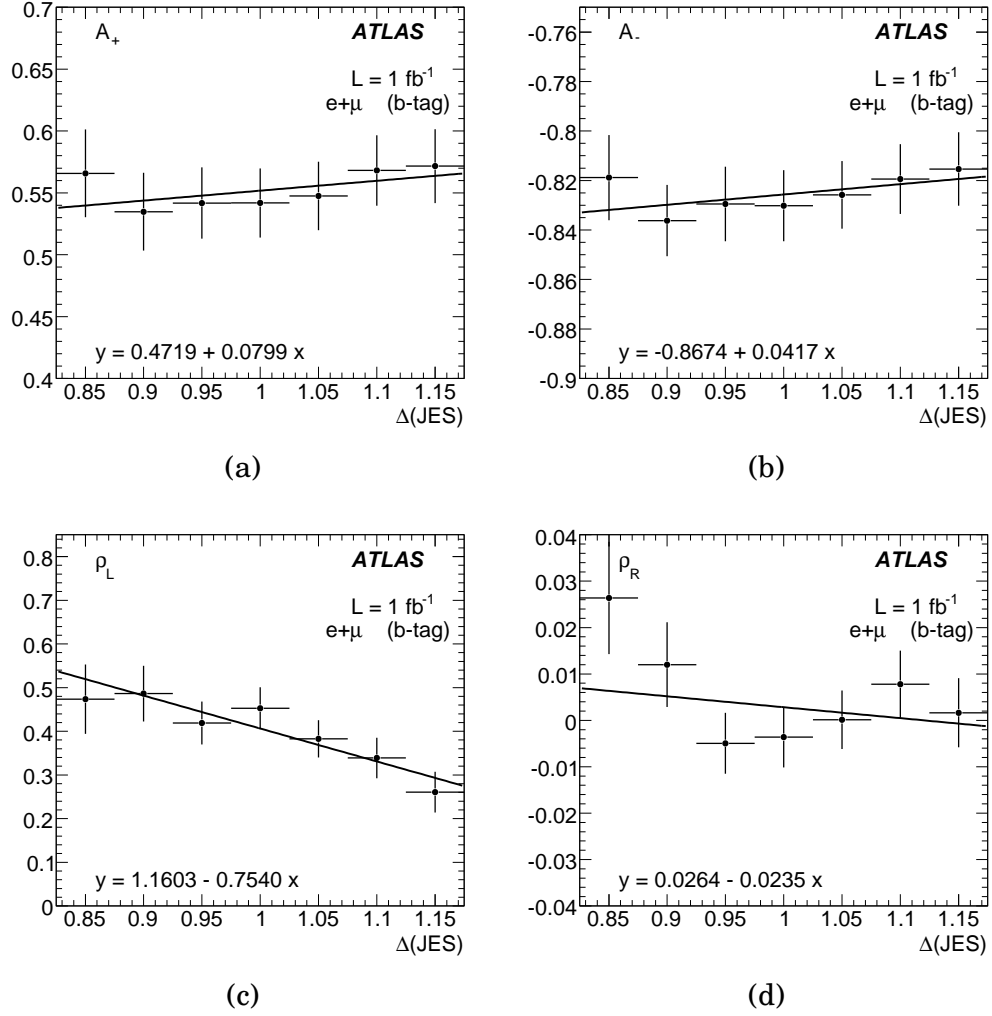


Figure B.10: *Fits used in the jet energy scale systematic error evaluation (full simulation analysis with b-tagging, $L = 1 \text{ fb}^{-1}$): (a) A_+ , (b) A_- , (c) ρ_L and (d) ρ_R .*

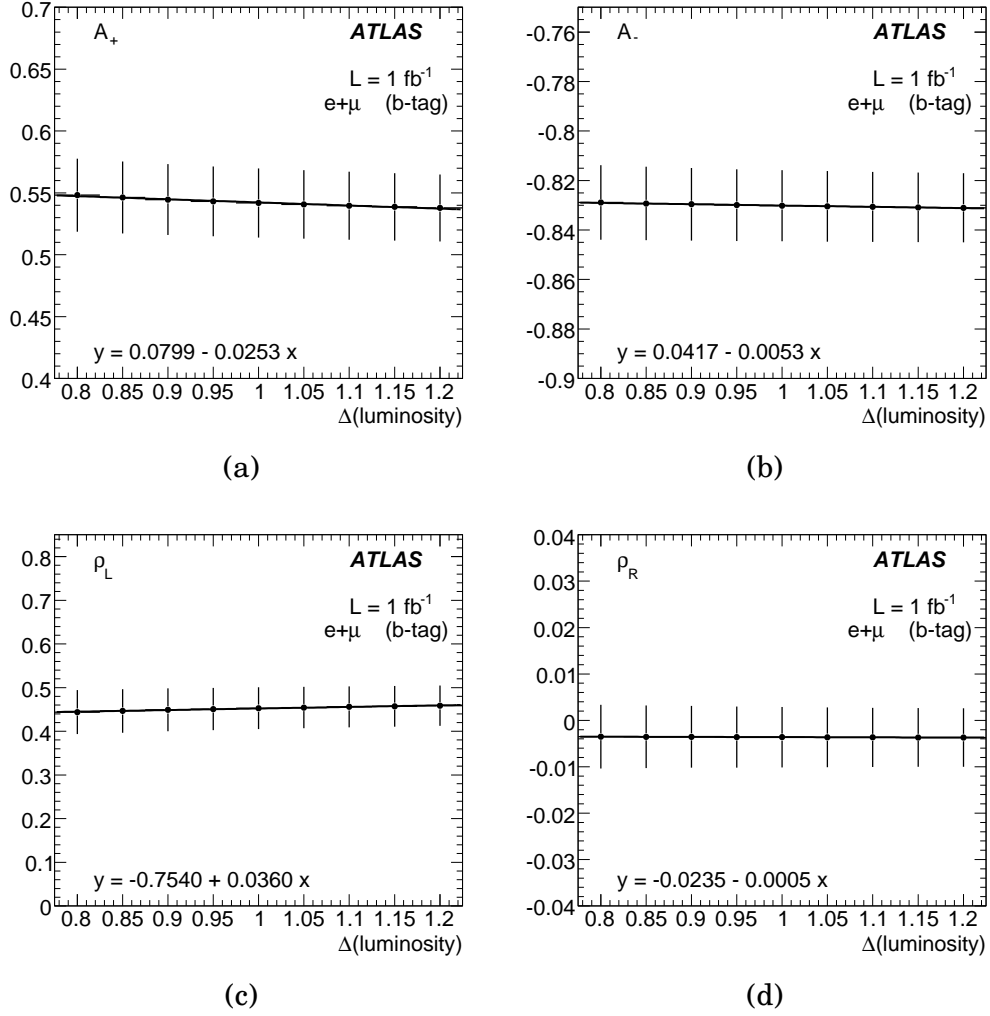


Figure B.11: Fits used in the luminosity systematic error evaluation (full simulation analysis with b -tagging, $L = 1 \text{ fb}^{-1}$): (a) A_+ , (b) A_- , (c) ρ_L and (d) ρ_R .

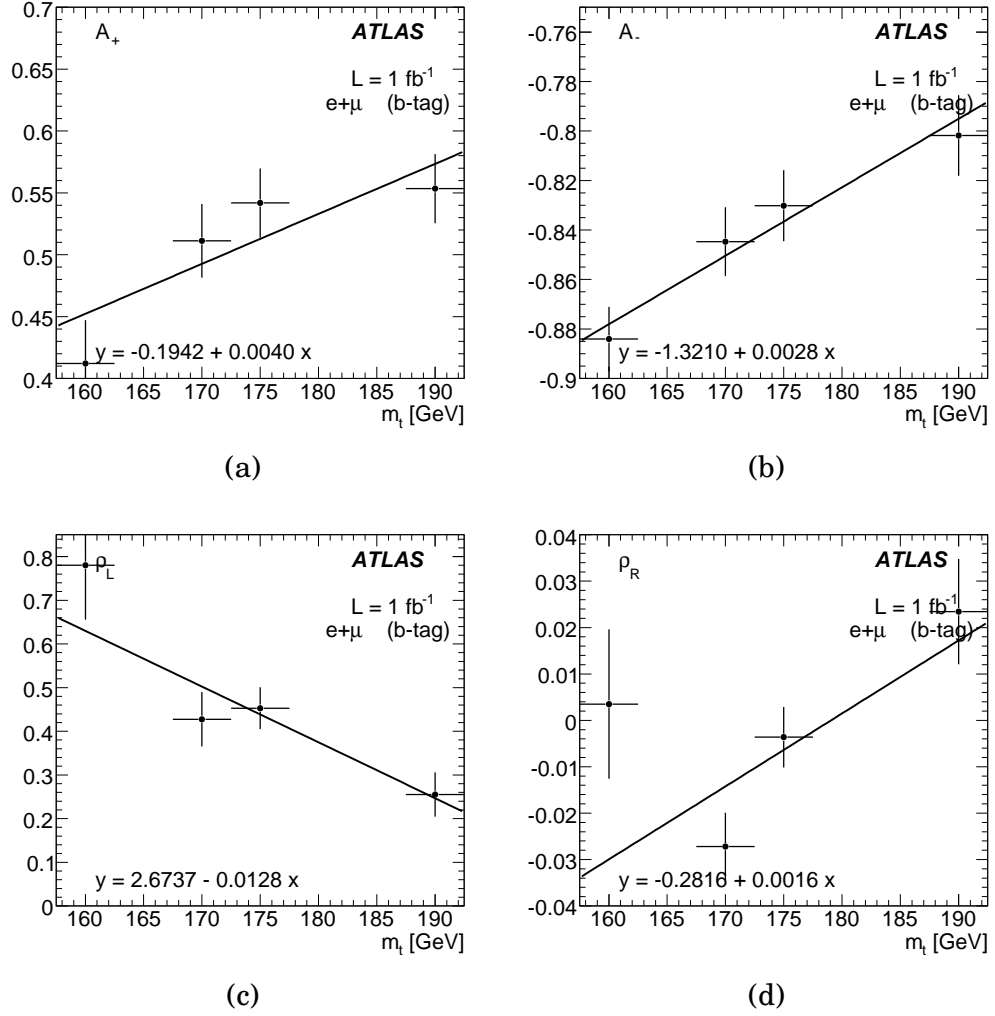


Figure B.12: *Fits used in the top mass systematic error evaluation (full simulation analysis with b -tagging, $L = 1 \text{ fb}^{-1}$): (a) A_+ , (b) A_- , (c) ρ_L and (d) ρ_R .*

Bibliography

- [1] **Tevatron Electroweak Working Group** for the CDF and D0 Collaborations, *A Combination of CDF and D0 Results on the Mass of the Top Quark*, arXiv:0803.1683 [hep-ph].
- [2] M. Beneke *et. al.*, *Top quark physics*, arXiv:hep-ph/0003033.
- [3] W. Bernreuther, *Top quark physics at the LHC*, *J. Phys.* **G35** (2008) 083001.
- [4] S. L. Glashow, *Partial Symmetries of Weak Interactions*, *Nucl. Phys.* **22** (1961) 579–588.
- [5] A. Salam, “Weak and Electromagnetic Interactions.” Originally printed in Svartholm: Elementary Particle Theory, Proceedings Of The Nobel Symposium, held at Lerum, Sweden, Stockholm, 1968.
- [6] S. Weinberg, *A Model of Leptons*, *Phys. Rev. Lett.* **19** (1967) 1264–1266.
- [7] M. Gell-Mann, *Behavior of current divergences under $SU(3) \times SU(3)$* , *Phys. Rev.* **175** (1968) 2195–2199.
- [8] G. Zweig, “An SU_3 model for strong interaction symmetry and its breaking.” CERN/TH 401, 1964.
- [9] C. Bouchiat, J. Iliopoulos and Ph. Meyer, *An Anomaly Free Version of Weinberg’s Model*, *Phys. Lett.* **B28** (1972) 519–523.
- [10] S. Weinberg, *The Quantum Theory of Fields - volume II*. Cambridge University Press, 1998.
- [11] P. W. Higgs, *Broken symmetries, massless particles and gauge fields*, *Phys. Lett.* **12** (1964) 132–133.
- [12] P. W. Higgs, *Spontaneous Symmetry Breakdown Without Massless Bosons*, *Phys. Rev.* **145** (1966) 1156–1163.
- [13] J. F. Donoghue, E. Golowich and B. R. Holstein, *Dynamics of the Standard Model*. Cambridge University Press, 1996.
- [14] **Super-Kamiokande** Collaboration, S. Fukuda *et. al.*, *Determination of solar neutrino oscillation parameters using 1496 days of Super-Kamiokande-I data*, *Phys. Lett.* **B539** (2002) 179–187.

- [15] **K2K** Collaboration, M. H. Ahn *et. al.*, *Indications of neutrino oscillation in a 250-km long- baseline experiment*, *Phys. Rev. Lett.* **90** (2003) 041801.
- [16] **SNO** Collaboration, S. N. Ahmed *et. al.*, *Measurement of the total active B-8 solar neutrino flux at the Sudbury Neutrino Observatory with enhanced neutral current sensitivity*, *Phys. Rev. Lett.* **92** (2004) 181301.
- [17] **KamLAND** Collaboration, K. Eguchi *et. al.*, *First results from KamLAND: Evidence for reactor anti- neutrino disappearance*, *Phys. Rev. Lett.* **90** (2003) 021802.
- [18] M. C. Gonzalez-Garcia and M. Maltoni, *Phenomenology with Massive Neutrinos*, *Phys. Rept.* **460** (2008) 1–129.
- [19] F. del Aguila *et. al.*, *Collider aspects of flavour physics at high Q*, arXiv:0801.1800 [hep-ph].
- [20] F. del Aguila, S. Bar-Shalom, A. Soni and J. Wudka, *Heavy Majorana Neutrinos in the Effective Lagrangian Description: Application to Hadron Colliders*, arXiv:0806.0876 [hep-ph].
- [21] F. del Aguila, J. A. Aguilar-Saavedra and R. Pittau, *Heavy neutrino signals at large hadron colliders*, *JHEP* **10** (2007) 047.
- [22] J. C. Romao, *Supersymmetric Models for Neutrino Mass*, arXiv:0710.5730 [hep-ph].
- [23] C. Arina, F. Bazzocchi, N. Fornengo, J. C. Romao and J. W. F. Valle, *Minimal supergravity sneutrino dark matter and inverse seesaw neutrino masses*, arXiv:0806.3225 [hep-ph].
- [24] P. Fileviez Perez, T. Han, G.-y. Huang, T. Li and K. Wang, *Neutrino Masses and the LHC: Testing Type II Seesaw*, arXiv:0805.3536 [hep-ph].
- [25] W. Rodejohann, *The see-saw mechanism: neutrino mixing, leptogenesis and lepton flavor violation*, arXiv:0804.3925 [hep-ph].
- [26] M. Kobayashi and K. Maskawa, *CP Violation in the Renormalizable Theory of Weak Interaction*, *Prog. Theor. Phys.* **49** (1973) 652–657.
- [27] S. L. Glashow, J. Iliopoulos and L. Maiani, *Weak Interactions with Lepton-Hadron Symmetry*, *Phys. Rev.* **D2** (1970) 1285.
- [28] I. J. R. Aitchinson and A. J. G. Hey, *Gauge Theories in Particle Physics*. Institute of Physics Publishing, 1993.
- [29] **Particle Data Group** Collaboration, W. M. Yao *et. al.*, *Review of particle physics*, *J. Phys.* **G33** (2006) 1–1232.
- [30] **LEP Working Group for Higgs boson searches** Collaboration, R. Barate *et. al.*, *Search for the standard model Higgs boson at LEP*, *Phys. Lett.* **B565** (2003) 61–75.

- [31] **LEP EEWG, ALEPH, DELPHI, L3 and OPAL** Collaborations, D. Abbaneo *et. al.*, *Precision Electroweak Measurements and Constraints on the Standard Model*. LEPEWWG/2007-01, December, 2007.
- [32] L. Wolfenstein, *Mixing Angles, Mass Matrix, and CP Violation in the Kobayashi-Maskawa Model*, *Nucl. Phys.* **B160** (1979) 501.
- [33] **CDF** Collaboration, F. Abe *et. al.*, *Observation of top quark production in $\bar{p}p$ collisions*, *Phys. Rev. Lett.* **74** (1995) 2626–2631.
- [34] **D0** Collaboration, S. Abachi *et. al.*, *Observation of the top quark*, *Phys. Rev. Lett.* **74** (1995) 2632–2637.
- [35] R. Bonciani, S. Catani, M. L. Mangano and P. Nason, *NLL resummation of the heavy-quark hadroproduction cross- section*, *Nucl. Phys.* **B529** (1998) 424–450.
- [36] N. Kidonakis and R. Vogt, *Next-to-next-to-leading order soft-gluon corrections in top quark hadroproduction*, *Phys. Rev.* **D68** (2003) 114014.
- [37] S. Moch and P. Uwer, *Theoretical status and prospects for top-quark pair production at hadron colliders*, arXiv:0804.1476 [hep-ph].
- [38] M. Cacciari *et. al.*, *Updated predictions for the total production cross sections of top and of heavier quark pairs at the Tevatron and at the LHC*, arXiv:0804.2800 [hep-ph].
- [39] Z. Sullivan, *Understanding single-top-quark production and jets at hadron colliders*, *Phys. Rev.* **D70** (2004) 114012.
- [40] J. Campbell and F. Tramontano, *Next-to-leading order corrections to Wt production and decay*, *Nucl. Phys.* **B726** (2005) 109–130.
- [41] J. A. Aguilar-Saavedra, *Single top quark production at LHC with anomalous Wtb couplings*, arXiv:0803.3810 [hep-ph].
- [42] T. Stelzer, Z. Sullivan and S. Willenbrock, *Single top quark production at hadron colliders*, *Phys. Rev.* **D58** (1998) 094021.
- [43] A. S. Belyaev, E. E. Boos and L. V. Dudko, *Single top quark at future hadron colliders: Complete signal and background study*, *Phys. Rev.* **D59** (1999) 075001.
- [44] E. Boos, M. Dubinin, A. Pukhov, M. Sachwitz and H. J. Schreiber, *Single top production in e^+e^- , e^-e^- , γe and $\gamma\gamma$ collisions*, *Eur. Phys. J.* **C21** (2001) 81–91.
- [45] J. A. Aguilar-Saavedra, *Effects of mixing with quark singlets*, *Phys. Rev.* **D67** (2003) 035003.

- [46] F. Del Aguila and J. Santiago, *Signals from extra dimensions decoupled from the compactification scale*, *JHEP* **03** (2002) 010.
- [47] J.-j. Cao, R. J. Oakes, F. Wang and J. M. Yang, *Supersymmetric effects in top quark decay into polarized W-boson*, *Phys. Rev.* **D68** (2003) 054019.
- [48] X.-l. Wang, Q.-l. Zhang and Q.-p. Qiao, *Studying top quark decay into the polarized W-boson in the TC2 model*, *Phys. Rev.* **D71** (2005) 014035.
- [49] C. Itzykson and J.-B. Zuber, *Quantum Field Theory*. McGraw-Hill, 1985.
- [50] J. G. K. H. S. Do, S. Groote and M. C. Mauser, *Electroweak and finite width corrections to top quark decays into transverse and longitudinal W-bosons*, *Phys. Rev. D* **67** (2003) 091501.
- [51] **Heavy Flavor Averaging Group** Collaboration, E. Barberio *et. al.*, *Averages of b-hadron properties at the end of 2006*, arXiv:0704.3575 [hep-ex].
- [52] B. Grzadkowski and M. Misiak, *Anomalous Wtb coupling effects in the weak radiative B- meson decay*, 0802.1413.
- [53] F. del Aguila and J. A. Aguilar-Saavedra, *Precise determination of the Wtb couplings at LHC*, *Phys. Rev. D* **67** (2003) 014009.
- [54] D. Espriu and J. Manzano, *A study of top polarization in single-top production at the LHC*, *Phys. Rev.* **D66** (2002) 114009.
- [55] C.-R. Chen, F. Larios and C. P. Yuan, *General Analysis of Single Top Production and W Helicity in Top Decay*, *Phys. Lett.* **B631** (2005) 126–132.
- [56] G. L. Kane, G. A. Ladinsky and C. P. Yuan, *Using the top quark for testing standard model polarization and CP predictions*, *Phys. Rev. D* **45** (1992) 124.
- [57] J. A. Aguilar-Saavedra, J. Carvalho, N. Castro, F. Veloso and A. Onofre, *Probing anomalous Wtb couplings in top pair decays*, *Eur. Phys. J.* **C50** (2007) 519–533.
- [58] R. H. Dalitz and G. R. Goldstein, *The Decay and polarization properties of the top quark*, *Phys. Rev.* **D45** (1992) 1531–1543.
- [59] **CDF** Collaboration, “Measurement of W-Boson Helicity Fractions in Top-Quark Decays Using $\cos\theta^*$.” Conf. Note 9215, 2007.
- [60] **D0** Collaboration, V. M. Abazov *et. al.*, *Model-independent measurement of the W boson helicity in top quark decays*, *Phys. Rev. Lett.* **100** (2008) 062004.
- [61] B. Lampe, *Forward - backward asymmetry in top quark semileptonic decay*, *Nucl. Phys. B* **454** (1995) 506.
- [62] J. Erler and P. Langacker, *Status of the standard model*, hep-ph/9809352.

- [63] R. J. Oakes, J. M. Yang and B.-L. Young, *Implications of LEP/SLD data for new physics in $Zb\bar{b}$ couplings*, *Phys. Rev.* **D61** (2000) 075007.
- [64] O. Bruning (Ed.) *et. al.*, *LHC design report. Vol. I: The LHC main ring*, Tech. Rep. CERN-2004-003-V-1, 2004.
- [65] O. Buning (Ed.) *et. al.*, *LHC Design Report. 2. The LHC infrastructure and general services*, Tech. Rep. CERN-2004-003-V-2, 2004.
- [66] M. Benedikt (Ed.) *et. al.*, *LHC Design Report. 3. The LHC injector chain*, Tech. Rep. CERN-2004-003-V-3, 2004.
- [67] D. Froidevaux and P. Sphicas, *General-purpose detectors for the Large Hadron Collider*, *Ann. Rev. Nucl. Part. Sci.* **56** (2006) 375–440.
- [68] **ATLAS** Collaboration, “The ATLAS Experiment at the CERN Large Hadron Collider.” ATL-COM-PHYS-2007-102 (to be published in *J. Instrum.*), 2007.
- [69] H. H. J. ten Kate, *ATLAS superconducting toroids and solenoid*, *IEEE Trans. Appl. Supercond.* **15** (2005) 1267–1270.
- [70] A. Yamamoto *et. al.*, *The ATLAS central solenoid*, *Nucl. Instrum. Meth.* **A584** (2008) 53–74.
- [71] **ATLAS Liquid Argon** Collaboration, J. Y. Hostachy, *Construction and test results of the ATLAS EM barrel calorimeter and presampler*, *Nucl. Phys. Proc. Suppl.* **125** (2003) 112–116.
- [72] P. Adragna *et. al.*, *The ATLAS hadronic tile calorimeter: From construction toward physics*, *IEEE Trans. Nucl. Sci.* **53** (2006) 1275–1281.
- [73] **ATLAS** Collaboration, *Tile Calorimeter Technical Design Report*, Tech. Rep. CERN-LHCC-96-42.
- [74] K. Kordas *et. al.*, *The ATLAS Data Acquisition and Trigger: Concept, design and status*, *Nucl. Phys. Proc. Suppl.* **172** (2007) 178–182.
- [75] R. W. L. Jones, *ATLAS computing and the GRID*, *Nucl. Instrum. Meth.* **A502** (2003) 372–375.
- [76] **ATLAS** Collaboration, D. Adams *et. al.*, “The ATLAS Computing Model.” ATL-SOFT-2004-007, CERN-LHCC-2004-037/G-085, 2005.
- [77] S. McKee, *The ATLAS computing model: status, plans and future possibilities*, *Comput. Phys. Commun.* **177** (2007) 231–234.
- [78] **GEANT4** Collaboration, S. Agostinelli *et. al.*, *GEANT4: A simulation toolkit*, *Nucl. Instrum. Meth.* **A506** (2003) 250–303.
- [79] J. M. Campbell, J. W. Huston and W. J. Stirling, *Hard interactions of quarks and gluons: A primer for LHC physics*, *Rept. Prog. Phys.* **70** (2007) 89.

- [80] R. P. Feynman, “The behavior of hadron collisions at extreme energies.” Invited paper at the Third Conference on High-Energy Collisions, Stony Brook, New York, 5-6 Sep 1969.
- [81] M. Dittmar *et. al.*, *Parton distributions: Summary report for the HERA - LHC workshop*, arXiv:hep-ph/0511119.
- [82] V. N. Gribov and L. N. Lipatov, *Deep inelastic $e p$ scattering in perturbation theory*, *Sov. J. Nucl. Phys.* **15** (1972) 438–450.
- [83] G. Altarelli and G. Parisi, *Asymptotic Freedom in Parton Language*, *Nucl. Phys.* **B126** (1977) 298.
- [84] Y. L. Dokshitzer, *Calculation of the Structure Functions for Deep Inelastic Scattering and $e+e-$ Annihilation by Perturbation Theory in Quantum Chromodynamics.*, *Sov. Phys. JETP* **46** (1977) 641–653.
- [85] **H1** Collaboration, N. Raicevic, *Structure functions and extraction of PDFs at HERA*, arXiv:hep-ex/0605050. Proceedings of 41st Rencontres de Moriond: QCD and Hadronic Interactions, La Thuile, Italy, 18-25 Mar 2006.
- [86] K. Wichmann, *Recent Results from HERA Experiments*, arXiv:0707.2724 [hep-ex]. Proceedings of the Symposium on Hadron Collider Physics 2006 (HCP 2006), Durham, North Carolina, 22-26 May 2006.
- [87] **CTEQ** Collaboration, J. Pumplin *et. al.*, *New generation of parton distributions with uncertainties from global QCD analysis*, *JHEP* **0207** (2002) 012.
- [88] M. Lambacher, *Study of fully hadronic $t\bar{t}$ decays and their separation from QCD multijet background events in the first year of the ATLAS experiment*. PhD thesis, Ludwig-Maximilians-Universität München, 2007.
- [89] E. S. Swanson, *Aspects of confinement: A brief review*, *AIP Conf. Proc.* **717** (2004) 636–645 [arXiv:hep-ph/0310089].
- [90] B. R. Webber, *Fragmentation and hadronization*, arXiv:hep-ph/9912292. Proceedings of 19th International Symposium on Lepton and Photon Interactions at High-Energies (LP 99), Stanford, California, 9-14 Aug 1999, pp 577-606.
- [91] T. Sjostrand *et. al.*, *High-energy-physics event generation with PYTHIA 6.1*, *Comput. Phys. Commun.* **135** (2001) 238–259.
- [92] G. Corcella *et. al.*, *HERWIG 6: An event generator for hadron emission reactions with interfering gluons (including supersymmetric processes)*, *JHEP* **01** (2001) 010.
- [93] B. Andersson, G. Gustafson, G. Ingelman and T. Sjostrand, *Parton Fragmentation and String Dynamics*, *Phys. Rept.* **97** (1983) 31–145.

- [94] G. Marchesini and B. R. Webber, *Simulation of QCD Jets Including Soft Gluon Interference*, *Nucl. Phys.* **B238** (1984) 1.
- [95] G. Marchesini and B. R. Webber, *Monte Carlo Simulation of General Hard Processes with Coherent QCD Radiation*, *Nucl. Phys.* **B310** (1988) 461.
- [96] S. R. Slabospitsky and L. Sonnenschein, *TopReX generator (version 3.25): Short manual*, *Comput. Phys. Commun.* **148** (2002) 87–102.
- [97] E. Richter-Was, D. Froidevaux and L. Poggioli, “ATLFAST 2.0 — a fast simulation package for ATLAS.” ATL-PHYS-98-131, 1998.
- [98] M. Mangano *et. al.*, *ALPGEN, a generator for hard multiparton processes in hadronic collisions*, *JHEP* **2003** (2003), no. 07 001–001.
- [99] **CTEQ** Collaboration, H. L. Lai *et. al.*, *Global QCD analysis of parton structure of the nucleon: CTEQ5 parton distributions*, *Eur. Phys. J.* **C12** (2000) 375–392.
- [100] A. D. Martin, R. G. Roberts, W. J. Stirling and R. S. Thorne, *MRST2001: Partons and α_s from precise deep inelastic scattering and Tevatron jet data*, *Eur. Phys. J.* **C23** (2002) 73–87.
- [101] I. Borjanovic *et. al.*, *Investigation of top mass measurements with the ATLAS detector at LHC*, *Eur. Phys. J.* **C39S2** (2005) 63–90.
- [102] CERN, “Computer Newsletter (Nov 8, 2004): *New Time Units simplify procedures*.” Article available in <http://cerncourier.com/objects/cnl/1/11/1/nov-decpdf.pdf>.
- [103] **ATLAS** Collaboration, “Top Simulation Technology.” Webpage available in <https://twiki.cern.ch/twiki/bin/view/Atlas/TopSimulationTechnology>.
- [104] **ATLAS** Collaboration, A. Rimoldi, *The ATLAS detector simulation application*, *Nucl. Phys. Proc. Suppl.* **172** (2007) 49–52.
- [105] **ATLAS** Collaboration, *ATLAS Computing Technical Design Report*, Tech. Rep. ATLAS TDR-017, CERN-LHCC-2005-022, 2005.
- [106] P. Perrodo, *Commissioning of the ATLAS detector and combined beam test results*, *Nucl. Instrum. Meth.* **A572** (2007) 113–116.
- [107] M. Dobbs *et. al.*, “HepMC 2: a C++ Event Record for Monte Carlo Generators.” Available in <http://savannah.cern.ch/projects/hepmc>, 2008.
- [108] **ATLAS** Collaboration, “The expected performance of the ATLAS experiment – Physics, trigger and detector.” CERN report in preparation, 2008.
- [109] Worldwide LHC Computing Grid, “gLite 3.1 User Guide.” CERN-LCG-GDEIS-7222398, 2008.

- [110] S. Frixione and B. Webber, *The MC@NLO 3.1 Event Generator*, arXiv:hep-ph/0506182.
- [111] S. Frixione, P. Nason and B. R. Webber, *Matching NLO QCD and parton showers in heavy flavour production*, *JHEP* **08** (2003) 007.
- [112] J. M. Butterworth and J. R. Forshaw, *Photoproduction of multi - jet events at HERA: A Monte Carlo simulation*, *J. Phys.* **G19** (1993) 1657–1663.
- [113] J. M. Butterworth, J. R. Forshaw and M. H. Seymour, *Multiparton interactions in photoproduction at HERA*, *Z. Phys.* **C72** (1996) 637–646.
- [114] U. Baur and L. H. Orr, *High p_T Top Quarks at the Large Hadron Collider*, *Phys. Rev.* **D76** (2007) 094012.
- [115] B. P. Kersevan and E. Richter-Was, *The Monte Carlo Event Generator AcerMC 2.0 with Interfaces to PYTHIA 6.2 and HERWIG 6.5*, arXiv:hep-ph/0405247.
- [116] M. L. Mangano, M. Moretti, F. Piccinini and M. Treccani, *Matching matrix elements and shower evolution for top- quark production in hadronic collisions*, *JHEP* **01** (2007) 013.
- [117] P. Golonka *et. al.*, *The tauola-photos-F environment for the TAUOLA and PHOTOS packages, release II*, *Comput. Phys. Commun.* **174** (2006) 818–835.
- [118] E. Norrbin and T. Sjostrand, *QCD radiation off heavy particles*, *Nucl. Phys.* **B603** (2001) 297–342.
- [119] **ATLAS** Collaboration, “The ATLAS Computing Workbook (ATHENA 12.0.6).” Webpage available in <https://twiki.cern.ch/twiki/bin/view/Atlas/WorkBook>.
- [120] A. Shibata, “TopView - ATLAS top physics analysis package.” ATL-SOFT-PUB-2007-002, 2007.
- [121] A. Shibata, *Investigation of Electroweak Production of the Top Quark at the LHC*. PhD thesis, London, Queen Mary University of London, 2007.
- [122] K. Cranmer, A. Farbin and A. Shibata, “EventView - The Design Behind an Analysis Framework.” ATL-SOFT-PUB-2007-008, 2007.
- [123] R. Lefèvre and C. Santoni, “In situ determination of the scale and resolution of the jet energy measurements using Z^0 +jet events.” ATL-PHYS-2002-026, 2002.
- [124] M. Sapinski, *Expected performance of ATLAS for measurements of jets, b-jets, τ -jets and E_T^{miss}* , *EPJ Direct* **4 S1** (2001) 8.
- [125] J. A. Aguilar-Saavedra, J. Carvalho, N. Castro, A. Onofre and F. Veloso, *ATLAS sensitivity to Wtb anomalous couplings in top quark decays*, *Eur. Phys. J.* **C53** (2008) 689–699.

- [126] F. Hubaut, E. Monnier, P. Pralavorio, K. Smolek and V. Simak, *ATLAS sensitivity to top quark and W boson polarization in t anti-t events*, *Eur. Phys. J. C* **44S2** (2005) 13–33.
- [127] **ATLAS** Collaboration, “The Atlantis Event Display.” Webpage available in <https://twiki.cern.ch/twiki/bin/view/Atlas/WorkBookAtlantis>.
- [128] J. A. Aguilar-Saavedra, J. Carvalho, N. Castro, F. Veloso and A. Onofre, “Study of the ATLAS sensitivity to angular asymmetries in top quark decays.” ATL-PHYS-PUB-2006-018, 2005.
- [129] W. H. Press *et. al.*, *Numerical Recipes — The Art of Scientific Computing*. Cambridge University Press, 1964.
- [130] G. Cowan, *Statistical Data Analysis*. Oxford Science Publications, 1998.
- [131] **CDF** Collaboration, S. Moed *et. al.*, “Measurement of Helicity Fractions in Top-Quark Decays Using $\cos \theta^*$.” CDF Conf. Note 9215, 2008.
- [132] E. Boos, L. Dudko and T. Ohl, *Complete calculations of $Wb\bar{b}$ and $Wb\bar{b}+jet$ production at Tevatron and LHC: Probing anomalous Wtb couplings in single top production*, *Eur. Phys. J. C* **11** (1999) 473–484.
- [133] G. Mahlon and S. J. Parke, *Single top quark production at the LHC: Understanding spin*, *Phys. Lett. B* **476** (2000) 323–330.
- [134] M. Jezabek and J. H. Kuhn, *V-A tests through leptons from polarized top quarks*, *Phys. Lett. B* **329** (1994) 317–324.
- [135] M. Jezabek, *Top quark physics*, *Nucl. Phys. Proc. Suppl.* **37B** (1994) 197.
- [136] G. Mahlon and S. J. Parke, *Improved spin basis for angular correlation studies in single top quark production at the Tevatron*, *Phys. Rev. D* **55** (1997) 7249–7254.
- [137] T. Stelzer and S. Willenbrock, *Spin Correlation in Top-Quark Production at Hadron Colliders*, *Phys. Lett. B* **374** (1996) 169–172.
- [138] W. Bernreuther, A. Brandenburg, Z. G. Si and P. Uwer, *Top quark pair production and decay at hadron colliders*, *Nucl. Phys. B* **690** (2004) 81–137.
- [139] N. Castro, *LHC sensitivity to top properties beyond the SM*, *PoS TOP2006* (2006) 028. Proceedings of the Top2006 Workshop, Coimbra, Portugal, January 2006.
- [140] A. Onofre, “Testing the Standard Model in $t\bar{t}$ and single top production at the LHC.” ATL-PHYS-CONF-2007-004 (talk at *ICHEP 06* conference, Moscow, Russia, July 2006), 2006.
- [141] F. Veloso, “Top quark properties: prospects at ATLAS.” (proceedings of the Top2008 Workshop, Isola d’Elba, Italy, May 2008; to be published in *Nuov. Cim.*), 2008.

- [142] J. A. Aguilar-Saavedra, J. Carvalho, N. Castro, F. Veloso and A. Onofre, “ATLAS sensitivity to Wtb anomalous couplings in $t\bar{t}$ events.” (proceedings of the *Top2008* Workshop, Isola d’Elba, Italy, May 2008; to be published in *Nuov. Cim.*), 2008.